Deformation and Fracture of Polymers with Work Hardening Behavior

by

Souvenir Muhammad

A thesis submitted in partial fulfillment of the requirements for the degree of

Doctor of Philosophy

Department of Mechanical Engineering

University of Alberta

Abstract

Ductile and brittle failure behaviors of semi-crystalline polymers such as high density polyethylene (HDPE) were investigated under uni-axial tensile loading at various test conditions.

The first part of the thesis examines the influence of aspect ratio of rectangular cross-section on the tri-axial stress state developed by necking in tensile specimens of HDPE. The approach included both experimental and numerical simulation, and identified that anisotropy is involved in the deformation process during necking. The study shows that with increasing aspect ratio anisotropy in the deformation process increases.

A new phenomenological model is then developed in an endeavor to reproduce the experimental work to identify the tri-axial stress state during the large deformation. The innovation lies in the unique technique used to develop the simulation model. The study clearly shows the advantages of this model over previously developed models by other researchers in this field. The results show that the technique is capable of considering non-linear and creep deformation

during the necking and has the potential to mimic accurately the stress-strain relationship along with lateral dimensional deformation obtained from the experimental testing.

Deformation of HDPE in tension was also analyzed at various crosshead speeds, to quantify the corresponding strain rate and strain rate variation during the necking process. The study clearly states with evidence that the common practice to evaluate the strain rate effect based on the measured total strain is acceptable in spite of the involvement of the creep strain.

Another new test methodology developed by using cylindrical specimens with a gauge section design to generate and evaluate bulk cavitation in HDPE. This design is unique, as it has the potential of generating bulk cavitation without the presence of any sharp notch, whereas all the works in literature to study bulk cavitation in polymers involve sharp notch and crack growth. Since no sharp notch is used in the new specimen design, its deformation does not involve crack growth, and therefore, is purely governed by the cavitation-induced rupture process. The FEM results indicate that hydrostatic stress level for bulk cavitation is about three times of that for necking at the same strain level. As a result, the

new specimen design has bulk cavitation replace necking as the dominant deformation mechanism in HDPE. The thesis shows that by changing the gauge section geometry, deformation of HDPE specimen under tension can be dominated by either bulk cavitation or the commonly observed necking. The FE results also suggest that the hydrostatic stress at the peak load needs to reach a level similar to the uniaxial yield strength in order to replace the necking by the bulk cavitation.

Preface

I have conducted research for this thesis under supervision of Dr. P.-Y. Ben Jar. Department of Mechanical Engineering, University of Alberta and Dr. Jar's laboratory resources have been used to conduct this research.

Chapter 2 of this thesis has been published as S. Muhammad, and P.-Y. B. Jar, 2010. "Effect of Aspect Ratio on Large Deformation and Necking of Polyethylene," *J. Mater. Sci.*, 46 (4) 1110-1123. I was involved in formation of concept, research planning, data analysis and all experimental and simulation work as well as the manuscript composition, Dr. Jar was the supervisory author and contributed to manuscript edit.

Chapter 3 of this thesis has been published as S. Muhammad, and P.-Y. B. Jar, 2013. "Determining Stress-Strain Relationship for Necking in Polymers Based on Macro Deformation Behavior," *Finite Elements in Analysis and Design*, 70-71, 36-43. Formation of concept, research planning, data analysis and all experimental and simulation work were done by me as well as the initial manuscript. Dr. Jar was involved in concept formation and manuscript edit.

Chapter 4 of this thesis has been published as S. Muhammad, and P.-Y. B. Jar, 2014. "Finite Element Modeling to Determine the Strain Rate Variation for Non-Viscous Deformation of HDPE During the Necking Process," *The IUP Journal of Mechanical Engineering*, 7 (2) 7-27. Formation of concept, research planning, data analysis and all experimental and simulation work were done by me as well as the initial manuscript. Dr. Jar was involved in concept formation and manuscript edit.

Chapter 5 of this thesis has been published as P.-Y. B. Jar, Souvenir Muhammad, 2012. "Cavitation-Induced Rupture in High-Density Polyethylene Copolymers," *Polym. Eng. Sci.*, 52, 1005-1014. Research planning, Specimen design, data analysis and all experimental and simulation work were done by me. Dr. Jar was involved in concept formation and manuscript composition.

Acknowledgements

I am obliged to my supervisor, Dr. P.-Y. Ben Jar for his continuous guidance and financial support throughout this study.

Special thanks to all the funding sources. The work was supported by Natural Sciences and Engineering Research Council of Canada (NSERC), NOVA Chemicals, and Queen Elizabeth II Ph.D. Graduate Scholarship at the University of Alberta.

Sincere appreciation is also due to T. Hilvo for help in specimen preparation, B. Faulkner for fabrication of the extensometer used in the experiments, R. Adianto for assistance in machine operation for testing, and I also wish to thank H. J. Kwon and S. Adeeb for invaluable advices in ABAQUS operation.

My gratitude to my wife, Shamima Shahid Dalia, for her support, and my parents for believing in me throughout the study.

TABLE OF CONTENTS

List of Tables

List of Figures

List of Abbreviations and Symbols

ABS	Poly(acrylonitrile-butadiene-styrene)
ASTM	American Standard for Testing Materials
a, b, c, d, e, k,	Constants of Constitutive model
M, N, αk, β	
A, n, m	User-defined constants of power-law creep model
DBT	Ductile-Brittle Transition
DENT	Double-edge-notched tensile
E	Young's modulus
FEM	Finite Element Method
FE	Finite Element
F_T	Triaxiality Factor
f	Yield function
HDPE	High-Density Polyethylene
J_2	Second stress invariant
M_n	Number-averaged molecular weight
M_w	Weight-averaged molecular weight
M_w/M_n	Molecular weight distribution
MPa	Mega pascals
P	Measured load
PE	Polyethylene
PC	Polycarbonate

SA	Simulation attempt
SCG	Slow crack growth
T	Time, $T = \frac{Elongation}{Crosshead\ speed} \times 60$
t	Thickness of specimen with rectangular cross-section
t_o	Initial thickness
t_f	Final thickness after necking
UT	Uni-axial tensile
W	Width of specimen with rectangular cross-section
W_o	Initial width
W_f	Final width after necking
Y	Yield stress
3D	Three dimensional
K, ξ, S	Adjusting factors for slope, curvature and horizontal shift of equation of χ
χ	Ratio of normalized width to normalized thickness
χ_f	Value of χ after completion of necking
$\overline{\sigma_{eff}}$	Mean Effective Stress
σ_x	Mean Axial Stress
$\sigma(\varepsilon)$	von-Mises stress as a function of von-Mises strain
σ_{eng}	Engineering stress
σ_{true}	True stress
ε	von-Mises strain
ε_y	Transitional strain between linear and nonlinear part of the

	elastic deformation
ε_n	Strain for on-set of necking
ε_t	transitional strain for the strain-hardening part of the plastic deformation
ε_{true}	True strain
$\dot{\bar{\varepsilon}}^{cr}$	uni-axial-equivalent creep strain rate
σ_{11}	Stress component in axial direction
σ_{22}	Stress component in transverse (width for rectangular cross-section specimen) direction
σ_{33}	Stress component in transverse (thickness for rectangular cross-section specimen) direction
σ_{12}	Shear stress component in plane 1-2 of stress tensor
σ_{23}	Shear stress component in plane 2-3 of stress tensor
σ_{31}	Shear stress component in plane 3-1 of stress tensor
$\tilde{q}$	von-Mises-equivalent stress
Ω	Rate of neck length increase
υ	Poisson's ratio
$\partial\sigma/\partial\varepsilon$	Tangent modulus

CHAPTER - 1

Introduction

1.1 Introduction and Background

Nowadays, undoubtedly polymers and polymer-based composites are invariably the principal substitute for metals in engineering and structural applications because of their excellent corrosion resistance, low cost and ease of processing. But the end use in engineering applications often faces restrictions due to their

macroscopic mechanical properties. Among these mechanical properties, deformation behaviour in elastic and small plastic region has been studied extensively in the past. Also theoretical and experimental schemes on fracture, proceeded by extremely small or large deformations, attracted attention from many researchers around the world. Large deformation, especially when necking occurs, has been studied abundantly in the past [1-8]. This is not only because understanding this behaviour has great potential to advance knowledge on material deformation, but also due to the common occurrence of necking in the fracture process of materials with high toughness, which necessitates vigorous understanding of the phenomenon.

Due to the susceptibility to spontaneous strain localization (commonly known as necking) and strain hardening that arises from structural rejuvenation, induced by large deformation of polymers such as high-density polyethylene (HDPE), the ability to predict necking in polymers has become essential for assurance of their reliable performance, especially when considering applications such as pipelines and pressure vessels. As a result, much of the research work on polymers has been dedicated to study of the necking behavior and the damage evolution process

during the neck development. However, challenges are encountered due to the time-dependent deformation process (such as creep) that plays a critical role for many polymers in the long-term service. As a result, most of the characterization methods to evaluate reliability of the long-term performance of polymers require tests on the full-sized products. Since those tests are time-consuming to carry out and involve significant uncertainty in its prediction accuracy, numerical simulation along with experimental investigation becomes obvious. Thus the urge for proper constitutive model that can accurately predict the deformation and fracture behaviour as well as ease of application to different polymers results in numerous studies in the area. During the last few decades many approaches have been proposed to establish the stress-strain relationship for polymer deformation.

Fracture behaviour of polymer after little deformation has been studied extensively in the past. But in ductile polymer, brittle fracture is hard to generate without the presence of sharp notch. It is even harder to generate cavitation-induced brittle fracture. Cavitation is known to be involved in many polymer products during the failure process. Its occurrence often results in

whitening appearance that is similar to that from crazing or shear yielding [9-10]. Unfortunately, the amount of cavities reported in most studies is too small to register any disturbance in the test results (i.e. load and displacement). Later, sharp notches are considered to encourage bulk cavitation [11-12]. But, due to crack growth from the notch tips, loading conditions for the bulk cavitation are extremely difficult to identify.

Despite difficulties in generating bulk cavitation in semi-crystalline polymers, such behaviour has been observed in rubber more than half a century ago. Gent and Lindley [13] demonstrated the bulk cavitation behaviour in short cylindrical specimens of rubber when subjected to tensile loading. The bulk cavitation caused a noticeable disruption on the load-displacement curve, but afterwards, the load resumed the initial trend of increase with further stretch until the final breakup. Thus, it is possible that such a cavitation behavior can also be generated in semi-crystalline polymers. However, loading conditions for the bulk cavitation in semi-crystalline polymers remain scarce in this field.

1.2 Rationale and objective

Despite the attention the scientific world has applied to the issue of large deformation behavior and associated fracture of polymers, there are some fundamental questions to which the answers still remain incomplete. Some questions that have been posed regarding the issue include: What is the effect of hydrostatic stress in the yielding behavior in the large deformation of polymers? To what extent the incorporation of hydrostatic stress in the yield function allows the simulation to mimic accurately the experimental observation? What is the role of creep during necking, neck propagation and cavitation-induced failure? How can one incorporate the failure criteria in the simulation to identify the loading condition between ductile and brittle failure? The scarcity of information in literature regarding the issue of hydrostatic stress and creep involvement in the necking and neck propagation of polymers, as well as the lack of proper information on cavitation-induced rupture criteria, provide the motivation for this research. Table 1-1 presents some of the few works that developed constitutive model to study the necking and neck propagation in polymers.

The thesis is primarily focused on the areas that have a lot of undiscovered regions yet to be explored. In its most general formulation, the objective of the proposed research is to develop a 3D finite element continuum model that is based on proper constitutive equations to generate stress states in both uni-axial and multi-axial loading conditions to disclose the undiscovered realm of large deformation and necking phenomena, and to generate and identify the stress state for cavitation-induced rupture in polymers. The research approaches include experimental study and numerical simulation using FEM model to achieve: 1. understanding and formulation of creep behavior exhibited by the material chosen for the investigation (high-density polyethylene, HDPE) during necking, 2. quantification of the role of hydrostatic stress on the variation of lateral dimensions and the ductile-brittle transition (DBT) in the failure mechanism, and 3. generating bulk cavitation and identifying the loading condition responsible for the bulk cavitation.

1.3 Necking and cavitation phenomena

Large deformation mechanisms of semi-crystalline polymers like HDPE have been studied abundantly in the past. Global necking phenomenon was described as a three-stage deformation process [14]: (a) plastic deformation of the original spherulitic structure, (b) transformation of the spherulites to fibril structures by micro-necking, and (c) plastic deformation of the fibril structure. Another researcher [15] investigated polyethylene and related copolymers based on their true stress-strain behaviour. It was found that deformation at small strain mainly occurred in the amorphous inter-crystalline layers through inter-lamellar shear slips. However, deformation at large strains is attributed to crystallite fragmentation and chain disentanglement. Increase of work-hardening was observed with the increase of the strain-rates, crystallinity and network density.

Many semi-crystalline polymers involve cavitation in their failure process. Its occurrence often results in whitening appearance that is similar to that from crazing or shear yielding [9-10]. However, crazing or shear yielding does not reduce load-carrying capacity of the polymers, but cavitation does. Necking is one kind of shear yielding and causes ductile failure. Therefore, ability to detect

cavitation, and to distinguish it from crazing or shear yielding, is crucial for characterizing load-carrying capacity of the polymer products. Previous studies that combined mechanical testing with microscopic examination or X-ray scattering to identify loading conditions for cavitation, have suggested that cavitation in semi-crystalline polymers usually starts between lamellae or among spherulites, and that cavitation is likely to be responsible for the ductile-brittle transition in semi-crystalline polymers [e.g. 16-20].

To identify loading condition and the influence of hydrostatic stress for the occurrence of necking or cavitation, information on the tri-axial stress state at each stage of the deformation is extremely important. There is no alternative but to use numerical simulation to evaluate the stress tri-axiality and hydrostatic stress. During the last few decades many approaches have been proposed to establish the stress-strain relationship for polymer deformation.

Some approaches [2-3] consider interactions at the molecular level to relate the molecular interactions with the macroscopic deformation behavior. One of the first models in those approaches took into account rotation and alignment of molecular chain segments for establishing the stress-strain relationship for large

deformation in amorphous polymers. The model was later extended to three-dimensional deformation. More recently, Wu and Buckley [6] developed a model based on molecular interaction to capture most of the features observed in ductile deformation of amorphous polymers. Based on a slightly larger scale, Drozdov and Christiansen [21] developed a model for a similar purpose, that is, to mimic plastic and visco-plastic deformation in semi-crystalline polymers.

A different approach, generally known as phenomenological models, was developed by considering mainly deformation at the macroscopic scale [1, 4-5].

PAE et al (2000) [28] shows affects of hydrostatic pressure on the stress whitened region of test coupons of polyethylene and polypropylene. The effect of stress triaxiality on the necking and neck propagation of a cylindrical specimen (following Bridgman triaxiality factor [22], $F_T = \overline{\sigma_{eff}} / \sigma_x$, where $\overline{\sigma_{eff}}$ is the mean effective stress and σ_x is the mean axial stress) was investigated by G'Sell et al. [23] and found that the section with a convex external profile has $F_T > 1$ and that with a concave external profile $F_T < 1$.

It is also found in the literature that for tempered steel and many polymers like polyethylene and polycarbonate, the compressive yield stress is higher than the

tensile counterpart [24], which implies that hydrostatic stress component may influence the yield process, which necessitates the modification of the yield criteria to consider the hydrostatic pressure. Raghava et al. [25] examined yield surface of various polymers under a wide range of loading conditions. Spitzig and Richmond [26] showed the variation of deformation behavior of some polymers in both tensile and compressive tests under various hydrostatic pressures. Similar effects of applied hydrostatic pressure on the mechanical behavior of some polymers (polyurethane, polyoxymethylene, and branched low-density polyethylene) were investigated experimentally by Silano et al. [27].

1.4 Materials

Four HDPEs were used in the study, two containing hexene co-monomers (H-series) and the other two octene co-monomers (O-series). Characteristics of the HDPEs, such as number-averaged (M_n) and weight-averaged (M_w) molecular weights, molecular weight distribution (M_w/M_n) and density, are listed in Table 1-2. All polymers were supplied by NOVA Chemicals. NOVA provided compression-molded rectangular plates with nominal thickness in the range from

2 to 10 mm from HDPE pellets. Melt flow was minimized during the molding process to avoid molecular alignment, thus ensuring isotropy of the mechanical properties. NOVA Chemicals kept the cooling rate constant to ensure same degree of crystallinity within each plate of HDPE.

HDPE is a semi-crystalline polymer which is composed of both crystalline and amorphous regions. Figure 1-1 shows a typical structure of a semi-crystalline polymer. The crystalline region consists of spherulities in which multiple lamellae are stacked together. Layered structure of folded entangled polymer chains are called lamella. Due to excellent ductility and enhanced work hardening, HDPE exhibit stable strain localization (necking) during plastic deformation.

1.5 Thesis overview

This thesis is structured in a way that chapters 2, 3 and 4 will discuss about the strain localization (necking) of HDPE Cavitation-induced rupture will be discussed in chapter 5 and 6.

Chapter 2 presents an experimental study that used 2 types of HDPE as sample material to identify the thickness-dependent relationship between engineering stress and elongation from tensile tests. It also describes finite element simulation of large deformation and necking in HDPE when subjected to uni-axial tension. True stress-strain relationship and the governing equation for visco-plastic deformation are determined from the finite element simulation based on experimental data for the two HDPEs, which reveals influence of aspect ratio of cross section on the stress state during the necking process.

An approach, based on mechanical testing and finite element modeling, is exhibited in chapter 3 to establish the stress-strain relationship for polymers when necking evolves under tension. This chapter gives details of criteria used for evaluating the stress-strain relationship during the necking process, and depicts how the total strain range is divided into several sections for the ease of the iterative calculation process. HDPE is used as a sample polymer to illustrate the approach. Deformation of HDPE in tension was analyzed in chapter 4 at different crosshead speeds to quantify the corresponding strain rate and strain rate variation during the necking process. Since deformation of HDPE is time-dependent at

room temperature, total strain generated in tensile test of HDPE consists of elastic-plastic strain and creep strain which have different stress response. Therefore, it is important to characterize the rate of the two types of deformation separately. The chapter uses finite element modeling to distinguish the two types of strain during the necking process.

Experience of research described in chapters 2, 3 and 4 enables a design of cylindrical specimen with short gauge length which has the potential of generating bulk cavitation in HDPE. Chapter 5 describes a method which is different from that in literature in that the latter must use sharp notches to generate bulk cavitation. Since no sharp notch is used in the new specimen design, its deformation does not involve crack growth, and therefore, is purely governed by the cavitation-induced rupture process. Bulk cavitation is investigated in two types of HDPE that have different molecular weight and its distribution characteristics.

In chapter 6, finite element (FE) models, with constitutive equation established based on mechanical test results, are used to investigate the effects of hydrostatic stress level on the deformation behaviour in polyethylene (PE). It has been

demonstrated that by changing the gauge section geometry, deformation of PE specimen under tension can be dominated by either bulk cavitation or the commonly observed necking. This chapter uses variation of load and cross sectional dimension from the mechanical testing to establish the stress-strain relationship for the FE model, in order to determine the critical stress state that leads to either necking or bulk cavitation.

Conclusions are summarized in chapter 7 along with the recommendations for the future work.

This thesis is based on paper format of five papers, three of which are published and the other two are ready to be submitted in technical journals. Reference of the papers and the corresponding chapters are listed below.

Chapter 2: S. Muhammad and P.-Y. B. Jar. "Effect of aspect ratio on Large deformation and necking of Polyethylene", Journal of Materials Science. 46, 1110-1123 (2010).

Chapter 3: S. Muhammad and P.-Y. B. Jar. "Determining stress-strain relationship for necking in polymers based on macro deformation

behavior", Finite Elements in Analysis and Design. 70-71, pp. 36-43 (2013).

Chapter 4: S. Muhammad and P.-Y. B. Jar. "Variation of Strain Rate during the Necking Process of High-Density Polyethylene", to be submitted.

Chapter 5: P.-Y. B. Jar and Souvenir Muhammad. "Cavitation-Induced Rupture in High-Density Polyethylene Copolymers ", Polymer Engineering and Science. 52, pp. 1005-1014 (2012).

Chapter 6: S. Muhammad and P.-Y. B. Jar. "Effect of Hydrostatic Stress Level on Bulk Cavitation in Polyethylene ", to be submitted.

Figures:

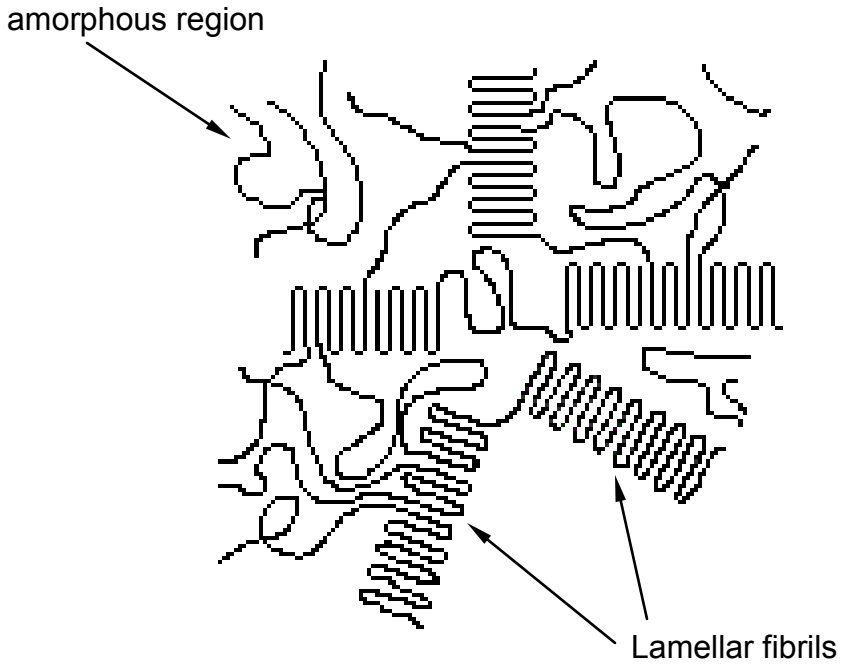

Figure 1-1 Schematic illustration of typical HDPE.

Tables:

Table 1-1 Previous works that developed constitutive model to study necking of polymers.

Researchers	Constitutive model based on	Results (parameters) presented	Variables	Comparison with experiments
Neale and Tugcu (1985)	Isotropic hardening J_2 flow theory	1. Stress-strain distribution across initial necking section 2. Stress triaxiality		Not done
Boyce and Arruda (1990)	Molecular chain segment rotation and alignment	True stress-true strain curves for both tension and compession		done
Li and Buckley (2008)	Molecular structure (GR constitutive model)	1. True stress-strain curve. 2. Strain localization factor	Strain rate	done
Wu and Van der Giessen (1995)	Molecular chain segment rotation and alignment	1. Nominal stress response 2. Thickness reduction ratio	1. Initial imperfection 2. Strain softening and hardening parameters 3. Strain rates	Not done
Tomita (1993)	Isotropic hardening J_2 flow theory	1. Iterative process to identify model parameters. 2. Necking	1. Strain rate 2. Temperature and 3. Stress triaxiality	Not done
Kwon and Jar (2008)	Isotropic hardening J_2 flow theory	1. Proposed new iterative process to identify model parameters. 2. Large deformation behavior in UT and DENT test		done

Table 1-2 Material characteristics of high-density polyethylene copolymers used in this study

Resin		Number-averaged molecular weight, Mn	Weight-averaged molecular weight, Mw	Mw/Mn	Branches / 1000 C	Density (g/cm^3)	Tensile strength at peak load (MPa)
Hexene copolymer	H-1	17,100	182,000	10.6	2.5 - 2.9	0.945	21.0
	H-2	14,400	154,000	10.7	4.7 - 5.3	0.940	20.5
Octene copolymer	O-1	40,700	89,000	2.2	2.0 - 2.4	0.944	21.9
	O-2	30,400	73,100	2.4	3.4 - 4.2	0.941	20.0

References

1. Neale KW, Tugcu P (1985) Analysis of necking and neck propagation in polymeric materials. J. Mech. Phys. Solids 33:323-337

2. Boyce MC, Arruda EM (1990) An experimental and analytical investigation of the large strain compressive and tensile response of glassy polymers. Polym. Eng. Sci. 30:1288-1298

3. Wu PD, Van Der Giessen E (1995) On neck propagation in amorphous glassy polymers under plane strain tension. Int. J. Plasticity 11:211-235

4. Tomita Y, Hayashi K (1993) Thermo-elasto-viscoplastic deformation of polymeric bars under tension. Int. J. Solids Structures 30:225-235

5. Kwon HJ, Jar P-YB (2008) On the application of FEM to deformation of high-density polyethylene. Int. J. Solids Structures 45:3521-3543

6. Li HX, Buckley CP (2008) Evolution of strain localization in glassy polymers: A numerical study. Int. J. Solids Structures 46:1607-1623

7. Fager LO, Bassani JL (1986) Plane strain neck propagation. Int. J. Solids Structures 22:1243-1257

8. Masud A (2005) A 3-D model of cold drawing in engineering thermoplastics. Mech. Adv. Mater. Structures 12:457-469

9. A. Galeski, *Prog. Polym. Sci.*, **28**, 1643 (2003).

10. A.S. Argon and R.E. Cohen, *Polymer*, **44**, 6013 (2003).

11. S. Castagnet, and Y. Deburck, Mater. Sci. Eng., **A448**, 56 (2007).

12. C. G'Sell, J.M. Hiver, and A. Dahoun, Inter. J. Solids and Structures **39**, 3857 (2002).

13. A.N. Gent, and P.B. Lindley, *Proc. R. Soc. London A*, **249**, 195 (1959).

14. Peterlin, A., 1971. Molecular model of drawing polyethylene and polypropylene. Journal of Materials Science 6 (6) 490-508

15. Hiss, R., Hobeika, S., Lynn, C., Strobl, G., 1999. Network stretching, slip processes, and fragmentation of crystallites during uniaxial drawing of polyethylene and related copolymers. A comparative study. Macromolecules 32 (13) 4390-4403

16. S. Castagnet, S. Girault, J.L. Gacougnolle, and P. Dang, *Polymer*, **41**, 7523 (2000).

17. X.C. Zhang, M.F. Butler, and R.E. Cameron, *Polymer*, **41**, 3797 (2000).

18. C.J.G. Plummer, A. Goldberg, and A. Ghanem, *Polymer*, **42**, 9551 (2001).

19. P.A. O'Connell, R.A. Duckett, and I.M. Ward, *Polym. Eng. Sci.*, **42**, 1493 (2002).

20. L.-Z. Liu, B.S. Hxiao, B.X. Fu, S. Ran, S. Toki, B. Chu, A.H. Tsou, and P.K. Agarwal, *Macromolecules*, **36**, 1920 (2003).

21. A.D. Drozdov, J. Christiansen, Nonlinear time-dependent response of isotactic polypropylene, J. Rheol. 47(3) (2003) 595-618

22. Bridgman PW (1944) Stress distribution at neck of tension specimen. Trans. Amer. Soc. Met. 32:553-572

23. Fang QZ, Wang TJ, Beom HG, Zhao HP (2009) Rate-independent large deformation behavior of PC/ABS. Polymer 50:296-304

24. Spitzig WA, Sober RJ, Richmond O (1975) Pressure dependence of yielding and associated volume expansion in tempered martensite. ACTA Metallurgica 23:885-893

25. Raghava R, Caddell RM (1973) The macroscopic yield behavior of polymers. J. Mater. Sci. 8:225-232

26. Spitzig WA, Richmond O (1979) Effect of hydrostatic pressure on the deformation behavior of polyethylene and polycarbonate in tension and in compression. Polym. Eng. Sci. 19:1129-1139

27. Silano AA, Bhateja SK, Pae KD (1974) Effects of hydrostatic pressure on the mechanical behavior of polymers: polyurethane, polyoxymethylene, and branched polyethylene. Int. J. Polym. Mater. 3:117-131

28. PAE, K. D., CHU, H.-C., LEE, J. K., KIM, J.-H., 2000. Healing of Stress-Whitening in Polyethylene and Polypropylene at or Below Room Temperature. Polymer Engineering and Science. 40 (8) 1783-1795

CHAPTER - 2

Effect of Aspect Ratio on Large Deformation and Necking of Polyethylene

2.1 Introduction and Background

Large deformation, especially when necking occurs, has attracted attention from many research groups around the world [1-8]. This is not only because understanding this behaviour has great potential to advance knowledge on material deformation, but also due to the common occurrence of necking in the

fracture process of materials with high toughness. Previous studies have shown that numerical simulation, when combined with experimental measurement, is a promising tool to determine material properties in large deformation. Among materials of interest in those studies, high-density polyethylene (HDPE) exhibits strong strain-hardening behaviour in large deformation, thus generating very stable neck development. The capability of stable necking before fracture is an important factor for HDPE in load-bearing applications, such as pipeline and pressure vessels that are used in the distribution network for oil and gas. In addition, extensive deformation is required in production of high-strength polymer fibres [9], for which the knowledge on necking facilitates the control of the production process. However, in spite of the importance of polymer necking in many industrial applications and extensive studies on its occurrence [1-19], mechanisms involved and criteria required are yet to be fully quantified. For polyethylene, the challenge is aggravated by the involvement of time-dependent deformation behaviour. At the time when this manuscript is prepared, only several studies [2, 5-6] are able to consider the time-dependent deformation behaviour in computer simulation to mimic accurately the necking process.

Most of the previous works on the necking behaviour [2-4, 6, 9-10] were focused on the effects of parameters such as strain rate, temperature and initial imperfection size on the neck development. Little attention has been paid to the influence of aspect ratio of the cross section. Thus, objective of the current study is to gain fundamental understanding of the influence of aspect ratio on the neck development, and to reveal the associated variation of stress state in the necking zone. In this work, aspect ratio is varied through thickness change for standard dog-bone specimens that are commonly used for simple tensile test.

This chapter consists of two parts: (i) experimental investigation to capture variation of the deformation behaviour and mechanical properties during the necking process, and (ii) computer simulation based on finite element (FE) method to determine the constitutive equation that can accurately mimic the experimental observations. Results from the study are used to enlighten the stress state generated during the necking process. In the remaining part of this section, two brief reviews of previous work on large deformation and necking of polymers are presented, one on experimental measurement and the other on FE simulation.

Experimental measurement

G'Sell and Jonas [12] and Kwon and Jar [18] gave detailed description on the neck development in simple tensile test. The former presents experimental curves of load versus elongation and engineering stress versus strain for polyvinyl chloride and HDPE, in which initiation and stabilization points on the curves for neck development are identified. The latter quantifies change of cross section and nominal stress in HDPE during the neck development. Kwon and Jar suggest that the neck development in HDPE occurs in two stages, for neck inception and neck propagation, respectively. In addition, following Hill's [20] approach they modified the neck initiation criterion determined from the simple tensile test, and applied it to the neck development in double-edge-notched tensile test. In an experimental study, G'Sell et al. [9] evaluated stress triaxiality (as defined in ref. [21]) in cylindrical tensile specimens, and suggested that the section with a convex external profile should have very different stress triaxiality from that with a concave external profile. Later, Kwon and Jar [5] used dog-bone specimens of rectangular cross section to demonstrate the non-uniform stress state on the cross section at the neck inception stage. Other studies on various polymers [10, 19] reported the true stress-strain relationship for large deformation using

experimental techniques, and measured variation of volume strain during the neck development.

Finite element simulation

Finite element method has been widely used in literature to simulate large deformation and necking of polymers like HDPE [e.g. 1-8]. However, most studies paid little attention to the establishment of proper constitutive equation to generate the deformation. Among the few attempts that paid attention to this, such as the work by Neale and Tugcu [1], Fager and Bassni [7] and Masud [8], the constitutive equation was rarely validated by experimental data.

To our knowledge, only four papers in the literature used experimental data to evaluate results from FE simulation. Boyce and Arruda [2], by considering rotation and alignment of molecular chain segments, developed a constitutive model to simulate necking in glassy polymers that exhibit both strain softening and straining hardening. Although they compared the simulation results with experimental data, we do not think that the agreement is close enough to fully validate the model, especially when subjected to tensile loading. As a result, the model was not adopted here to investigate the effects of aspect ratio on the neck

development. It should be noted that Wu and van der Giessen [3] used a constitutive model similar to the model developed by Boyce and Arruda, to study the necking phenomenon in glassy polymers. Variables considered in that study include initial imperfection size, strain softening and hardening parameters, strain rate, as well as specimen geometry. Although the model by Wu and van der Giessen uses material properties that could be determined experimentally, similar to the model by Boyce and Arruda, the simulation results were not explicitly validated using experimental data. Furthermore, aspect ratio was not included in the study as a variable for the specimen geometry.

Tomita and Hayashi [4] proposed an iterative process to identify model parameters that can accurately simulate the necking process at different temperatures and strain rates. The results were used to discuss effects of strain rate, temperature and stress triaxiality on the deformation behaviour during the necking process. Their iterative process was further modified by Kwon and Jar [5], from which the results exhibited a close agreement with the experimental observation on HDPE in both uni-axial tensile and double-edge-notched tensile tests. The constitutive model proposed by Kwon and Jar is through a combination

of stress-strain relationships for different ranges of deformation, which are available in the literature and the expressions are given below.

$$\sigma(\varepsilon)=\begin{cases} E\varepsilon & for\ \varepsilon \le \varepsilon_y \quad [1,14,16] \quad (a) \\ d\left[\{a(\varepsilon+b)\}^{(c-1)}-\{a(\varepsilon+b)\}^{(-c)}\right]+e & for\ \varepsilon_y \le \varepsilon \le \varepsilon_n \quad [22] \quad (b) \\ \alpha k\varepsilon^{N} & for\ \varepsilon_n \le \varepsilon \le \varepsilon_t \quad [23] \quad (c) \\ k\exp(M\varepsilon^{\beta}) & for\ \varepsilon \ge \varepsilon_t \quad [12,13] \quad (d) \end{cases} \tag{2.1}$$

in which unit for σ is MPa, ε_y represents the transitional strain between linear and nonlinear part of the elastic deformation, ε_n the strain for on-set of necking, and ε_t the transitional strain for the strain-hardening part of the plastic deformation.

Li and Buckley [6] also presented a numerical study on necking of glassy polymers by employing a glass-rubber constitutive model at the molecular level, in which the nonlinear elastic-viscoplastic deformation is incorporated in the response to deviatoric stress, to take into account the time-dependent deformation behaviour that is known for many polymers. Although all of the above work establishes the constitutive equation for large deformation and necking, the approach adopted by Tomita and Hayashi [4] and by Kwon and Jar [5] is different from that by Boyce and Arruda [2] and by Li and Buckley [6]. The former uses a macroscopic (global) approach, with validation based on load-elongation curve

and reduction of cross section in the necking process; while the latter uses a microscopic approach based on motion at the molecular level.

In addition to the above studies on necking, it is worth mentioning that some papers in the literature have searched for explanations for the compressive yield stress being higher than the tensile counterpart for many polymers such as polyethylene and polycarbonate. Spitzig et al. [24] suggested that hydrostatic stress and its type (tension or compression) may have influenced the yielding process. Raghava et al. [25] reported possible changes of the yield surface under a wide range of loading conditions. Spitzig and Richmond [26] showed the change of tensile and compressive deformation behavior for some polymers under various hydrostatic pressures. Similar studies were also conducted by Silano et al. [27]. Although those studies demonstrated variability of stress-strain curves by the change of hydrostatic pressure, the variation occurs only with a significant change of the hydrostatic pressure. In simple tensile tests conducted in the current study, the hydrostatic stress is mainly generated by axial load, of which the level should not be high enough to impose any significant effect on the yielding behaviour.

It should be noted that very few studies have been conducted to reveal the influence of cross sectional dimensions on the necking behaviour, let alone its influence on the triaxial stress state during the necking process. Scarcity of information in this area provides motivation for the current study.

2.2 Problem description and research methodology

Although necking is a phenomenon commonly observed in simple tensile test of many ductile polymers, the standard method (ASTM D638) that uses specimens of rectangular cross section does not consider the influence of aspect ratio (defined as the ratio of width to thickness of the cross section) on the deformation. In addition, current practice on material evaluation that is based on simple tensile test results only considers results up to the yield point, despite the fact that many products rely on post-yield deformation to evaluate their reliability and damage tolerance. In view of the possible influence of aspect ratio of specimen cross section on the post-yield deformation, we conducted experimental testing and FE simulation to understand the following phenomena: (i) variation of the necking behaviour with the change of aspect ratio, (ii) the corresponding change in the

triaxial stress state, and (iii) the involvement of viscoplastic deformation during the necking.

Methodology adopted in the study is firstly to identify constitutive stress-strain relationship that enables the FE model to mimic the deformation behaviour observed experimentally, which includes experimental load-elongation curve and the cross section reduction during the necking process. In this work, validation of the FE model is based on the following experimental data:

(i) Curves of engineering stress versus elongation, with special attention paid to the peak stress position (stress value and the corresponding elongation), profile for the stress-drop section, and the flow stress level during the neck propagation, and

(ii) Reduction of the cross section as a function of elongation at the location where the neck was initially generated.

The FE model that met the above criteria was then used to analyze the variation of stress state by the change of aspect ratio on the cross section.

The above approach for determining the constitutive relationship between stress and strain is different from the purely experimental measurement that was demonstrated by G'Sell et al. [19] who determined strains based on displacement at selected positions on the specimen surface. The experimental method by G'Sell et al. is applicable only if strain distribution is relatively uniform in the area between the selected positions. As the necking process involves significantly inhomogeneous reduction of cross section, the deformation clearly violates the above assumption. In a similar experimental approach, Fang et al. [10] used a three-dimensional non-contact technique, based on digital image correlation, to measure large deformation in polymers. Although this technique allows non-uniform strain distribution in the area of measurement, and has the potential to extract creep strain from the total strain, the measurement is limited to deformation on surface. When the strain on the surface does not represent the strain inside, such as the case for necking in polymers, the technique cannot be used to determine the internal strain values. As a result, techniques purely based on experimental measurement are insufficient to determine the constitutive equation when necking occurs. Instead, a new approach that combines

experimental measurement with computer simulation is adopted in this study to determine the constitutive equation for the FE simulation.

Experimental

Two types of HDPE, named PE1 and PE2 here, were provided by NOVA Chemicals for the experimental investigation. Characteristics of the HDPEs, such as molecular weight, molecular weight distribution and density, are given in Table 2-1. HDPE pellets were firstly compression-molded to rectangular plates with nominal thickness in the range from 2 to 10 mm. Melt flow was minimized during the molding process to avoid molecular alignment, thus ensuring isotropy of the mechanical properties. NOVA Chemicals kept the cooling rate constant to ensure same degree of crystallinity within each plate of HDPE. The rectangular plates of four different thicknesses were received from NOVA Chemicals. 19 mm wide strips were cut out of those plates using table saw. The strips were then machined to dog-bone specimens of standard dimensions, as shown in Figure 2-1, using Tensilkut II machine. The specimens were fine polished using sand paper to avoid any scratches or imperfactions due to machine cut. Width in the middle part of the gauge section, around 2 mm long, was reduced gradually by a maximum

reduction of 0.1 mm, which corresponds to less than 1% reduction from the original width. Such width reduction was to ensure that the neck initiation occurred at the location where the extensometer was placed, in order to measure accurately the width and thickness changes during the neck development. In addition, a high resolution video camera was used to record the neck initiation and growth along the gauge length, in order to quantify the neck growth rate.

Since standard dog-bone specimen has width fixed at 13 mm, variation of aspect ratio was through change of specimen thickness from 2 to 10 mm, corresponding to change of aspect ratio from 6.5 (for 2-mm-thick specimens) to 1.3 (for 10-mm-thick specimens). Although only specimen thickness was used as the variable to change the aspect ratio, the trend presented here should be universal and the constitutive equation determined applicable to mimicking the necking process in specimens of different width. It should be noted that in the beginning of this study, due to machining and polishing using 600-grit sand paper for the specimen preparation, there were concerns about the possible influence of the surface roughness on the deformation behaviour, and the influence may vary with the change of specimen width. Therefore, specimen width was kept constant to

remove this concern. It turned out that all specimens used in this study fractured after the neck had been fully developed in the whole gauge section. As a result, surface roughness introduced by machining and polishing did not have any effect on the necking behaviour described here.

The tensile tests were conducted using a universal testing machine (QUASAR 100) at a crosshead speed of 100 mm/min. The choice of a relatively high crosshead speed was to minimize the time for the neck initiation to be less than 30 seconds, in order to reduce the amount of time-dependent deformation so that a relative simple creep model could be used in the simulation to mimic the neck formation.

The experiments require measurement of width and thickness changes to determine strain values. To reduce scattering of width and thickness measurements during the necking, the measured data were smoothed using a commercial graphics software (KaleidaGraph version 3.5), based on a window size of 10 points for a data set of around 3000 points from each test.

Numerical simulation

The numerical simulation was carried out on two specimen thicknesses, 10 and 3 mm, using ABAQUS Standard (version 6.7-1). FE model for the former thickness has 4140 20-node brick elements and totally 19583 nodes, and for the latter 4620 20-node brick elements and 22183 nodes. As an example, Figure 2-2 shows the mesh pattern for the 10-mm-thick model, with 1-, 2-, and 3-axes designated the direction along length, width, and thickness, respectively. Due to geometrical symmetry, the FE model is only for half of the specimen length and quarter of the cross section. That is, point A in Figure 2-2 is at the center of the cross section in the middle of the specimen. An imperfection was introduced through a tapered width reduction, to reduce the width by about 0.07% of the original value at the cross section where point A is, so that necking was always initiated from there.

Plastic deformation generated in the FE model is based on J_2 flow theory, that is,

$$f(\sigma_{ij}) = \sqrt{3J_2} = \frac{1}{\sqrt{2}}\left[(\sigma_{11}-\sigma_{22})^2 + (\sigma_{22}-\sigma_{33})^2 + (\sigma_{33}-\sigma_{11})^2 + 6\left(\sigma_{12}{}^2 + \sigma_{23}{}^2 + \sigma_{31}{}^2\right)\right]^{\frac{1}{2}} = Y \quad (2.2)$$

where Y is the yield stress determined from the simple tensile test. The yield criterion based on the J_2 plasticity theory has the following assumptions:

(a) the material is isotropic and homogeneous,

(b) hydrostatic stress does not have any effect on yielding,

(c) volume is conserved and

(d) there is no strength differential (*S-D*) effect, with $S-D=2\left[\frac{|\sigma_c|-|\sigma_t|}{|\sigma_c|+|\sigma_t|}\right]$,

where σ_c and σ_t are the compressive and tensile strength, respectively.

Most of the work in the past [e.g. 1, 4-5, 7, 14-16] assumed that the simple tensile test introduces a uni-axial stress state in the gauge section, which ignores the transverse normal stresses (σ_{22} and σ_{33}) and all shear stresses (σ_{12}, σ_{23} and σ_{31}). As a result, the constitutive equation for stress and strain used in the FE simulation was often based on true axial stress-strain curve, determined directly from the simple tensile test. Later, however, it was found that the ignorance of transverse normal stresses has caused inconsistency between simulation and experimental behaviour [1, 7, 14-16]. Consequently, various schemes were proposed to determine the correct constitutive equation for the FE simulation [4-5]. The scheme used in the current study was slightly modified from that given in ref. [5].

The constitutive equation for the FE simulation is based on equation 2.1. In the original scheme presented in ref. [5], values for the parameters in equation 2.1 were selected in such a way that the corresponding stress-strain input curve fits the experimentally determined uni-axial stress-strain curve and satisfies continuity of the first derivative at ε_y, ε_n, and ε_t. FE model with this constitutive equation is used to generate the uni-axial engineering stress-elongation curve, which is compared with the experimental counterpart. Through iteration, discrepancy between the two curves is minimized by adjusting values for parameters in equation 2.1. The modified approach used in the current study is based on the same principle, but applies the iteration to each section of the stress-strain curve. That is, Young's modulus E in equation 2.1(a) is adjusted first to have the linear section of the FE-generated engineering stress-elongation curve be identical to that determined from the experiment. The process is then applied to equation 2.1(b) for the strain range from ε_y to ε_n, and then to equation 2.1(c) for the strain range from ε_n to ε_t. However, it was found that no matter what values were selected for parameters in equation 2.1(c), the engineering stress-elongation curve generated from the FE model could not match the experimental curve without sacrificing the accuracy of the cross section reduction predicted from the FE

model (the second criterion described earlier). In other words, if the FE-generated engineering stress-elongation curve were matched to the experimental curve, the cross section in the FE model would be reduced much more than that measured experimentally. This was later found to be due to the ignorance of time-dependent deformation that must have occurred during the testing. Since glass transition temperature of HDPE is below -50^{o}C, time-dependent deformation is unavoidable at room temperature. However, with the neck evolvement, thus improvement of molecular chain alignment in the loading direction [29], the time-dependent deformation will eventually become negligible. As a result, the creep model was considered in the FE simulation, to reconcile the difference with the experimental measurement. But, the creep model was considered only during the initial necking process, not after the neck initiation was completed.

Creep model introduced in the FE simulation is based on the following strain rate function, expressed in terms of the power-law expression of stress and time [28]:

$$\dot{\bar{\varepsilon}}^{cr} = A\tilde{q}^{n}t^{m} \tag{2.3}$$

where, $\dot{\bar{\varepsilon}}^{cr}$ is the uni-axial-equivalent creep strain rate, $\tilde{q}$ the von-Mises-equivalent stress, t time measured from the onset of necking, and A, n,

and m the user-defined constants for which values were selected through a trial-and-error process. As to be shown in the next section "2.3 Results and discussion," the above function is sufficient to adjust the engineering stress-elongation curve from the FE model so that it could match the experimental curve using only one set of A, n, and m values for each type of HDPE.

Note that the creep model was introduced only during the neck initiation, i.e. during the initial stress-drop section in the engineering stress-elongation curve, but not during the neck propagation. This is because molecular chains in a fully-developed neck should be well aligned in the loading direction [29]. Therefore, their time-dependent deformation behaviour should become negligible. Although time-dependent deformation could still occur at the neck propagation stage, in sections of the specimen other than that for the neck initiation, such deformation only causes increase of elongation in the flow-stress section of the engineering stress-elongation curve, not affecting the level of flow stress that is used as a criterion to validate the FE model. Therefore, ignorance of creep deformation at the neck propagation stage should not affect accuracy of the constitutive equation. Creep deformation was not introduced before the maximum

stress mainly to save computational time, as creep deformation should not be significant at that stage.

It should also be noted that for the two HDPEs used in this study, work hardening at the strain range for equation 2.1(d) was so significant that one set of parameter values for the equation was insufficient to introduce the required stress increase with the increase of deformation to match the experimental data. Instead, a minimum of four sets of values are needed for equation 2.1(d), with β kept constant at 1.8 (as recommended in ref. [5]) but different k and M values. As to be shown later, the use of four sets of parameters for equation 2.1(d) provides sufficient strain hardening in the constitutive equation, in order to reproduce the flow stress and the cross sectional reduction obtained from the experimental testing. The main advantage of the current approach over that used previously [4-5] is that the former provides mathematical expression for the constitutive relationship between stress and strain in order to facilitate future analysis of deformation when subjected to multi-axial loading; while the latter only discrete data points.

2.3 Results and discussion

Experimental

Typical plots of engineering stress versus elongation for different specimen thicknesses are presented in Figures 2-3(a) and 2-3(b) for PE1 and PE2, respectively. In general, variation of specimen thickness does not affect the curves up to the maximum point, with PE1 giving higher values of maximum engineering stress than PE2. After the maximum point, the curves show dependence on the specimen thickness, as characterized by the onset of neck propagation (point F in Figure 2-4), flow stress level, and elongation at break. The general trend is that with decrease in specimen thickness, elongation at point F decreases, but flow stress and elongation at break increase as shown in Table 2-2. Table 2-2 also shows the standard deviation of some critical measurements for each curve of Figure 2-3, which clearly indicate the repeatability of experimental data.

Neck evolvement during the test is characterized by the change of width (W) and thickness (t) during the test, after normalization with their original dimensions (W_o and t_o, respectively). The ratio of normalized width to normalized thickness

(named χ here) is plotted as a function of elongation in Figures 2-5(a) and 2-5(b), for PE1 and PE2, respectively. Those plots clearly indicate that with the decrease of specimen thickness, the difference between width contraction and thickness contraction is enlarged during the necking.

Percentage of the width reduction and the thickness reduction at point *F* (Figure 2-4), $(1-W_f/W_o)$ and $(1-t_f/t_o)$, respectively, and the corresponding reduction in cross sectional area $(1-A_f/A_o)$ are presented in Figure 2-6 as functions of specimen thickness. It is worth pointing out that variations of width and thickness with the change of initial specimen thickness are in an opposite trend, but the two trends converge at specimen thickness around 13 mm. This is consistent with the expectation, as the aspect ratio for specimens of 13 mm thick should be around 1, thus showing no distinction in contraction between the two directions. Figure 2-6 also suggests that the reduction of cross sectional area $(1-A_f/A_o)$ increases with decrease of specimen thickness, though the change is relatively small compared to that for the width and thickness. Note that a similar trend of dimensional contraction was also reported for PC/ABS blends [10], also attributed to the

change of aspect ratio of the cross section, but without any further explanation for the phenomenon.

In addition to the experimental data, Figure 2-5 contains curves that were generated using the following equation to express χ as a function of elongation. The equation was adopted from the expression that is commonly used for the gain of Butterworth filter [30-31], and with slight modification the experimental data can be fit by choosing suitable values for the constants. The expression captures the pattern of our data very well, though the data have nothing to do with the filtering function.

$$\chi = \frac{W/W_0}{t/t_0} = \left[\chi_f - \left\{ \frac{1}{\sqrt{\left[\{1-10^{\left(\frac{T-S}{K}\right)}\}^2 + \xi \times 10^{\left(\frac{T-S}{K}\right)} \right]}} \right\} \times (\chi_f - 1) \right] \tag{2.4}$$

in which K, ξ and S are adjusting factors, mainly for slope, curvature and horizontal shift, respectively, T is the elongation after normalization with the crosshead speed (i.e. $T = \frac{Elongation}{Crosshead\ speed} \times 60$, where crosshead speed is 100 mm/min), and χ_f is χ value at point F shown in Figure 2-4. Table 2-3 summarizes values for K, ξ and S selected in this study in order for the curves to fit the

experimental data. The values indicate that for a given HDPE, ξ and S can be kept constant. Only K needs to be changed with specimen thickness to fit the experimental data.

Using χ from equation 2.4 to take into account the difference in contraction between the width and the thickness directions, axial true stress and strain values could be determined from the following equations, based on the measured load (P) and specimen width (W), with the assumption that volume is conserved during the plastic deformation.

$$\sigma_{true} = P \frac{W_o}{t_o} \frac{\chi}{W^2} \tag{2.5a}$$

$$\varepsilon_{true} = 2 \ln\left[\frac{W_o}{W}\right] + \ln[\chi] \tag{2.5b}$$

Figure 2-7 presents typical true axial stress-strain curves from the two HDPEs of different thickness. The figure suggests that the change in specimen thickness has little effect on the stress-strain curve. Since thinner specimens show higher flow stress and more cross section contraction, values for the maximum axial stress and strain at the point for the onset of neck growth are expected to be the largest for the thinnest specimens.

Figure 2-8 expresses the rate of neck length increase (Ω) as a function of specimen thickness for both PE1 and PE2. The figure suggests that the neck growth rate (represented by Ω value) decreases with the decrease of specimen thickness for both HDPEs, with Ω value for PE2 being slightly higher than PE1. Since flow stress increases with decrease of specimen thickness, with the opposite trend for Ω, results from the experimental measurement suggest that the thinner specimens provide higher resistance to the neck growth.

Numerical simulation

Following the simulation procedure described in section II, values for parameters in equations 2.1 and 2.3 are listed in Tables 2-4 and 2-5, respectively. An example of the neck formation in the FE model is given in Figure 2-9 which was generated at elongation of 80 mm, using parameter values for 10-mm-thick PE1.

As mentioned earlier, the FE model for purely elastic-plastic deformation cannot generate both engineering stress-elongation curve and cross sectional reduction that match those obtained experimentally. This was confirmed after numerous trials using different sets of values for parameters in equation 2.1. Examples of the engineering stress-elongation curve generated by the FE model for purely

elastic-plastic deformation are presented in Figure 2-10 (+), and compared with the experimental curve (—) from a 10-mm-thick PE1 specimen and another FE-generated curve (○) with the consideration of creep deformation. Both FE -generated curves in Figure 2-10 are from FE models that can mimic correctly the cross sectional reduction observed experimentally. However, the one without creep does not match the experimental curve in the stress-drop section after the maximum point. Only with the creep deformation can the stress drop section be identical to that from the experiment.

Figure 2-11 compares the engineering stress-elongation curves for both HDPEs in two different thicknesses, 10 and 3 mm. With the consideration of creep, the FE-generated curve reproduces the experimental curve correctly, matching the stress drop section, elongation for on-set of neck propagation (point F in Figure 2-4), and flow stress level. Results from the FE model can also distinguish the small difference between two HDPEs in the stress level for the onset of neck propagation, 14 and 13 MPa for PE1 and PE2 of 10 mm thick, respectively, which are consistent with the values listed in Table 2-2.

Accuracy of the FE model for mimicking the deformation behaviour was evaluated by comparing the reduction of cross-sectional area during the necking process, for both 10- and 3-mm-thick specimens. As shown in Figure 2-12 in which the cross sectional area is normalized by its original value before the deformation, reasonable agreement is achieved for all comparisons.

Figure 2-13 presents a comparison of curves for true axial stress (σ_{11}) versus true strain between experiment and FE simulation, for 10- and 3-mm-thick specimens of both HDPEs. The experimental values (—) were calculated from load and cross sectional area at the cross section where neck was initiated, and the simulation counterparts (□) were determined in the same manner but from the FE model. The figure also includes curves of von Mises stress (Δ), which are used as the material property input for the FE simulation and presented here as reference for comparison. Note that the two σ_{11} curves in Figure 2-13 are very close to each other, which further supports the representation of FE simulation for the deformation of HDPEs. Closeness of von Mises stress to σ_{11} in Figure 2-13 suggests that σ_{11} dominates the von Mises stress value during the necking process. Based on the above comparisons, it is concluded that stress state determined from

the FE model can be used to analyze the effect of aspect ratio (by changing specimen thickness) on the stress state generated during the necking process.

Figure 2-14 presents variation of nodal values for transverse normal stresses (σ_{22} and σ_{33}) at the central point (point A in Figure 2-2) as a function of true strain (ε_{true}). Since shear stresses are very small and their variation during the necking insignificant, their data are omitted in those plots for clarity. Figure 2-14 demonstrates the significance of variation in the transverse normal stresses during the necking process. Further, it highlights the opposite trend of the change of transverse normal stresses with the change of specimen thickness, i.e., σ_{22} (in the width direction) increases with the decrease of specimen thickness but σ_{33} (in the thickness direction) decreases. It should be pointed out that the maximum difference between the two transverse normal stresses occurs when the cross section is close to its final dimensions, i.e. before the onset of neck propagation to the neighboring regions.

The opposite trend of the two transverse normal stresses with the change of specimen thickness, as shown in Figure 2-14, provides explanations for the opposite trend of contraction in the width and thickness directions shown in

Figure 2-6. That is, with the decrease in specimen thickness used for the tensile testing σ_{22} increases due to the increase in the resistance to deformation, resulting in bigger W_f/W_o value (i.e. smaller contraction in the width direction); while the opposite trend applies to σ_{33} and contraction in the thickness direction. Figure 2-14 also suggests that as the specimen thickness approaches zero, σ_{33} ceases, thus the plane-stress condition prevails.

G'Sell et al. [9] suggested that during the necking, variation of the stress state can be divided into two stages. The first stage occurs at the beginning of the neck formation when the neck front approaches to the cross section of interest. At this stage, the von Mises stress should be larger than the axial stress due to the transverse stress being compressive. At the second stage when the cross section is about to reach the final dimensions of the neck, however, the transverse normal stresses are tensile, thus the von Mises stress becomes smaller than the axial stress. This phenomenon is correctly predicted by the FE model, as shown in Figures 2-15(a) and (b) for variation of the stress components at two cross section locations, of 3.05 mm (Figure 2-15(a)) and 6.11 mm (Figure 2-15(b)) away from the neck initiation location, for 10-mm-thick PE1 specimen. Both figures in

Figure 2-15 show that the von Mises stress is larger than the axial stress at the beginning of the necking process where sharp stress drop occurs, but smaller at the later stage. The two figures also show that the transverse normal stress (σ_{22}) is compressive at the beginning of the necking process, but it becomes tensile later. Thus, the general trend presented in Figure 2-15 supports that suggested by G'Sell et al. [9].

It should be pointed out that the sharp drop of σ_{11} shown in both figures in Figure 2-15 was generated before the neck front reached the point of interest, i.e. 3.05 and 6.11 mm away from the initial necking position for Figures 2-15(a) and 2-15(b), respectively. The sharp drop of σ_{11} was caused by force decrease due to the localized deformation at the initial necking position, but little change of the cross sectional area (i.e. little strain change) at the point of interest. When the neck front reaches the point of interest, however, the cross sectional area is reduced, thus causing increase in both σ_{11} and strain values. As suggested in Figure 2-15, the onset of σ_{11} increase after its sharp drop occurs at strain levels about 0.43 and 0.32 for the locations of 3.05 and 6.11 mm, respectively, away from the initial necking position. In other words, further away is the point of

interest from the initial necking position, lower is the strain level at which the necking process commences at that point. This trend is consistent with the experimental observation in another study [5], and is attributed to the gradient of the cross-sectional reduction generated in the initial necking process.

Although results presented here are expressed as a function of thickness variation, similar effects should also occur by varying the specimen width to change the aspect ratio. This is expected because the HDPE plates were compression-molded, thus having isotropic mechanical properties.

2.4 Conclusions

The study provides information to quantify the influence of specimen thickness on the necking behaviour during uni-axial loading of HDPE. A 3-dimensional finite element model was developed to facilitate determination of the stress-strain relationship, and to provide explanations that elucidate the effect of aspect ratio of cross section on the necking process.

Experimental results show slight dependence of engineering stress-elongation curve on the change of specimen thickness. The results show that necking in thinner specimens generates higher reduction in thickness direction but lower in width direction. The axial stress-strain curve, however, has little variation by the change of specimen thickness, except the stress and strain values at the completion of the neck initiation process. The data suggest that resistance to neck propagation is highest for the thinnest specimens, as their neck growth speed is lowest and flow stress highest.

The work also provides the constitutive relationship between stress and strain that can be used in the FE simulation to mimic the necking process. It was found that time-dependent deformation needs to be considered in order to regenerate accurately the experimental deformation behaviour. A simple, time-hardening form of power law function was found to be sufficient to describe the creep deformation observed in the study, and only one parameter in the power law function depended on HDPE properties used in the simulation. Engineering stress versus elongation, true axial stress versus strain, and normalized cross sectional

area versus elongation curves, from the FE simulation, all show close agreement with the experimental results.

The FE simulation suggests that with the decrease of specimen thickness, normal stress in the thickness direction decreases, while that in the width direction increases. This is consistent with the experimental observation that with decrease in specimen thickness, reduction of the specimen thickness increases by the necking process, but reduction in specimen width decreases. Decrease in specimen thickness used for testing also resulted in the increase in the maximum true strain generated by the necking process, which is consistent with the expectation that when the plane-stress condition dominates the deformation, capability of the material to endure deformation increases.

Figures:

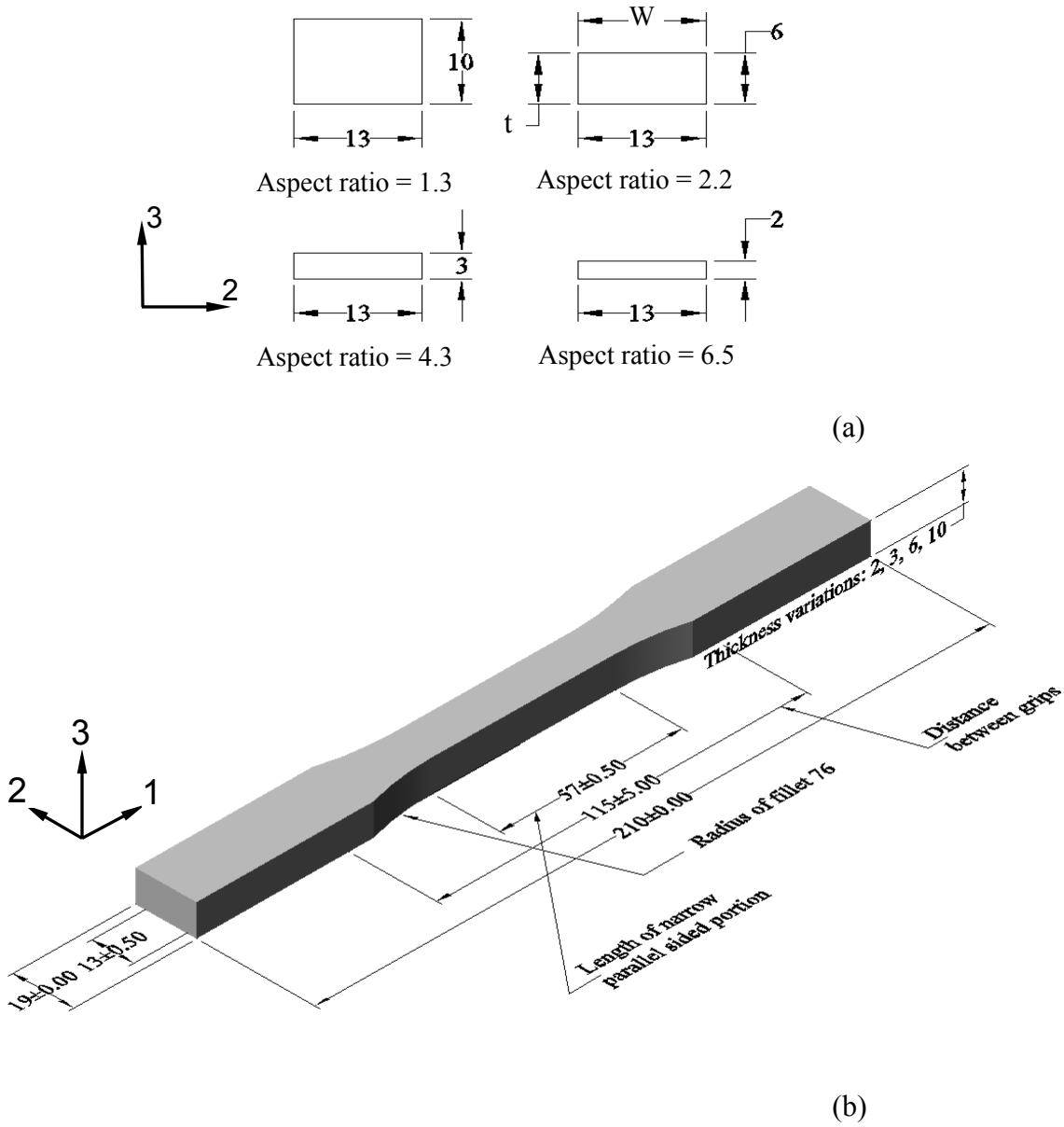

Figure 2-1 (a) Cross sectional dimensions for four different aspect ratios by change in thickness from 10 to 2 mm, and (b) other dimensions of the specimen according to ASTM D638 (Type 1).

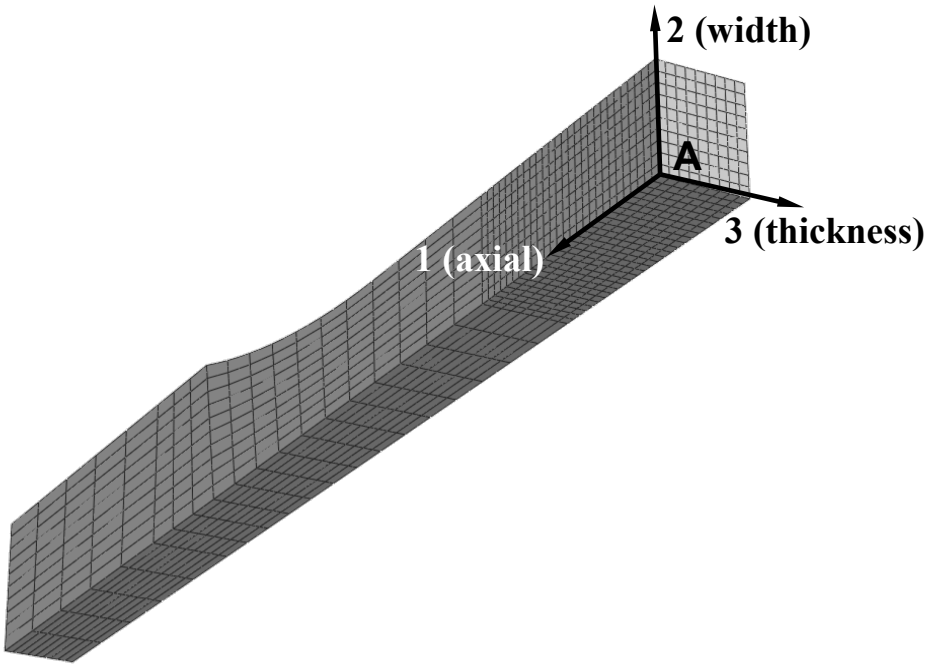

Figure 2-2 Example of un-deformed FE model with origin of the co-ordinate system set at point A.

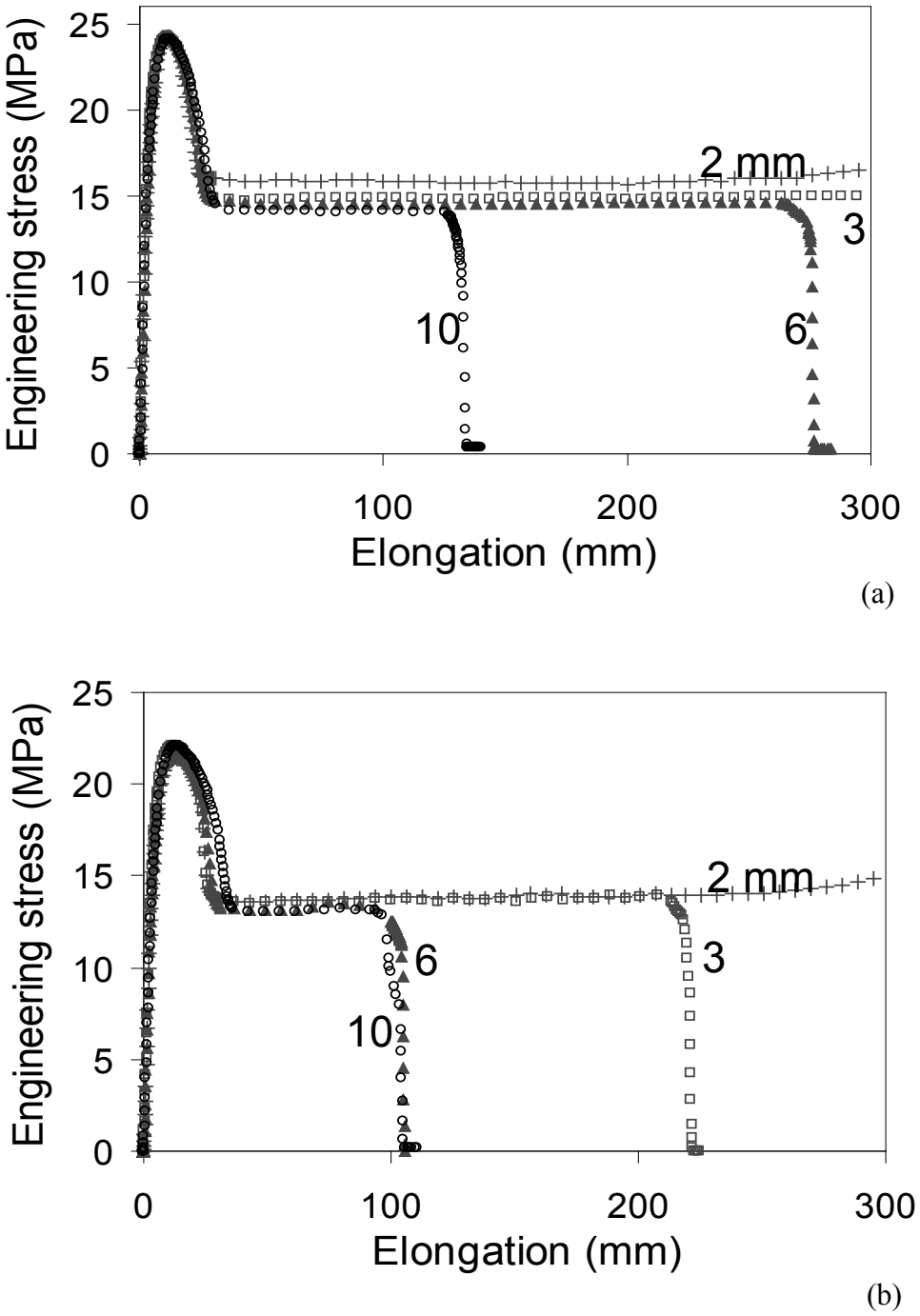

Figure 2-3 Engineering stress-elongation plots determined from experiments at cross-head speed of 100 mm/min, for PE1 (a) and PE2 (b) of various specimen thicknesses: 2 mm (+), 3 mm (□), 6 mm (▲), and 10 mm (○).

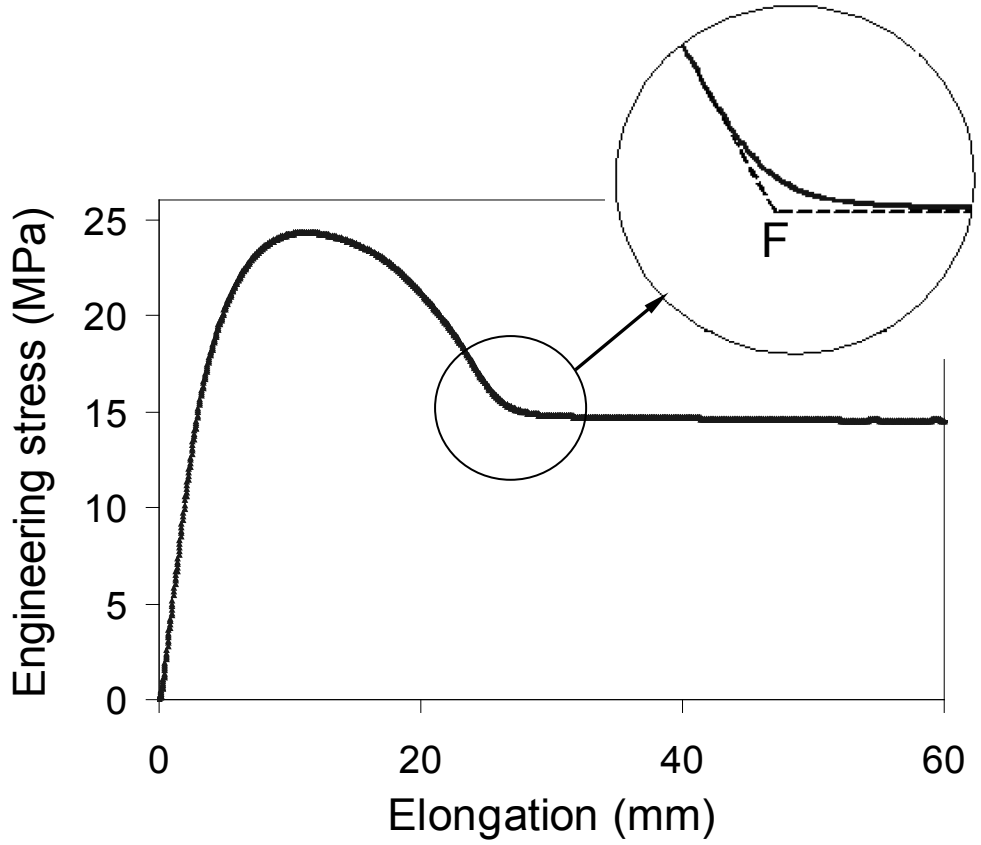

Figure 2-4 Location of the critical point (point F) for onset of neck growth on a typical engineering stress-elongation plot.

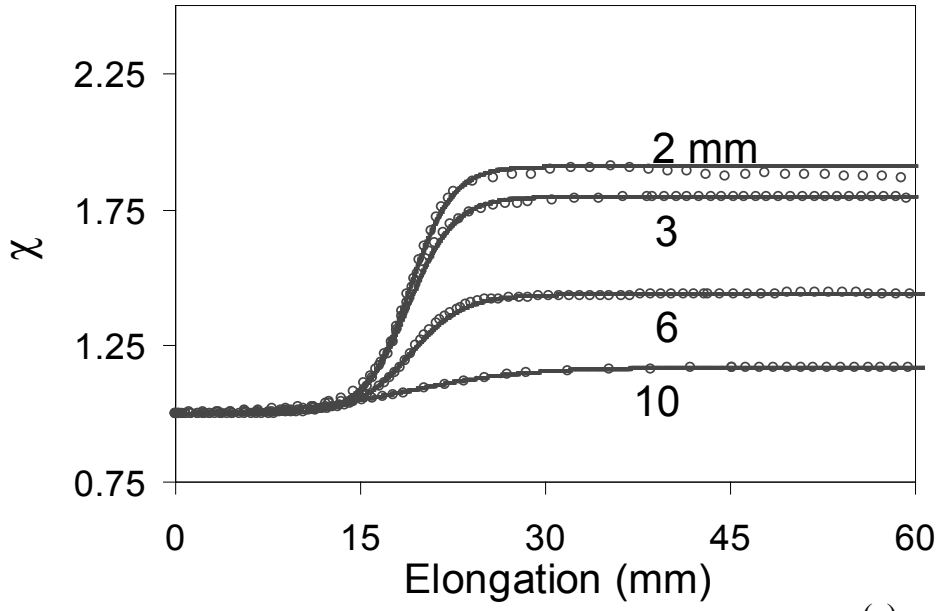

(a)

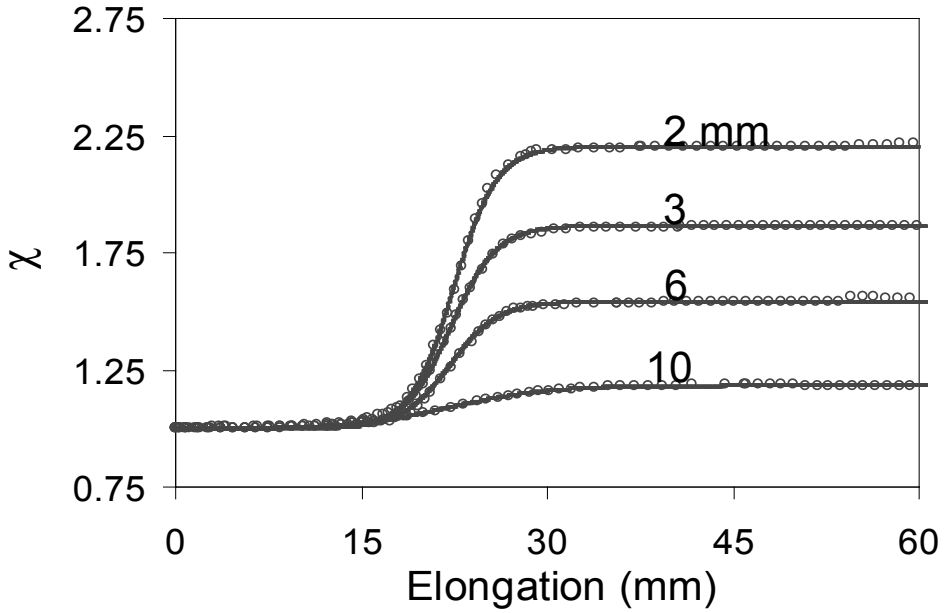

(b)

Figure 2-5 Plots of χ, defined as the ratio of normalized width (W/W_o) to normalized thickness (t/t_o), as a function of elongation from experimental data (○) and fitted data (—) using equation 2.4, for PE1 (a) and PE2 (b).

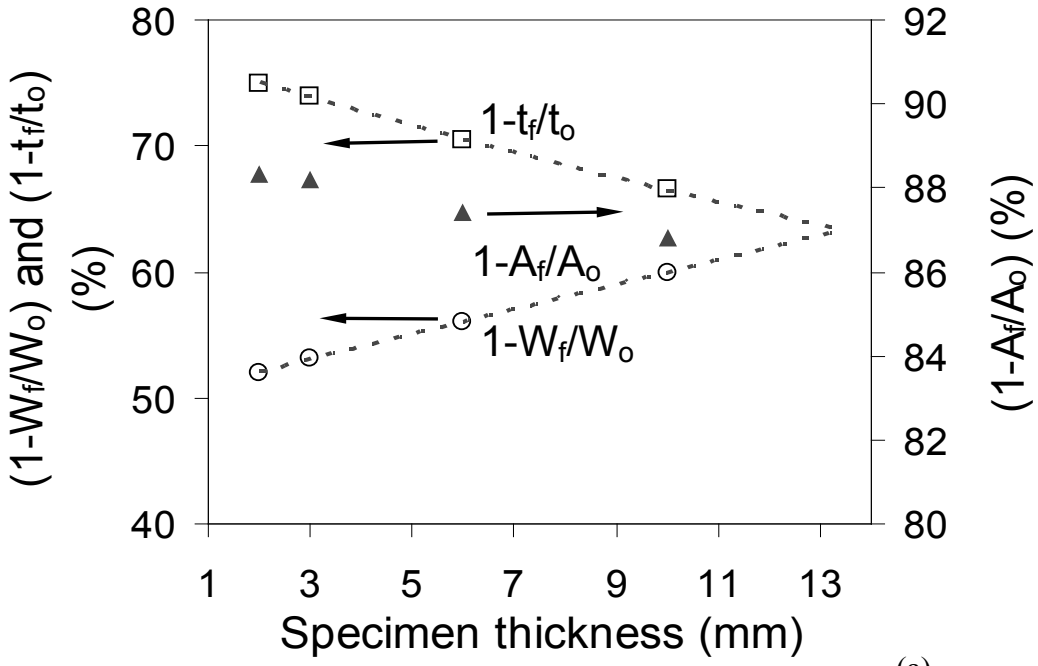

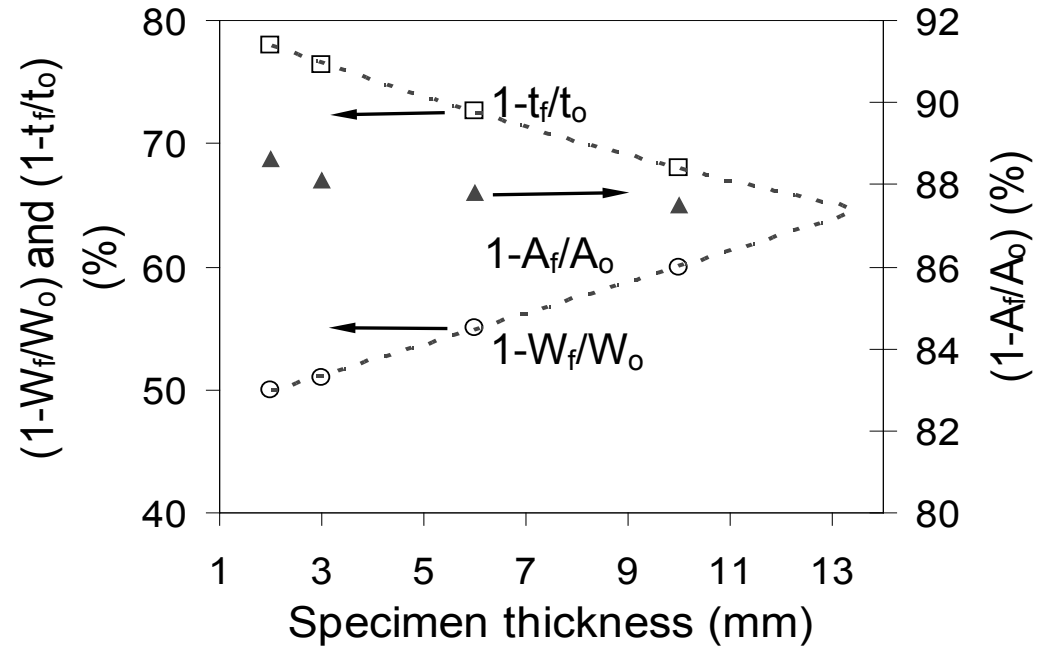

Figure 2-6 Experimental data for variation of reduction in normalized width (1-W_f/W_o) (○), normalized thickness (1-t_f/t_o) (□), and normalized area (1-A_f/A_o) (▲) as functions of specimen thickness, at the end of the neck formation but before its propagating to the neighboring region, for PE1 (a) and PE2 (b).

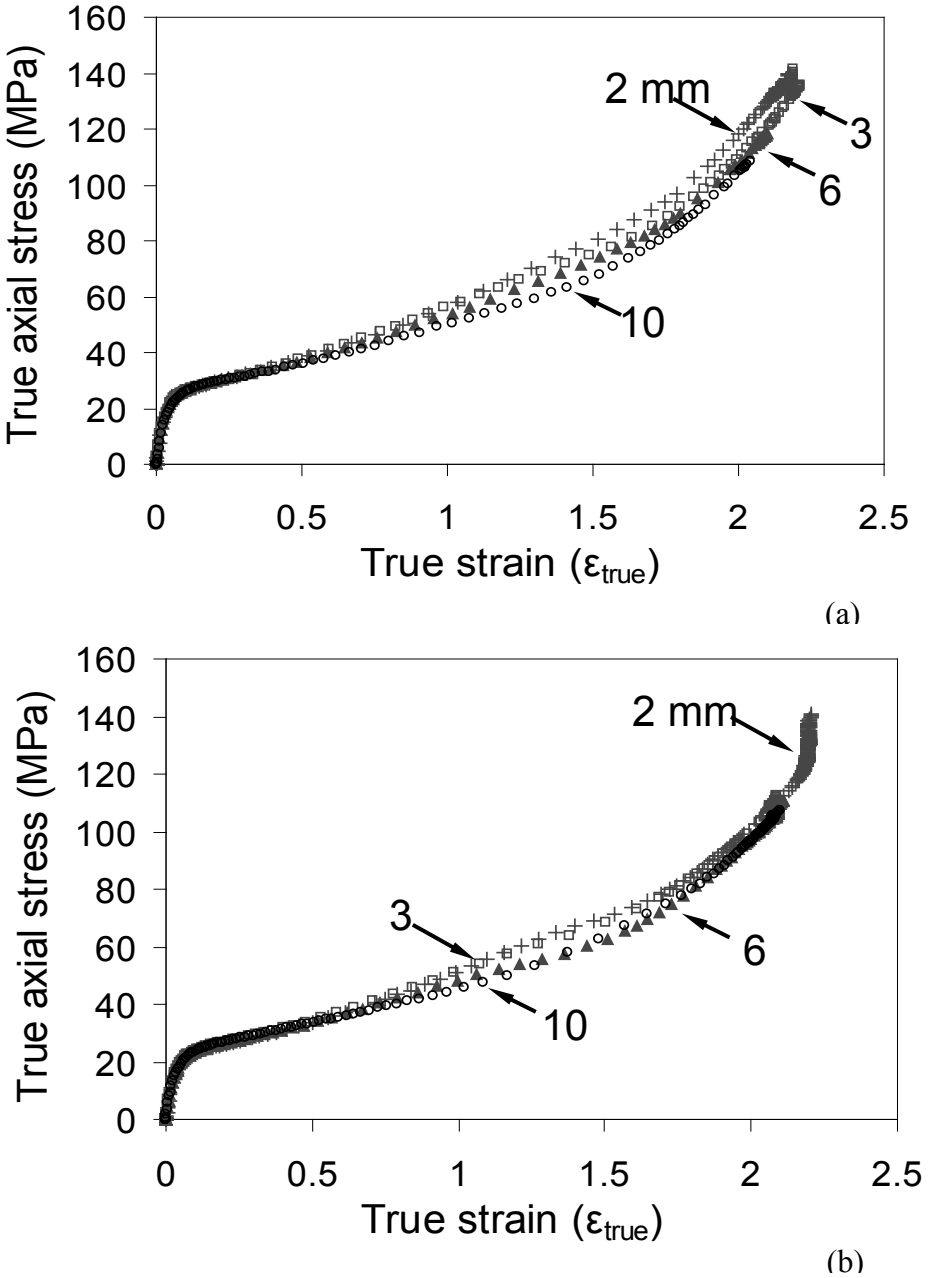

Figure 2-7 Experimental curves of true axial stress versus true strain for PE1 (a) and PE2 (b): 2 mm (+), 3 mm (□), 6 mm (▲), and 10 mm (○). Cross-head speed was 100 mm/min.

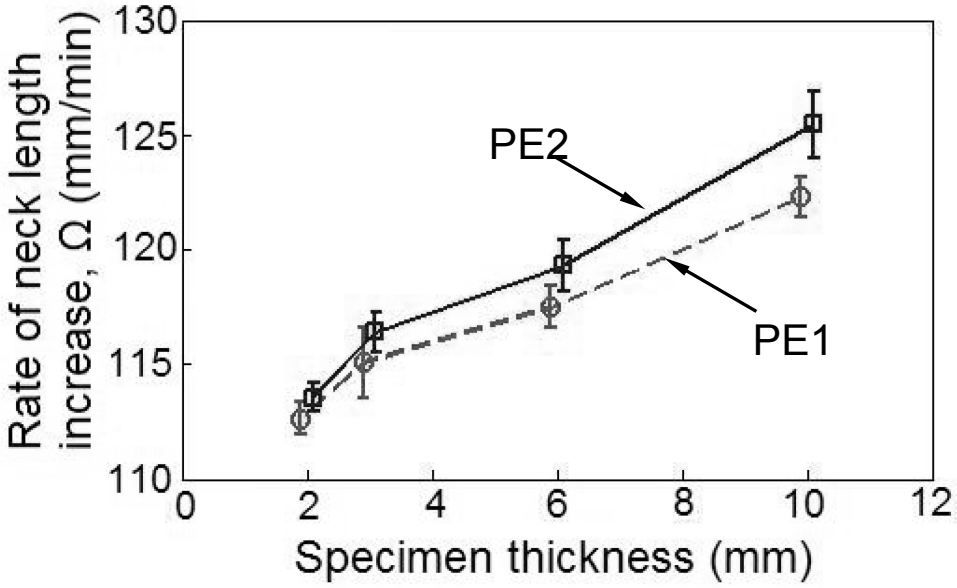

Figure 2-8 Plot of the measured rate of neck length increase (Ω) as a function of specimen thickness for PE1 and PE2 at cross-head speed of 100 mm/min.

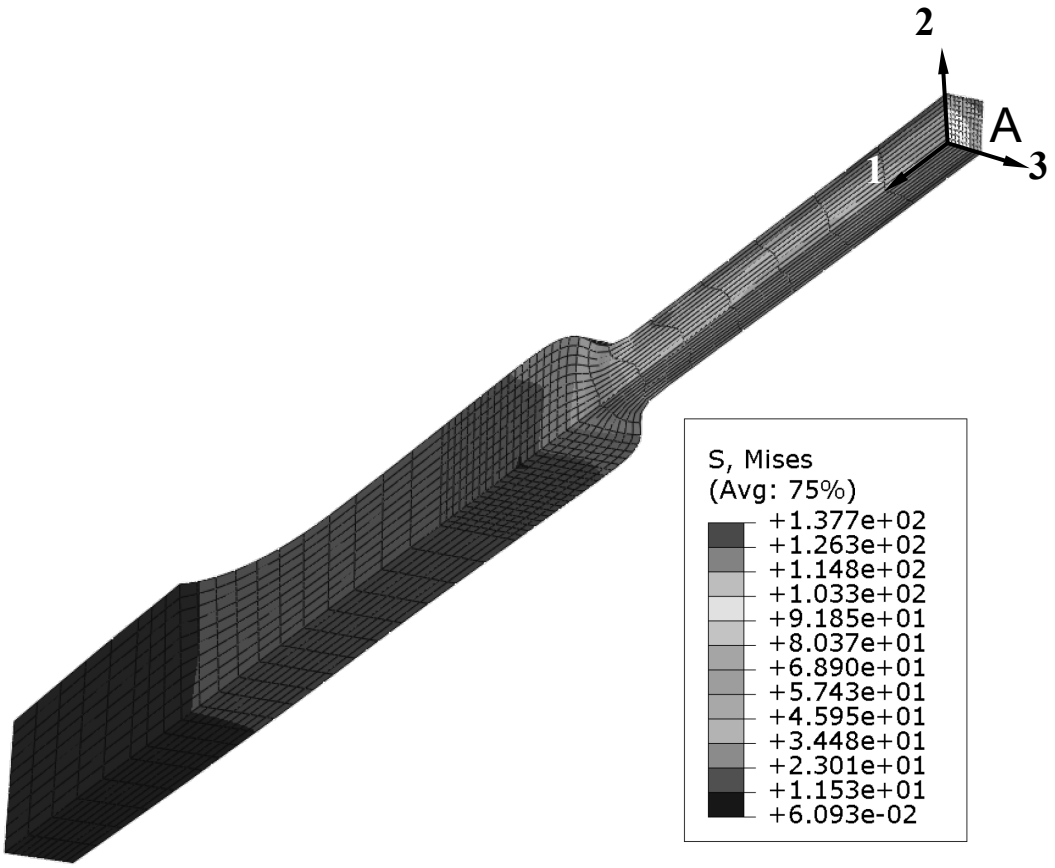

Figure 2-9 FE model for PE1 of 10 mm thick at elongation of 80 mm.

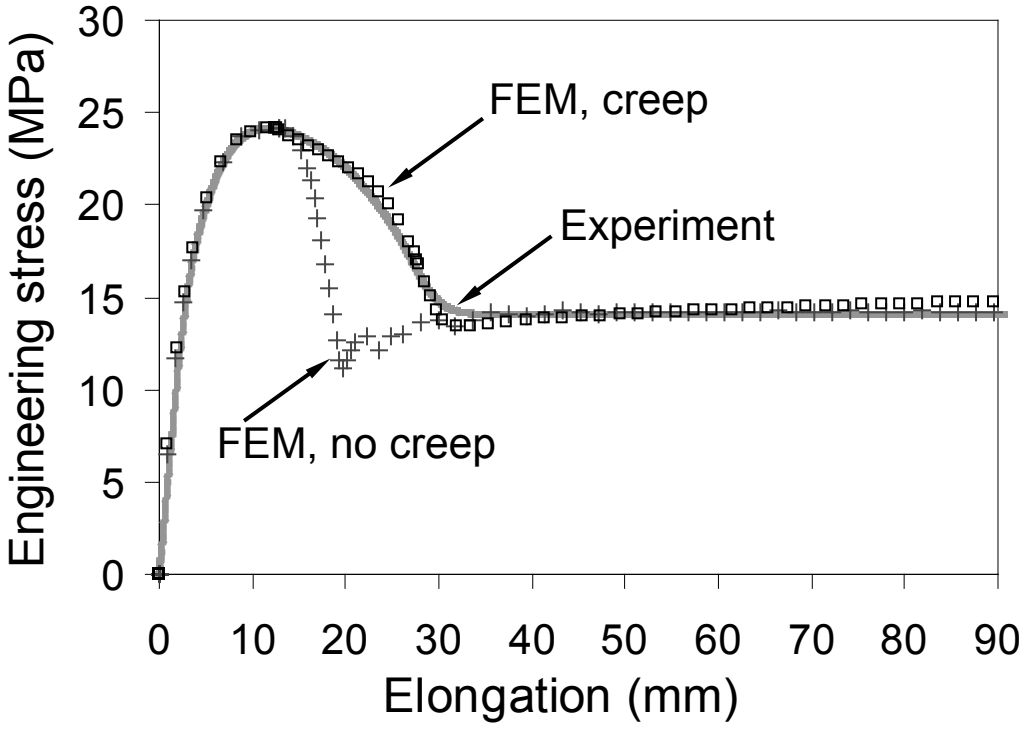

Figure 2-10 Comparison of engineering stress-elongation curve between experiment (▬) and FE simulation for PE1 of 10 mm thick. The latter is either with (□) or without (+) the consideration of creep.

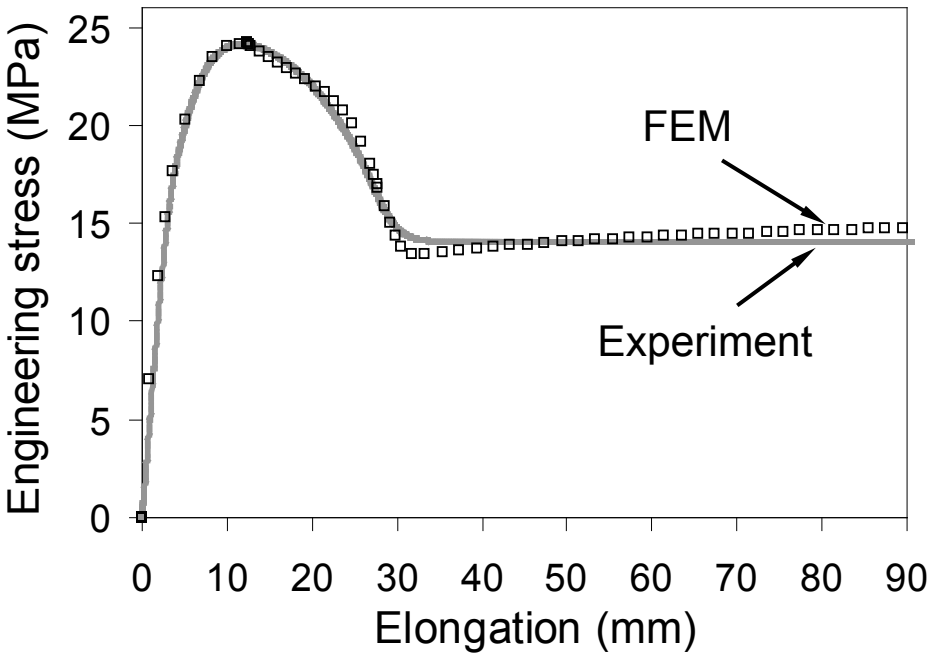
Engineering stress (MPa)
25
20
15
10
5
0
0
10
20
30
40
50
60
70
80
90
Elongation (mm)
FEM
Experiment

(a)

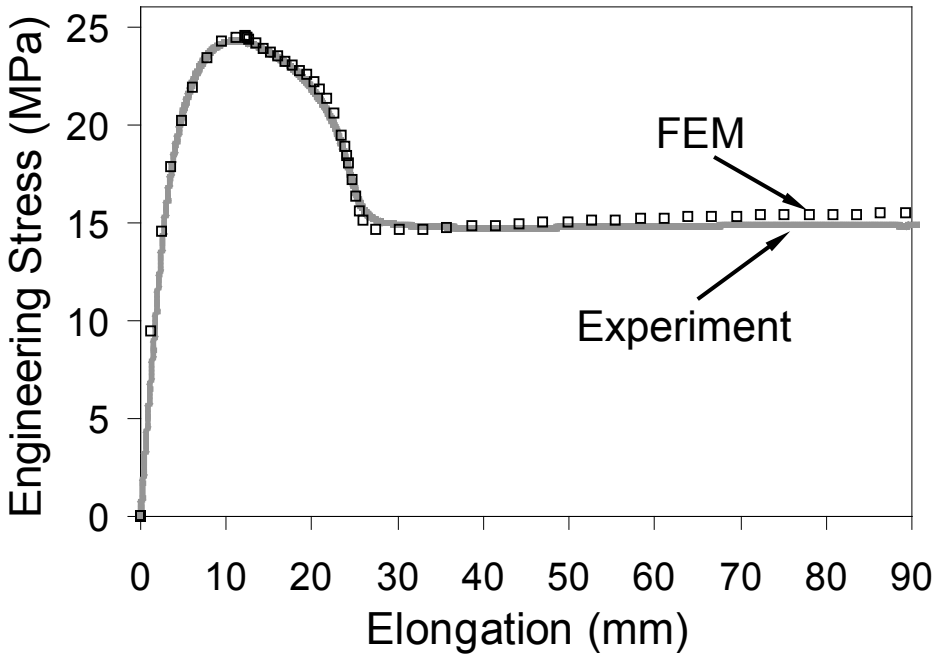
Engineering Stress (MPa)
25
20
15
10
5
0
0
10
20
30
40
50
60
70
80
90
Elongation (mm)
FEM
Experiment

(b)

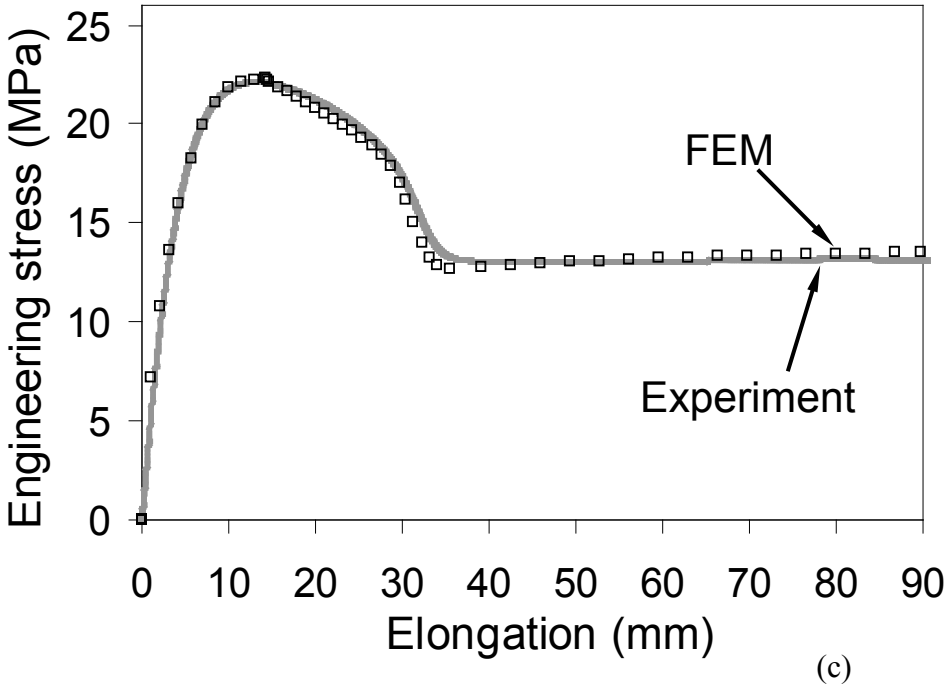

(c)

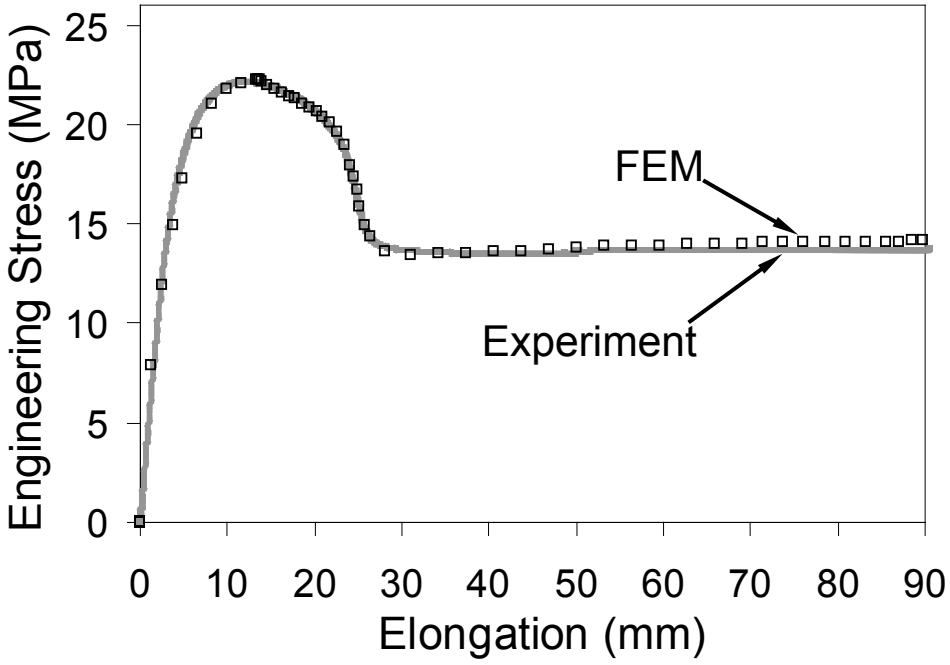

(d)

Figure 2-11 Comparison of engineering stress-elongation curve between experiment (▬) and simulation (□), for PE1 of 10 mm thick (a), PE1 of 3 mm (b), PE2 of 10 mm (c), and PE2 of 3 mm (d).

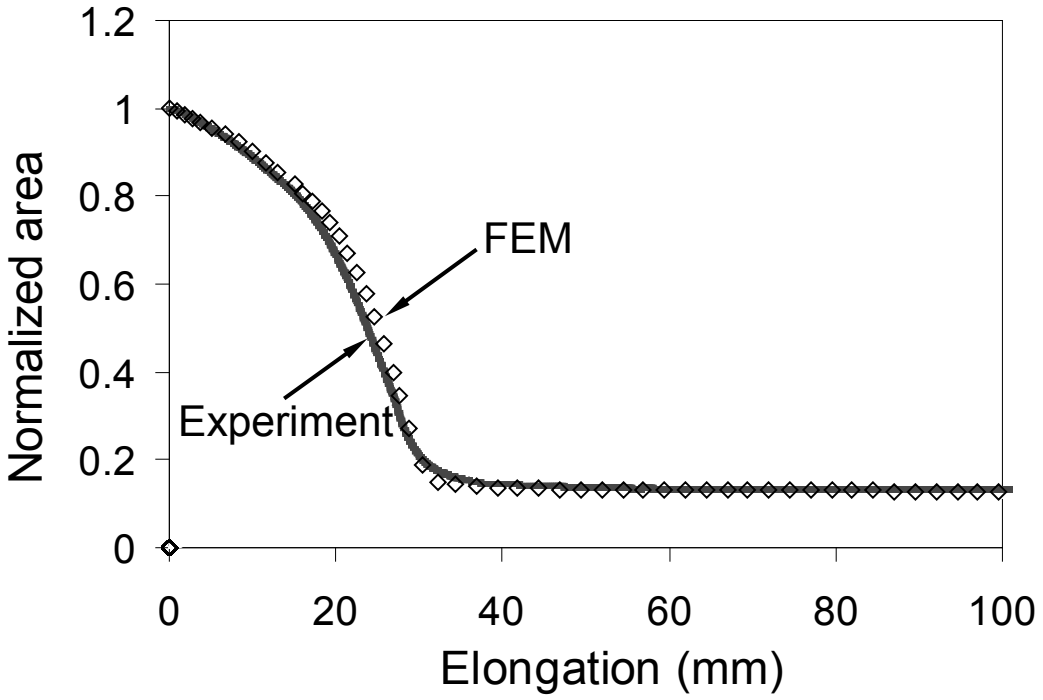
1.2
1
0.8
0.6
0.4
0.2
0
Normalized area
FEM
Experiment
0
20
40
60
80
100
Elongation (mm)

(a)

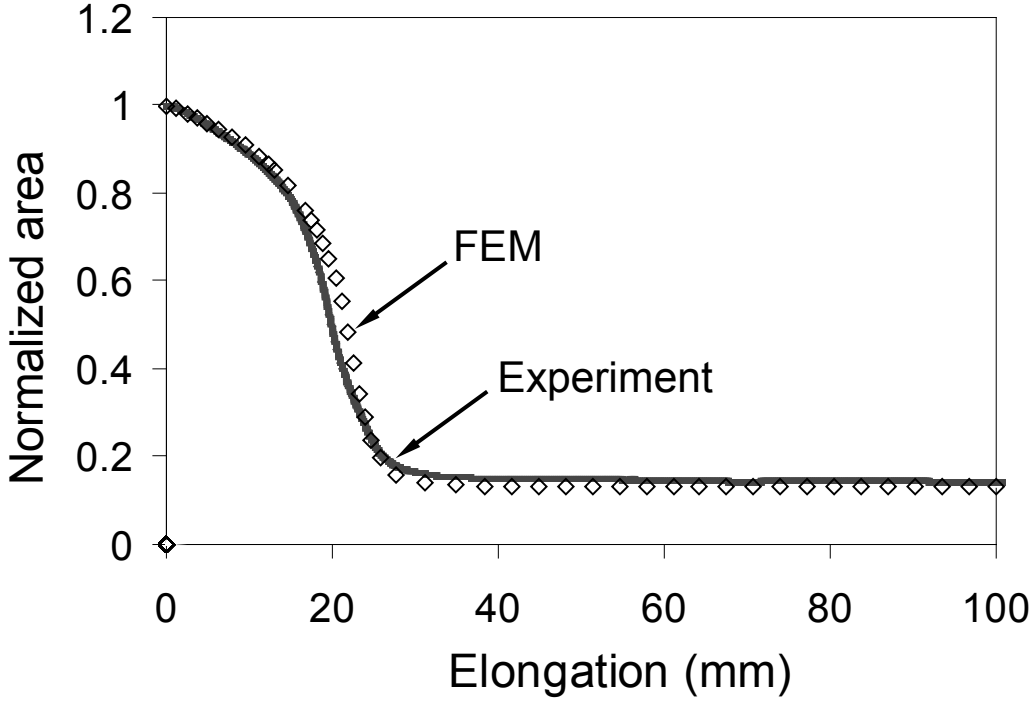
1.2
1
0.8
0.6
0.4
0.2
0
Normalized area
FEM
Experiment
0
20
40
60
80
100
Elongation (mm)

(b)

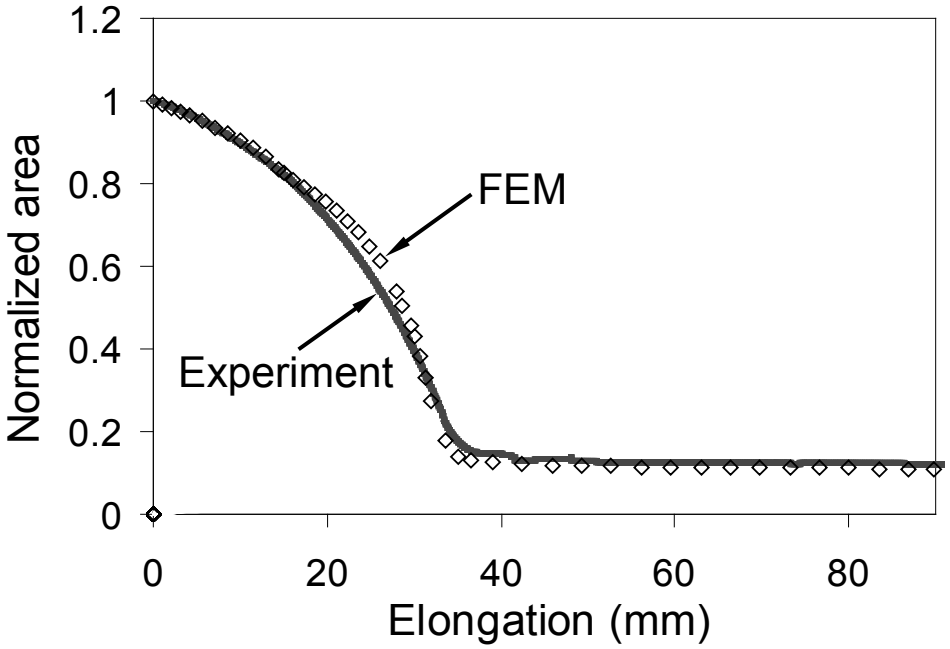

(c)

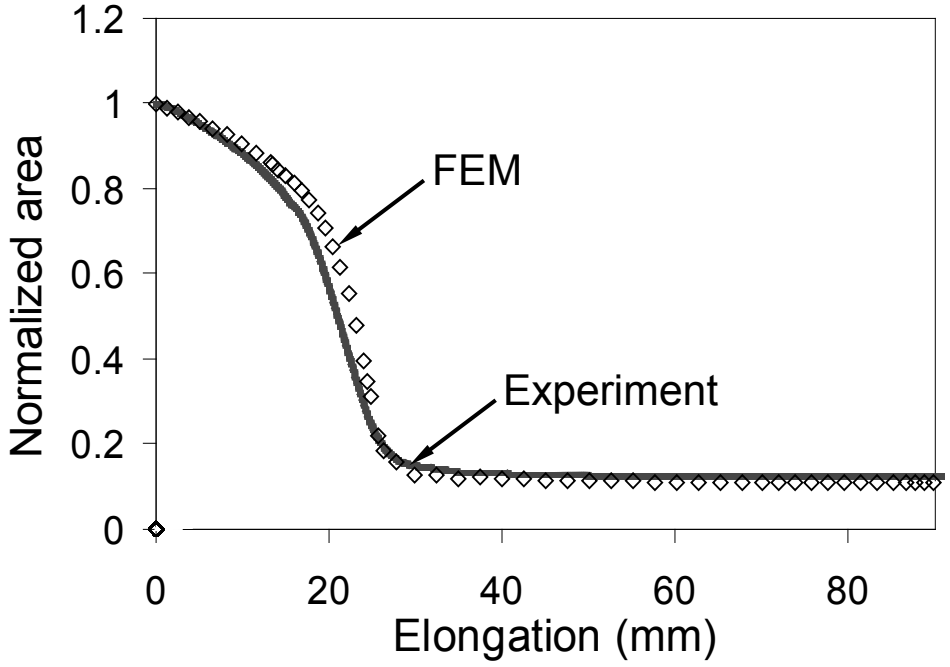

(d)

Figure 2-12 Comparison of the change of normalized cross sectional area at the initial necking section as a function of elongation between experiment (⎯⎯) and FE simulation (◊), for PE1 of 10 mm thick (a), PE1 of 3 mm (b), PE2 of 10 mm (c), and PE2 of 3 mm (d).

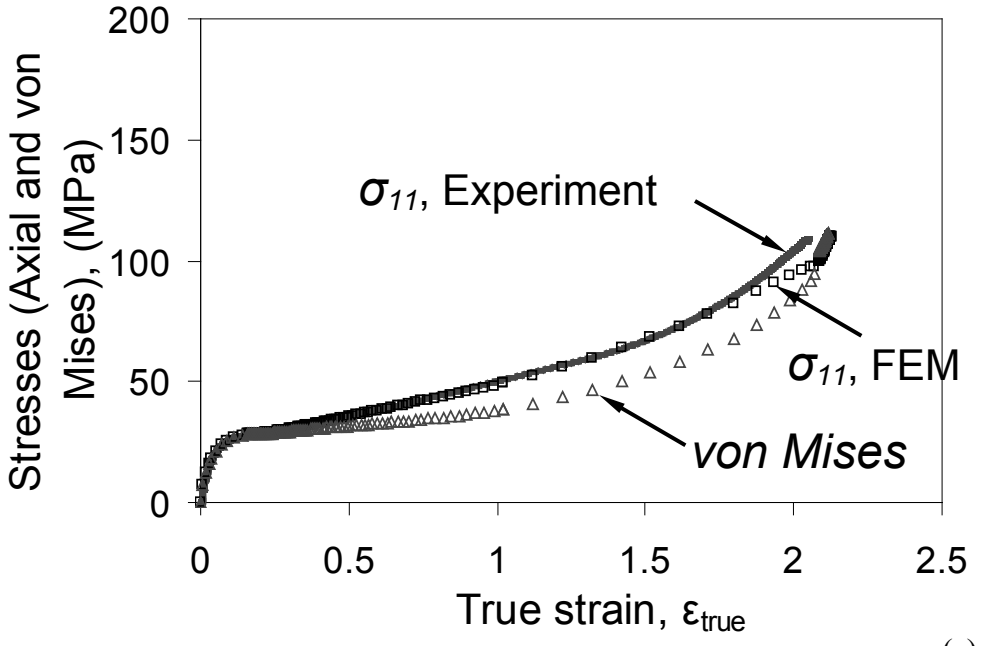
200
150
100
50
0
Stresses (Axial and von Mises), (MPa)
σ11, Experiment
σ11, FEM
von Mises
0
0.5
1
1.5
2
2.5
True strain, εtrue

(a)

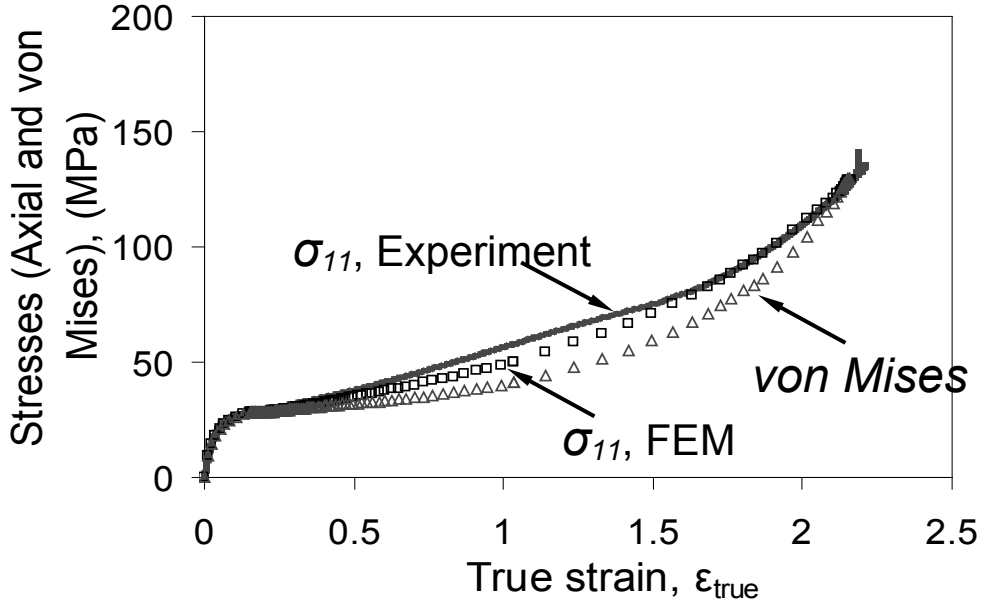
200
150
100
50
0
Stresses (Axial and von Mises), (MPa)
σ11, Experiment
von Mises
σ11, FEM
0
0.5
1
1.5
2
2.5
True strain, εtrue

(b)

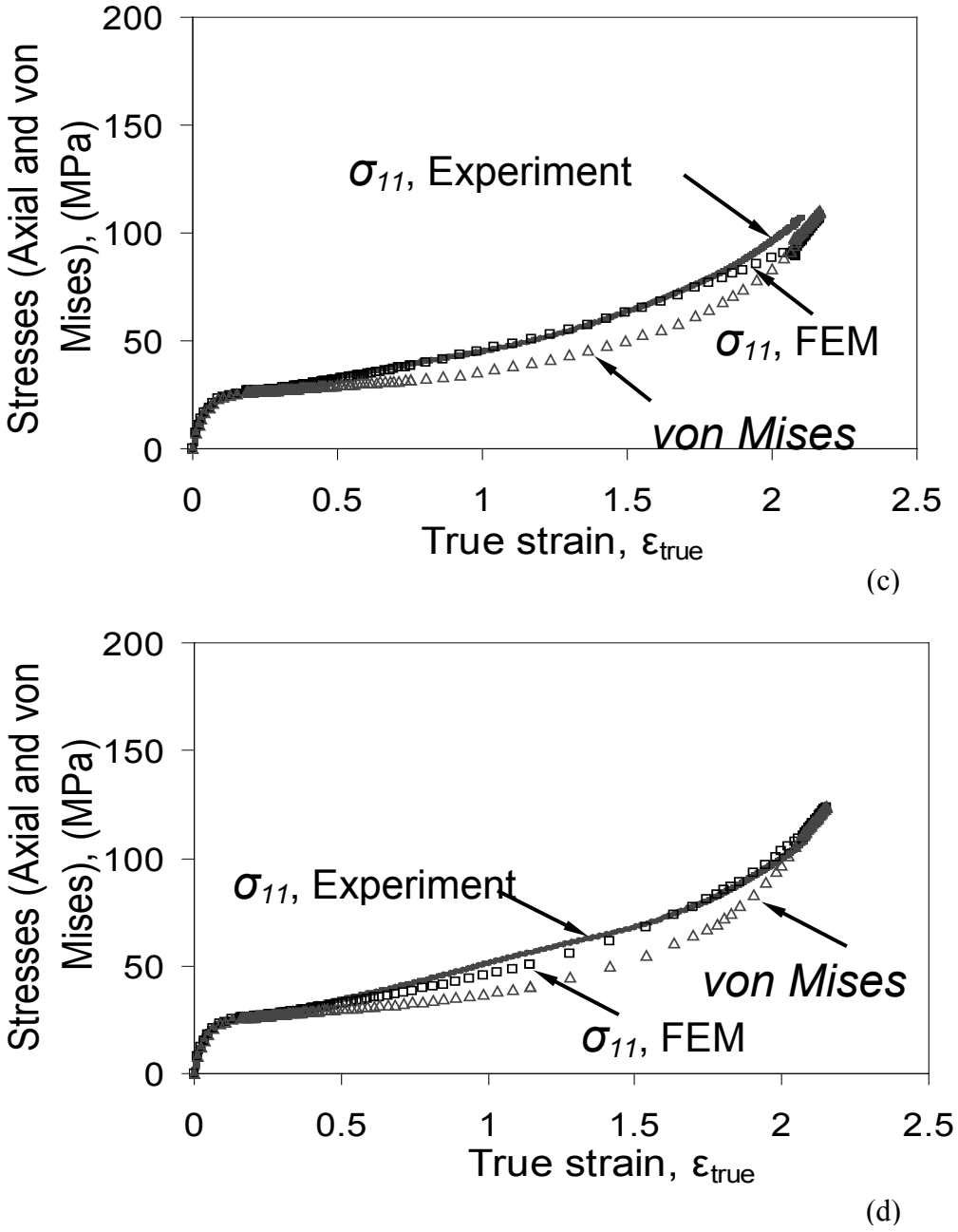

Figure 2-13 Plots of true axial stress (σ_{11}) versus true strain (ε_{true}) in the initial necking section, determined from experiment (⎯) and FE simulation (□) for PE1 of 10 mm thick (a), PE1 of 3 mm (b), PE2 of 10 mm (c), and PE2 of 3 mm (d). Curve of von Mises stress (∆) is also included as a reference. Note that the two curves for σ_{11} almost overlap with each other.

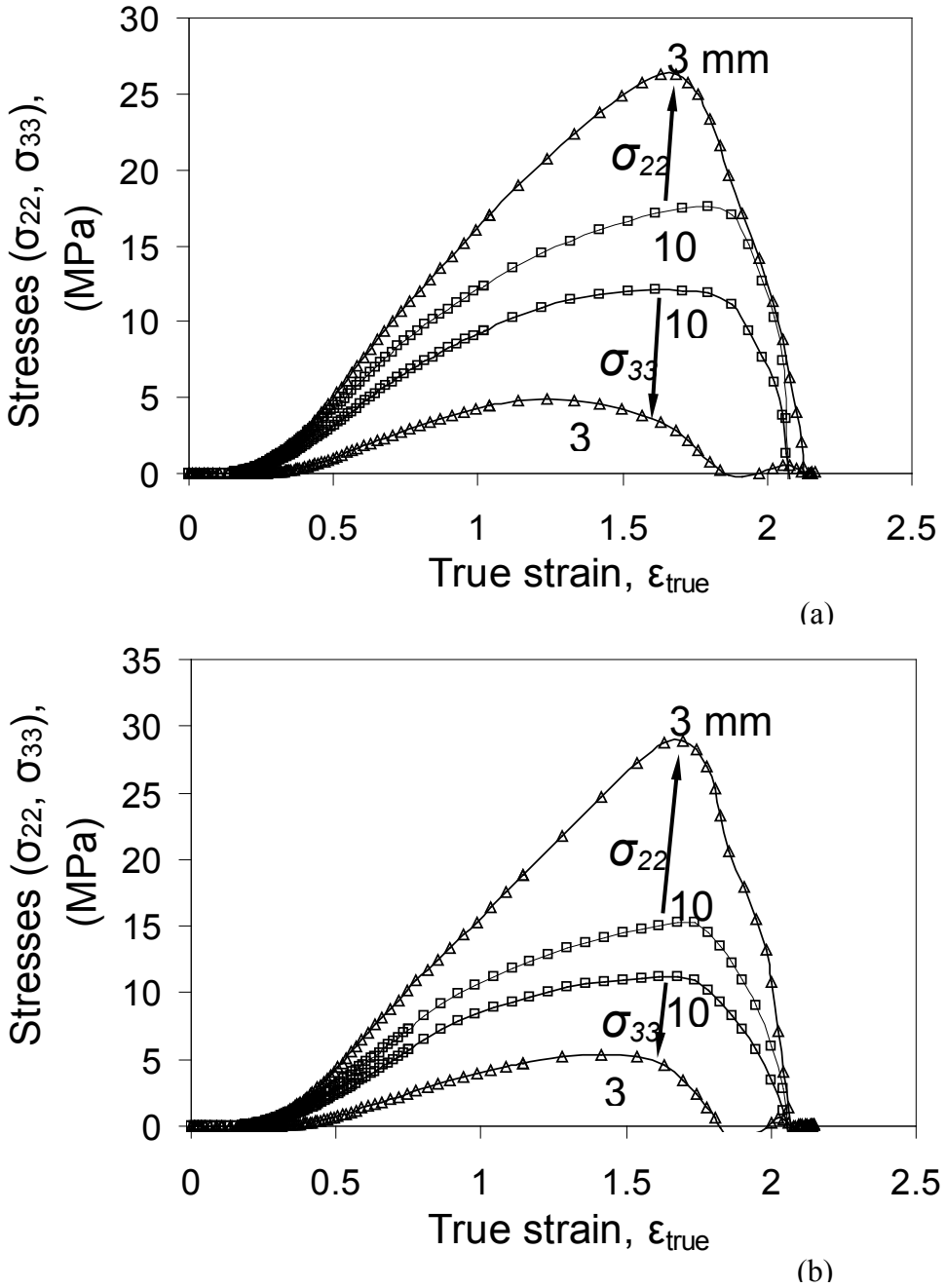

Figure 2-14 Plots of transverse normal stresses (σ_{22} and σ_{33}) at point A in Figure 2-2, as a function of true strain for PE1 (a) and PE2 (b), of 10 mm thick (□) and 3 mm thick (∆). Arrows in the figures indicate the direction of change with the decrease of specimen thickness.

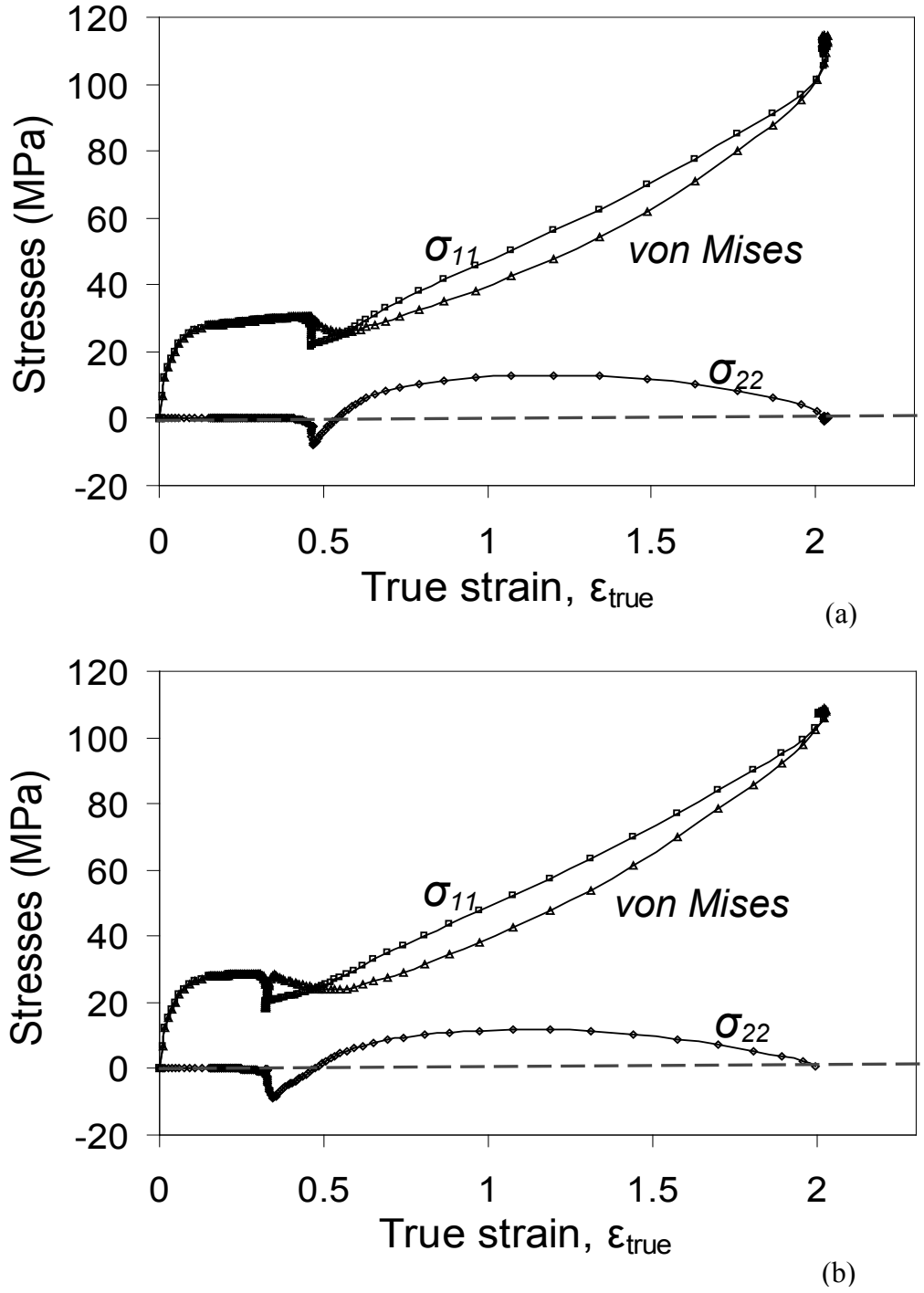

Figure 2-15 Plot of normal stresses (σ_{11} and σ_{22}) and von Mises stress obtained from FE simulation as a function of true strain at a section of 3.05 mm (a) and 6.11 mm (b) away from the initial necking position (where point A is located in Figure 2-2) for PE1 of 10 mm thick.

Tables:

Table 2-1 Material characteristics for HDPE used in this study.

Material designation	M_w (gm mol^{-1})	M_n (gm mol^{-1})	M_z (gm mol^{-1})	Density, ρ (gm cm^{-3})	M_w/M_n
PE1 (Hexene copolymer)	182000	17000	935000	0.945	10.6
PE2 (Octene copolymer)	73100	30400	147000	0.941	2.4

M_w: weight-average molecular weight,

M_n: number-average molecular weight, and

M_z: Z-average molecular weight

Table 2-2 Mean values (and standard deviation) of critical parameters, each based on six measurements.

Material	PE1				PE2			
Nominal Thickness (mm)	10	6	3	2	10	6	3	2
Maximum Engineering Stress (MPa)	24.1 (0.1)	24.3 (0.1)	24.3 (0.2)	24.5 (0.4)	22.4 (0.3)	22.2 (0.3)	22.3 (0.2)	22.1 (0.4)
Elongation for F (mm)	30.1 (0.4)	27.2 (0.8)	23.8 (1.8)	22.8 (1.2)	31.7 (2.4)	28.6 (1.7)	25.0 (1.4)	25.9 (0.4)
Flow stress (MPa)	14.0 (0.1)	14.4 (0.1)	15.0 (0.1)	15.8 (0.1)	13.2 (0.1)	13.2 (0.1)	13.7 (0.1)	14.0 (0.2)
Elongation at break (mm)	146 (12)	202 (45)	440 (27)	More than 500	89 (7)	106 (3)	169 (43)	More than 500

Table 2-3 Values for parameters in equation 2.4.

Material	PE1				PE2			
Nominal thickness (mm)	2	3	6	10	2	3	6	10
K	2.4	2.6	3	6.5	2.4	2.55	2.7	5.5
ξ	4	4	4	4	4	4	4	4
S	12	12	12	12	14	14	14	14
χ_f	1.91	1.80	1.44	1.17	2.20	1.87	1.54	1.19

Table 2-4 Values of parameters for equation 2.1.

Equation		parameters	Materials			
			PE1		PE2	
			Specimen thickness		Specimen thickness	
			10	3	10	3
2.1(a)		ε_n	0.078	0.078	0.080	0.074
		E (MPa)	800	800	800	800
		ν	0.35	0.35	0.35	0.35
2.1(b)		ε_y	0.013	0.013	0.008	0.008
		a	30	30	25	25
		b	0.015	0.015	0.025	0.025
		c	0.007	0.007	0.038	0.040
		d	-19	-19	-22	-23
		e	14	14	11	11
2.1(c)		ε_t	0.41	0.39	0.43	0.43
		αk	37	37	35	35
		N	0.14	0.14	0.16	0.16
2.1(d)	1st part	k	30	30	28	28
		M	0.4	0.4	0.4	0.4
		β	1.8	1.8	1.8	1.8
	2nd part	k	25	27	24	24
		M	0.5	0.5	0.5	0.5
		β	1.8	1.8	1.8	1.8
	3rd part	k	16	22	19	19
		M	0.7	0.6	0.6	0.60
		β	1.8	1.8	1.8	1.8
	4th part	k	5.9	19	10	10
		M	1.1	0.6	0.8	0.8
		β	1.8	1.8	1.8	1.8

Table 2-5 Values for parameters in equation 2.3.

Materials	Nominal thickness (mm)	*A*	*n*	*m*
PE1	10	1.75E-08	4.5	-0.5
	3	1.75E-08	4.5	-0.5
PE2	10	2.50E-08	4.5	-0.5
	3	2.50E-08	4.5	-0.5

References

1. Neale KW, Tugcu P (1985) Analysis of necking and neck propagation in polymeric materials. J. Mech. Phys. Solids 33:323-337

2. Boyce MC, Arruda EM (1990) An experimental and analytical investigation of the large strain compressive and tensile response of glassy polymers. Polym. Eng. Sci. 30:1288-1298

3. Wu PD, Van Der Giessen E (1995) On neck propagation in amorphous glassy polymers under plane strain tension. Int. J. Plasticity 11:211-235

4. Tomita Y, Hayashi K (1993) Thermo-elasto-viscoplastic deformation of polymeric bars under tension. Int. J. Solids Structures 30:225-235

5. Kwon HJ, Jar P-YB (2008) On the application of FEM to deformation of high-density polyethylene. Int. J. Solids Structures 45:3521-3543

6. Li HX, Buckley CP (2008) Evolution of strain localization in glassy polymers: A numerical study. Int. J. Solids Structures 46:1607-1623

7. Fager LO, Bassani JL (1986) Plane strain neck propagation. Int. J. Solids Structures 22:1243-1257

8. Masud A (2005) A 3-D model of cold drawing in engineering thermoplastics. Mech. Adv. Mater. Structures 12:457-469

9. G'Sell C, Aly-Helal NA, Jonas JJ (1983) Effect of stress triaxiality on neck propagation during the tensile stretching of solid polymers. J. Mater. Sci. 18:1731-1742

10. Fang QZ, Wang TJ, Beom HG, Zhao HP (2009) Rate-independent large deformation behavior of PC/ABS. Polymer 50:296-304

11. Buckley C, Costas M (2004) Neck propagation in polyethylene. J. Polym. Sci. Part B: Polym. Phys. 42:2081-2091

12. G'Sell C, Jonas JJ (1979) Determination of the plastic behavior of solid polymers at constant true strain rate. J. Mater. Sci. 14:583-591

13. Hutchinson JW, Neale KW (1983) Neck propagation. J. Mech. Phys. Solids 31:405-426.

14. Tugcu P, Neale KW (1987a) Analysis of plane-strain neck propagation viscoplastic polymeric films. Int. J. Mech. Sci. 29:793-805

15. Tugcu P, Neale KW (1987b) Necking and neck propagation in polymeric materials under plane-strain tension. Int. J. Solids Structures 23:1063-1085

16. Neale KW, Tugcu P (1988) Approximate methods for analyzing the cold drawing of polymeric fibres and films. Int. J. Numer. Methods Eng. 25:99-112

17. Peterlin A (1971) Molecular model of drawing polyethylene and polypropylene. J. Mater. Sci. 6:490-508

18. Kwon HJ, Jar P-YB (2007a) The application of essential work of fracture concept to toughness characterization of high-density polyethylene. Polym. Eng. Sci. 47:1327-1337

19. G'Sell C, Hiver JM, Dahoun A (2002) Experimental characterization of deformation damage in solid polymers under tension, and its interrelation with necking. Int. J. Solids Structures 39:3857-3872

20. Hill R (1952) On discontinuous plastic states, with special reference to localized necking in thin sheets. J. Mech. Phys. Solids 1:19-30

21. Bridgman PW (1944) Stress distribution at neck of tension specimen. Trans. Amer. Soc. Met. 32:553-572

22. Ogden RW (1972) Large deformation isotropic elasticity: on the correlation of theory and experimental for compressible rubberlike solids. Proceedings of the Royal Society of London, Series A (Mathematical and Physical Sciences) 328:567-83

23. Hollomon JH (1945) Trans. Metall. Soc. American Institute of Mining and Metallurgical Engineers 162:268-290

24. Spitzig WA, Sober RJ, Richmond O (1975) Pressure dependence of yielding and associated volume expansion in tempered martensite. ACTA Metallurgica 23:885-893

25. Raghava R, Caddell RM (1973) The macroscopic yield behavior of polymers. J. Mater. Sci. 8:225-232

26. Spitzig WA, Richmond O (1979) Effect of hydrostatic pressure on the deformation behavior of polyethylene and polycarbonate in tension and in compression. Polym. Eng. Sci. 19:1129-1139

27. Silano AA, Bhateja SK, Pae KD (1974) Effects of hydrostatic pressure on the mechanical behavior of polymers: polyurethane, polyoxymethylene, and branched polyethylene. Int. J. Polym. Mater. 3:117-131

28. "Rate-dependent plasticity: creep and swelling", Section 18.2.4, ABAQUS Analysis User's Manual. ABAQUS manual version 6.7 (2007) ABAQUS, Inc.

29. Peterlin A (1987) Drawing and extrusion of semi-crystalline polymers. Colloid Polym. Sci. 265:357-382

30. Bianchi G, Sorrentino R (2007) Electronic filter simulation and design. McGraw-Hill Companies, New York

31. Butterworth S (1930) On the theory of filter amplifiers. Experimental wireless and the wireless engineer 7:536-541

CHAPTER - 3

Determining Stress-Strain Relationship for Necking in Polymers based on Macro Deformation Behavior

3.1 Introduction and Background

Polymers such as high-density polyethylene (HDPE) are susceptible to spontaneous strain localization (commonly known as necking) and strain hardening that arises from structural rejuvenation induced by large deformation. In view that the ability to predict necking in polymers is essential for assurance of their reliable performance, especially when considering applications such as

pipelines and pressure vessels, understanding such deformation behavior is of utmost importance. As a result, much of the research work on polymers has been dedicated to study of the necking behavior and the damage evolution process during the neck development. However, challenges are encountered due to the time-dependent deformation process (such as creep) that plays a critical role for many polymers in long-term service. As a result, most of the characterization methods to evaluate reliability of the long-term performance of polymers require tests on full-sized products. Since those tests are time-consuming to carry out and involve significant uncertainty in its prediction accuracy, some researchers have considered a different approach that is to evaluate the performance through numerical simulation, for which the first step is to establish the stress-strain relationship for the deformation process.

During the last few decades many approaches have been proposed to establish the stress-strain relationship for polymer deformation. Some of those approaches, often known as slip-link or tube models [1], are an extension from classical rubber elasticity, to consider chain entanglements in the molecular network for the mechanical response during the deformation. One of those approaches,

commonly known as Edward-Vilgis theory [2], separates the number of permanent joints from the number of topological constraints in the expression of free energy as a function of stretch ratio. Based on this model, formation of cross links in radiated polyethylene was investigated and found to increase the effective chain entanglements during the deformation [3].

Other approaches consider interactions at the molecular level to relate the molecular interactions with the macroscopic deformation behavior. One of the first models in those approaches took into account rotation and alignment of molecular chain segments for establishing the stress-strain relationship for large deformation in amorphous polymers [4-5]. The model was later extended to three-dimensional deformation [6-7]. More recently, Wu and Buckley [8] developed a model based on molecular interaction to capture most of the features observed in ductile deformation of amorphous polymers. Based on a slightly larger scale, Drozdov and Christiansen [9] developed a model for a similar purpose, that is, to mimic plastic and visco-plastic deformation in semi-crystalline polymers.

A different approach, generally known as phenomenological models, was developed by considering mainly deformation at the macroscopic scale. Although early work, e.g. ref. [10-23], is limited to elastic-plastic deformation, advancement in this approach has shown the ability to mimic viscoelastic deformation [24-28], rate reversal behaviour in creep and relaxation [29], and dynamic response [30].

Work presented here is part of the phenomenological modeling approach that uses finite element (FE) technique to mimic deformation during the neck development. The previous publication [31] used a relatively simple set of equations to describe the input stress-strain relationship for the FE model, with values for unknown parameters determined using an iteration process. Based on this stress-strain relationship, the FE model was able to mimic the cross section contraction and load-displacement curve very accurately, provided that creep deformation is considered. This approach greatly simplifies the simulation process without the sacrifice of accuracy. However, questions are often raised on whether creep deformation needs to be included in the stress-strain relationship to mimic the deformation behaviour in such a short duration of less than 30 minutes in total.

To address this issue, some additional studies have been carried out, as presented in this chapter, to justify the need to include creep deformation in the FE model in order to reproduce the mechanical test results. This chapter will give details of the procedure for establishing the stress-strain relationship, including creep deformation, and discuss dependence of parameters in the corresponding constitutive equations on the specimen geometry and loading speed used in the mechanical testing.

3.2 Mechanical Testing and Simulation

The conventional approach to determining the stress-strain relationship is based on measurements from the mechanical testing. An example is the work by G'Sell et al. [32] in which displacements of selected points on specimen surface are measured to determine strain for a given stress level. However, during the necking process deformation on a cross section is highly non-uniform. Therefore, strain values measured from the surface do not reflect the strain in the core region. Instead, the approach adopted in our study is to establish the

stress-strain relationship through a combination of mechanical testing and FE modeling. Details of the approach are given below.

3.2.1 Mechanical Testing

Specimens used for the mechanical testing are prepared from HDPE plates of 10 mm thick, provided by NOVA Chemicals, of which molecular weight, molecular weight distribution, and density are given in Table 3-1. The plates were compression-molded by NOVA Chemicals from pellets to ensure isotropy of the mechanical properties. Cooling rate also kept constant by them to ensure same degree of crystallinity within each plate of HDPE. Both standard dog-bone specimens of rectangular cross section (ASTM D 638 type I) and nonstandard cylindrical specimens [33] were machined from those plates, with dimensions shown in Figures 3-1(a) and 3-1(b), respectively. To ensure that necking was always initiated at the middle of the gauge section where an extensometer was placed to monitor the change of the cross-sectional dimensions, a small imperfection was introduced there to reduce width and diameter of the dog-bone and cylindrical specimens, respectively, by less than 2%. Note that despite the

presence of such an imperfection, all specimens showed full neck development in the whole gauge section prior to the final fracture.

All tests were conducted using a universal testing machine (QUASAR 100). To ensure that the test results were reproducible, crosshead speed of 100 mm/min, same as that used previously [31], was used for testing the dog-bone specimens. This crosshead speed was chosen in the previous study to shorten the test duration, in order to minimize the creep strain involved during the test. However, heating induced at this crosshead speed may be significant enough to cause material softening. Therefore, another crosshead speed within the common speed range for plastics testing, 5 mm/min, was used for both dog-bone and cylindrical specimens. In view that each test at 5 mm/min took less than 30 minutes to complete, it was deemed unnecessary to consider another crosshead speed between 100 and 5 mm/min. On the other hand, the amount of creep deformation is expected to increase at a crosshead speed below 5 mm/min, thus increasing its significance in the deformation process. In view that the objective of the current study is to show that even within a short duration, the time-dependent deformation behaviour still plays an important role in the

mechanical testing, conducting tests below 5 mm/min is unnecessary if creep deformation needs to be considered at 5 mm/min.

It should be noted that stress-strain relationship determined from the dog-bone specimens at 5 mm/min are identical to that from the cylindrical specimens at the same crosshead speed. Therefore, whenever possible, results from the former are omitted in order to reduce the amount of data presented here.

3.2.2 FE Modeling

FE modeling was based on three-dimensional (3-D) dog-bone and two-dimensional (2-D) axisymmetric cylindrical models. The models were developed using ABAQUS Standard (version 6.7-1). The 3-D dog-bone model consisted of 4140 (C3D20R) 20-node quadratic brick elements, of totally 19583 nodes, and was used to determine the stress-strain relationship at two cross-head speeds, 100 and 5 mm/min. The 2-D cylindrical model, on the other hand, had 909 CAX8R axisymmetric 8-node elements, of totally 2918 nodes, and was used to determine the stress-strain relationship at the cross-head speed of 5 mm/min. Figures 3-2(a) and 3-2(b) give an example of the mesh pattern and typical necking

behavior generated in the dog-bone and cylindrical FE models, respectively. Note that due to the geometric symmetry, the dog-bone FE model was for half of the specimen length and quarter of the cross section.

Necking in the dog-bone FE model was introduced by tapering width in the gauge section so that the smallest width, with reduction about 0.07%, was located at the middle of the gauge section (i.e. at one end of the FE model). For the cylindrical FE model, on the other hand, the geometry was identical to the true specimen geometry used in the mechanical testing, without any artificial defect to encourage the neck formation.

Criteria used to evaluate the stress-strain relationship were based on the following information obtained from the mechanical testing.

(a) On the curve of engineering stress versus elongation: (i) peak stress and the corresponding elongation, (ii) curve profile during the initial necking process (i.e. during the load drop phase), and (iii) flow stress level during the neck propagation.

(b) On the curve of cross-sectional dimensions versus elongation: variation of the cross-sectional dimensions during the necking process, i.e. width and thickness of dog-bone specimens and diameter of cylindrical specimens.

When the FE models could mimic the above information from the mechanical testing, the stress-strain relationship was deemed to be successfully established.

Stress-strain relationship for the plastic deformation was based on J_2 flow theory. For the creep deformation a simple power law function was used to express the creep strain rate in terms of stress and time. Such an expression should be sufficient in view of the short duration involved in the mechanical testing. As shown by Eqn. 3.1 below, the stress-strain relationship was expressed using four equations for the elastic-plastic deformation and one for the creep deformation, with the creep deformation considered only for the strain range between ε_y and ε_t. Details of implementing the creep strain are given in section 3.3.3.

$$\sigma(\varepsilon)=\begin{cases}\dfrac{3}{2(1+\upsilon)}E\varepsilon & for\ \varepsilon\le\varepsilon_y & [15,19,34] & (a)\\ d\left[\{a(\varepsilon+b)\}^{(c-1)}-\{a(\varepsilon+b)\}^{(-c)}\right]+e & for\ \varepsilon_y\le\varepsilon\le\varepsilon_n & [35] & (b)\\ \alpha k\varepsilon^{N} & for\ \varepsilon_n\le\varepsilon\le\varepsilon_t & [36] & (c)\\ k\exp(M\varepsilon^{\beta}) & for\ \varepsilon\ge\varepsilon_t & [12,14] & (d)\\ \dot{\bar{\varepsilon}}^{cr}=A\sigma^{n}t^{m} & for\ \varepsilon_n\le\varepsilon\le\varepsilon_t & [37] & (e)\end{cases} \tag{3.1}$$

where σ is effective stress in MPa, ε the equivalent strain, ε_y the critical strain for the transition from linear to non-linear deformation, ε_n the strain for the on-set of necking, ε_t the transitional strain for the strain-hardening, $\dot{\bar{\varepsilon}}^{cr}$ the equivalent creep strain rate, t the time measured from the onset of necking, E Young's modulus, υ Poisson's ratio, and the rest of parameters (a, b, c, d, e, α, k, N, M, β, A, n, and m) user-defined constants.

Note that the above stress-strain relationship was implemented in the FE model using more than 2000 discrete points in a table format. Such a high density of discrete points allows minor adjustment to satisfy continuity in the stress-strain relationship between the adjacent strain ranges. Figure 3-3 presents the

stress-strain relationship used in this study. However, number of points in the figure has been dramatically reduced to improve the presentation clarity.

As mentioned earlier, values for parameters in Eqn. 3.1 were determined through iteration which was applied progressively in the current work through each strain range, while the iteration process in refs. [23, 28] was applied simultaneously to the entire strain range, i.e. from zero to the final necking strain. Therefore, the approach considered in this study has no more than 5 parameters for which values need to be determined through iteration.

3.3 Simulation Attempts for the Neck Development

Three typical FE simulation attempts (SA) are presented in this section, to illustrate the process that leads to the establishment of the stress-strain relationship for the necking in polymers. Typical relationship between

equivalent stress and equivalent strain is depicted in Figure 3-3(a) for the FE model of dog-bone specimen, and Figure 3-3(b) for the cylindrical specimen.

3.3.1 First simulation attempts (SA-1)

In the first simulation attempts (SA-1), an elastic-plastic stress-strain relationship was searched to mimic firstly the engineering stress-elongation curve (the first criterion in section 3.2.2). The input material property for the dog-bone specimen is depicted by the SA-1 curve in Figure 3-3(a) which unfortunately resulted in collapse of the FE model at an elongation around 40 mm, just slightly after the commencement of the neck propagation, as shown in Figure 3-4(a). Collapse of the FE model was due to an extremely small cross section in the necked section, as depicted by the change of cross sectional dimensions in Figure 3-4(b), a curve labeled SA-1, compared to the dimensions measured from the mechanical testing (labeled "Experiment"). Excessive reduction of the necked cross section was avoided by increasing the rate of strain hardening in the last stage of the neck forming process, i.e. by increasing M value in Eqn. 3.2(d). However, this also resulted in an increase of the flow stress level, thus not be able

to match the engineering stress-elongation curve obtained from the mechanical testing.

A similar trend of increasing M in Eqn. 3.2(d) to avoid the model collapse also resulted in an increase of the flow stress from the FE model of the cylindrical specimen. An example is given in Figure 3-5 for which the stress-strain relationship used for the FE model are presented by the curve labeled SA-1 in Figure 3-3(b). It should be noted that the SA-1 curve in Figure 3-3(b) is different from the corresponding one in Figure 3-3(a). The former has more significant strain hardening than the latter at the last stage of the neck formation. Although model collapse was avoided by the SA-1 curve in Figure 3-3(b), and the engineering stress-elongation curve from the FE model could match that from the mechanical testing, as depicted in Figure 3-5(b), such improvement in strain hardening could not mimic the change of the cross-sectional diameter observed from the mechanical testing, as depicted in Figure 3-5(b).

Many scenarios have been considered in the first attempts by firstly matching the engineering stress-elongation curve, but always resulted in a cross section which was smaller than that obtained from the mechanical testing. Therefore, it was

concluded that the change of the cross section as a function of elongation cannot be regenerated by the elastic-plastic FE model with the adjustment of strain hardening at the later stage of the necking process, even though the model could regenerate the engineering stress-elongation curve obtained from the mechanical testing.

3.3.2 Second simulation attempts (SA-2)

In view of the problems for matching both the cross section reduction and the flow stress level in all first simulation attempts, focus in the second simulation attempts was shifted to exploring the possibility of using elastic-plastic deformation, Eqns. 3.2(a)-3.2(d), to match the flow stress level determined from the mechanical testing. The final cross sectional dimensions of the neck, on the other hand, was controlled by introducing a sharp stress increase at a strain level that is equivalent to the strain level measured from a post-tested specimen with a

fully developed neck. The use of sharp stress increase is to stop further reduction of the cross section in the FE model.

With the final neck dimensions determined by setting the sharp stress increase at the final strain level for necking, values for parameters in Eqns. 3.2(a)-3.2(d) were selected in order for the FE model to regenerate the flow stress level. An example of the stress-strain relationship is shown by the SA-2 curves in Figures 3-3(a) and 3-3(b) for dog-bone and cylindrical specimens, respectively. Note that the SA-2 curves in Figure 3-3 are lower than the corresponding SA-1 curves, except the final portion where the sharp stress increase is. All attempts showed that even though the flow stress level from the mechanical testing could be regenerated by the FE model using the SA-2 curves in Figure 3-3, displacement for the on-set of neck propagation turned out to be much smaller than that measured from the mechanical testing, as shown in Figures 3-6 and 3-7 for dog-bone and cylindrical specimens, respectively. In each figure, for a given engineering stress or cross-sectional dimensions during the initial neck forming process, elongation from the FE model is much smaller than that from the mechanical testing. Further investigation indicated that this approach could not

generate a stress-strain relationship to enable the FE model to generate both engineering stress and cross sectional dimensions that match those from the mechanical testing during the load-drop phase. Had the stress-strain relationship allowed the SA-2 curves in Figures 3-6(a) and 3-7(a) move closer to the corresponding curves from the mechanical testing, labeled as "Experiment," the SA-2 curves in Figures 3-6(b) and 3-7(b) would have moved further away from the curves obtained from the mechanical testing.

Consistent results from many attempts, as described above, led to the conclusion that the FE model with the elastic-plastic deformation, i.e. Eqns. 3.2(a)–3.2(d), could not generate an engineering stress-elongation curve that had both the load-drop phase and the flow stress level match with those from the mechanical testing; while the rate of cross sectional reduction also matched with that measured from the mechanical testing.

3.3.3 Third simulation attempts (SA-3)

In view that based on elastic-plastic deformation, the above FE models could not regenerate results from the mechanical testing, specifically, variation of

engineering stress and cross section reduction as functions of elongation, approach adopted in the third simulation attempts (SA-3) was to introduce additional elongation, starting from the peak load, to match results from the mechanical testing. The approach is illustrated schematically in Figure 3-8. Since HDPE has a glass transition temperature of more than 50 K below the room temperature [38], creep is expected to occur at room temperature under tensile loading, especially when subjected to a high level of stress. The FE models, however, only considered the creep deformation during the initial neck forming stage, i.e. during the load-drop phase in the strain range for Eqns. 3.2(b) and 3.2(c). This was considered to be reasonable because at the initial loading stage, for Eqn. 3.2(a), time involved was so short that creep deformation could be ignored, and at the later stage of the neck development, for Eqn. 3.2(d), polymer molecules should have been stretched to be more or less aligned in the loading direction [39], thus allowing very little creep to occur. Although a significant amount of creep might still occur during the neck propagation stage, i.e., in sections away from the fully developed neck, such creep deformation does not affect the flow stress level or cross sectional dimensions of the neck that were used to verify the stress-strain relationship.

It should be noted that due to the deformation-induced chain reorientation, the necking process should have significantly increased the creep resistance of HDPE, especially at the later stage of neck development before the final neck dimensions were reached. However, the increase in creep resistance during the necking process was not considered in this study. Instead, parameters A, n and m in Eqn. 2(e) were assumed to have constant values. This assumption, however, could not generate sufficiently fast strain hardening rate to reflect the deformation behaviour observed in the mechanical testing. Instead, four sets of parameters were found to be the minimum required number of sets for Eqn. 3.2(d) to capture the fast increase of strain hardening at this stage of the necking process.

As mentioned in section 3.2 (Mechanical Testing and Simulation), values for parameter in Eqn. 3.2 were determined using a piecewise curve fitting technique. That is, the curve fitting was first applied progressively to each of the strain range for Eqn. 3.2(a)-3.2(d). Since number of the unknown parameters in each strain range is no more than 5, the task of determining values for those parameters is quite manageable, in spite of the large number of unknown parameters. Note that for the strain range from ε_y to ε_t, i.e., for Eqns. 3.2(b) and 3.2(c), values for

the unknown parameters were first determined without the consideration of creep. Then, those values were adjusted to take into account the creep involvement, Eqn. 3.2(e), through iteration to meet the criteria set in section 3.2.2.

The final stress-strain relationships determined in SA-3 are presented in Figures 3-3(a) and 3-3(b), for dog-bone and cylindrical specimens, respectively. Tables 3-2 and 3-3 present the corresponding parameter values and the strain ranges, respectively, and Figure 3-9 the comparison between FE models and mechanical testing for the engineering stress and cross sectional dimensions as functions of elongation. Figure 3-9 suggests that all criteria specified in section 3.2.2 are satisfactorily met.

As shown in Table 3-2, one set of values for parameters in Eqn. 3.1(d) could not generate sufficient strain hardening to mimic the behaviour observed from the mechanical testing. Instead, four sets of k and M values were used for Eqn. 3.2(d), with β being fixed at 1.8 (following that used in ref. [23]), in order to capture the fast strain hardening rate at this stage. Note that no creep needed to be considered at this stage.

3.4 Discussion

Similar to other constitutive equations that have been proposed for large deformation and necking in polymers, e.g. ref. [4-5, 8, 40], Eqn. 3.2 contains many parameters of which thirteen (except υ and β) require results from the mechanical testing to determine their values. As mentioned earlier, because of the use of piecewise strain range in the iteration process, no more than five parameters need to be considered each time. Therefore, the procedure to establish the stress-strain relationship is relatively easy to execute.

The use of Eqn. 3.2 to determine the stress-strain relationship allows the separation of elastic-plastic deformation from the creep deformation, which would have been difficult if the study had been purely based on the experimental measurement. Creep occurs in polymers due to their nature of time-dependent deformation which is sometimes regarded as the major source for their strain-rate dependency. However, change in elastic-plastic strain rate may also affect the material response to the load. In fact, change of elastic-plastic strain rate is well known to affect deformation and fracture behaviour of metals that rarely show any time-dependent behavior [41-43], especially in a short timeframe such as that

used in the current study. For most studies on polymers, however, this type of investigation has been difficult because creep is usually involved in the deformation and little is known about how to separate the creep deformation from the elastic-plastic counterpart at the post-yield stage when necking is involved. We believe that through Eqn. 3.2, creep deformation can be readily separated from the elastic-plastic deformation, enabling us to separate strain rate sensitivity of polymers due to elastic-plastic strain from that due to time-dependent strain. As indicated by values in Table 3-2, for a timeframe of less than 30 minutes that is commonly used for the mechanical testing, change of the crosshead speed from 5 to 100 mm/min does not seem to affect the time-dependent deformation process governed by Eqn. 3.2(e), though this part of deformation is essential to simulate correctly the necking process in an FE model.

Values in Table 3-2 also suggest that change of the specimen geometry from dog-bone to cylindrical shape has little effect on the stress-strain relationship, and that increase of the crosshead speed from 5 to 100 mm/min affects mainly the stress-strain relationship governed by Eqns. 3.2(a)-3.2(d).

3.5 Conclusions

An approach is presented to use macro deformation behavior of polymers to establish the stress-strain relationship. The approach has been successfully applied to HDPE specimens of two different geometries at cross-head speeds of 5 and 100 mm/min. Stress-strain relationship determined using this approach allows the use of FE simulation to mimic closely the mechanical behavior of polymers during the necking process. The results also suggest that creep deformation needs to be considered in order to regenerate the mechanical behavior observed from the mechanical testing.

As the creep deformation is expressed separately from the elastic-plastic counterpart in Eqn. 3.2, the creep-related strain can be excluded from the total strain in order to evaluate the effect of the strain rate on the elastic-plastic deformation of polymers.

Figures:

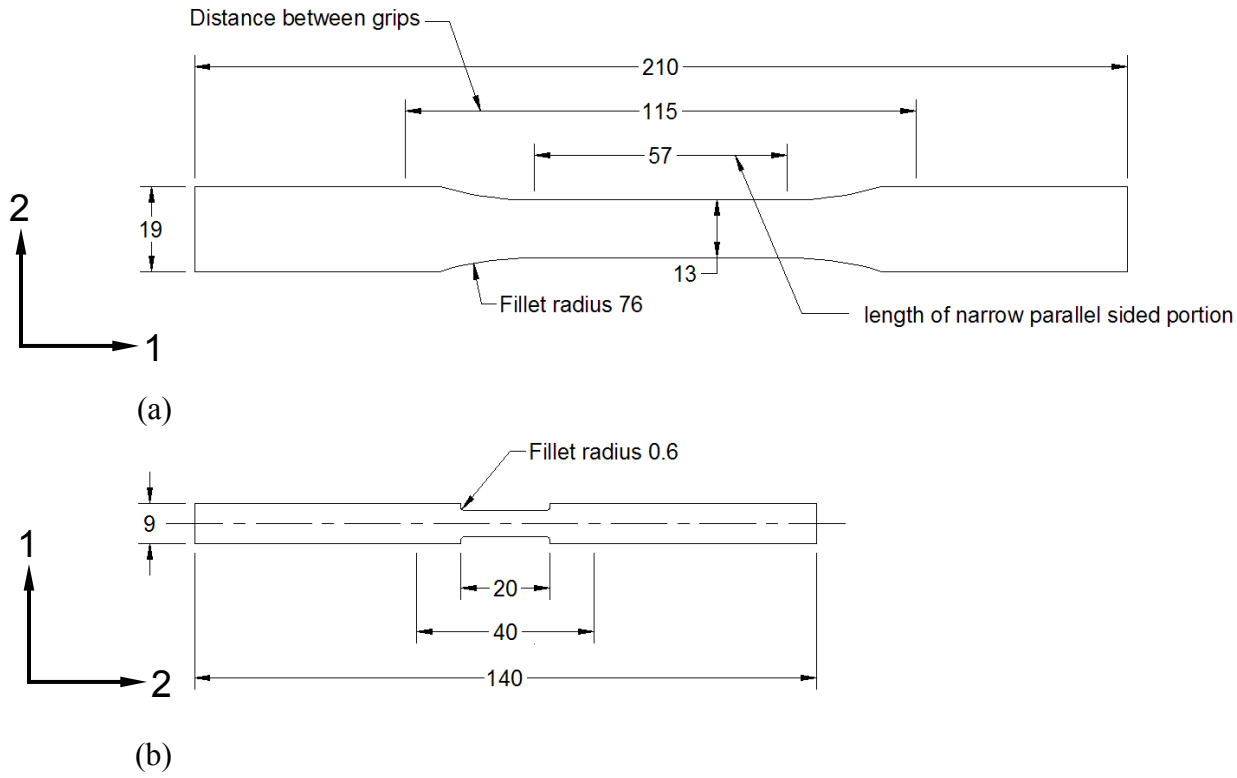

Figure 3-1 (a) Dimensions of the dog-bone specimen according to ASTM D638 (Type I) with coordinates 1 and 2 representing direction in length and width, respectively (specimens thickness = 10 mm), and (b) dimensions of the cylindrical specimens with coordinates 1 and 2 representing direction in radius and length, respectively.

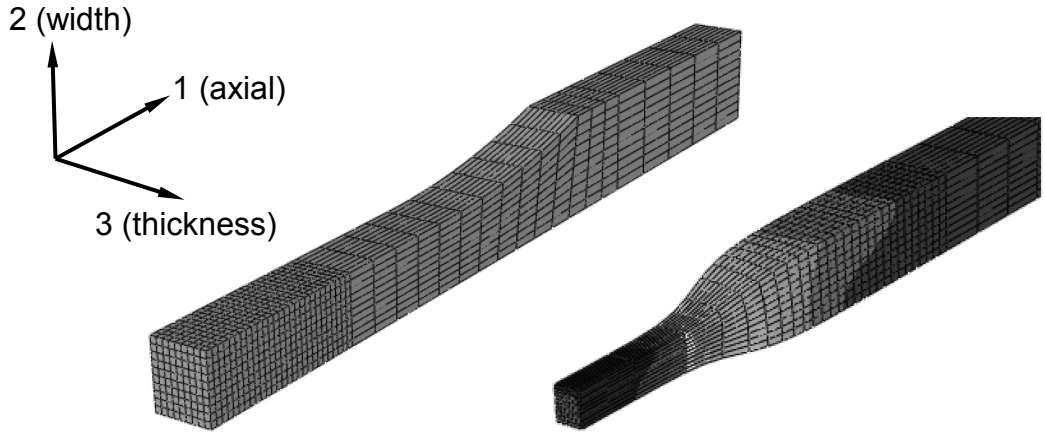

(a)

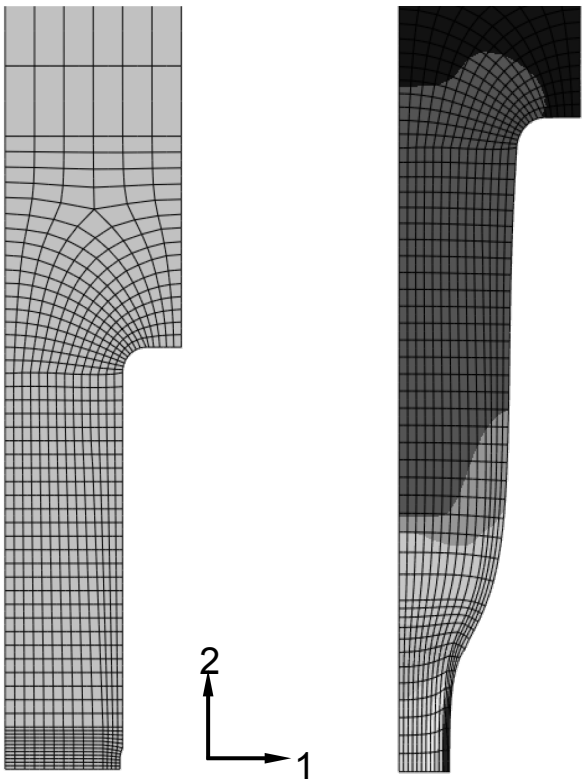

(b)

Figure 3-2 The FE models and examples of neck formation: (a) 3-D dog-bone model with coordinates 1, 2, and 3 representing axial, width, and thickness directions, respectively, and (b) axisymmetric cylindrical model with coordinates 1 and 2 representing radial and axial directions, respectively.

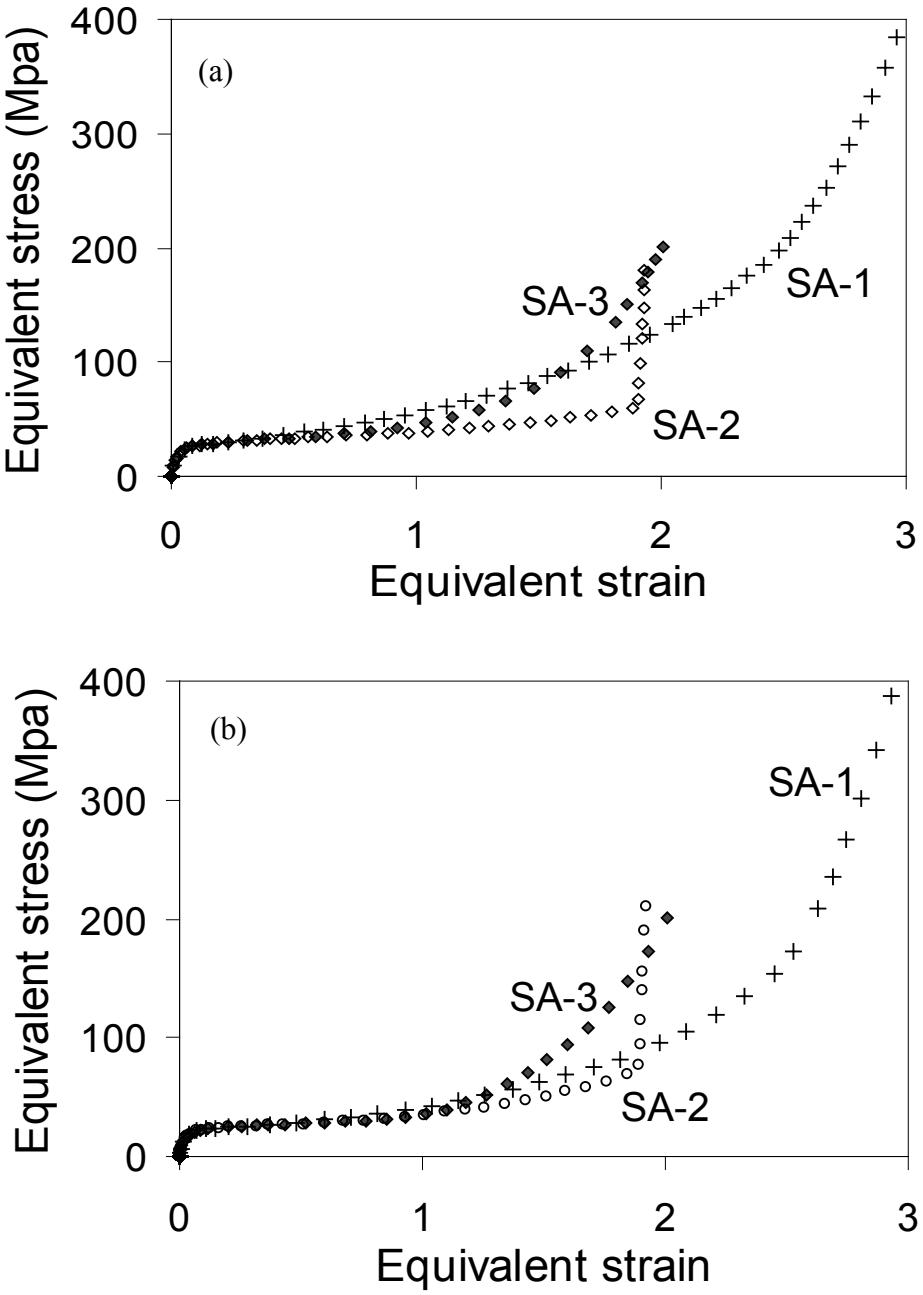

Figure 3-3 Curves of equivalent stress versus equivalent strain, for various simulation attempts: (a) for 3-D dog-bone model, and (b) for 2-D axisymmetric cylindrical model.

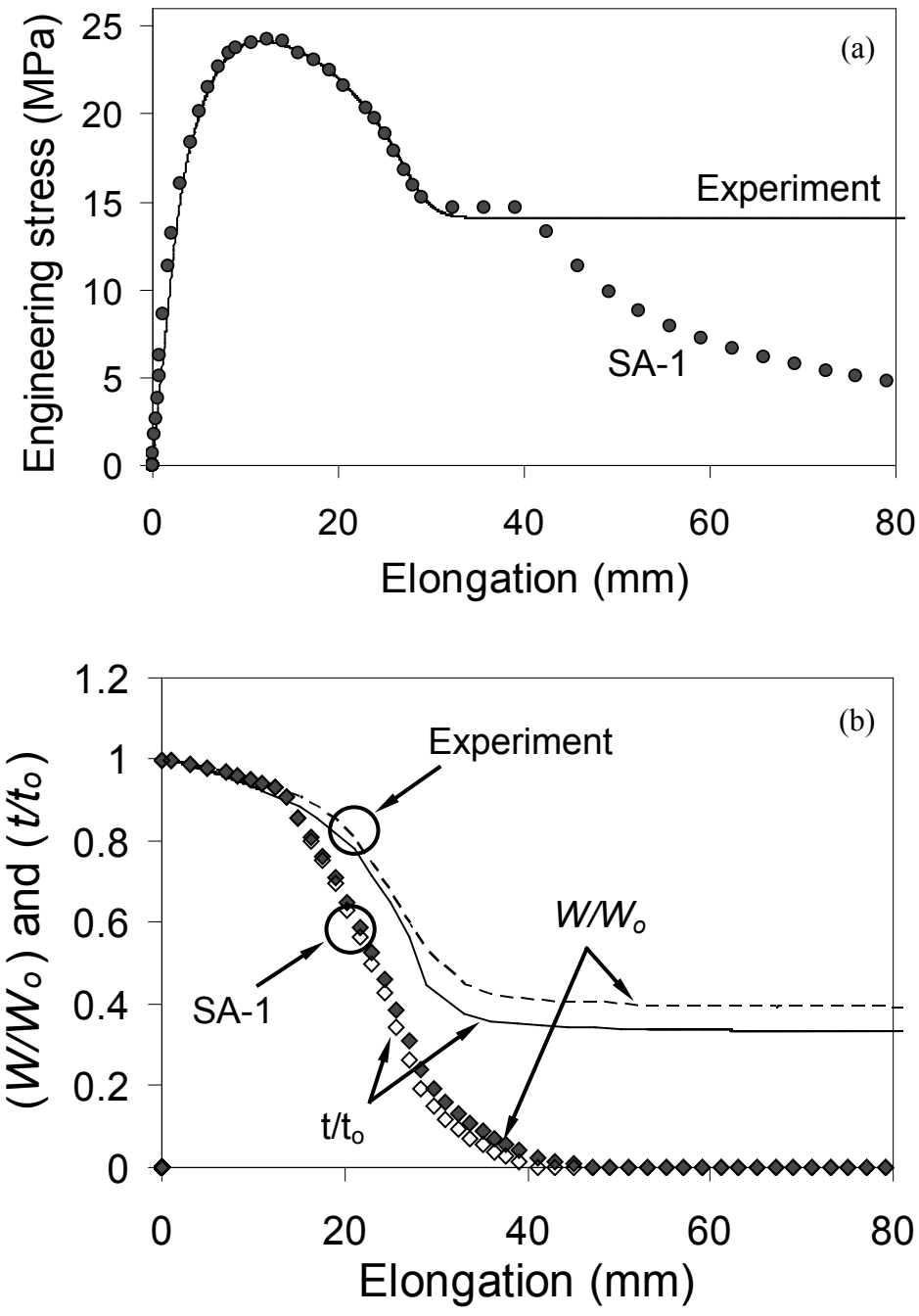

Figure 3-4 Comparison between mechanical testing (Experiment) and FE simulation (SA-1) for dog-bone specimens: (a) engineering stress and (b) normalized width (W/W_o) and thickness (t/t_o), as a function of elongation.

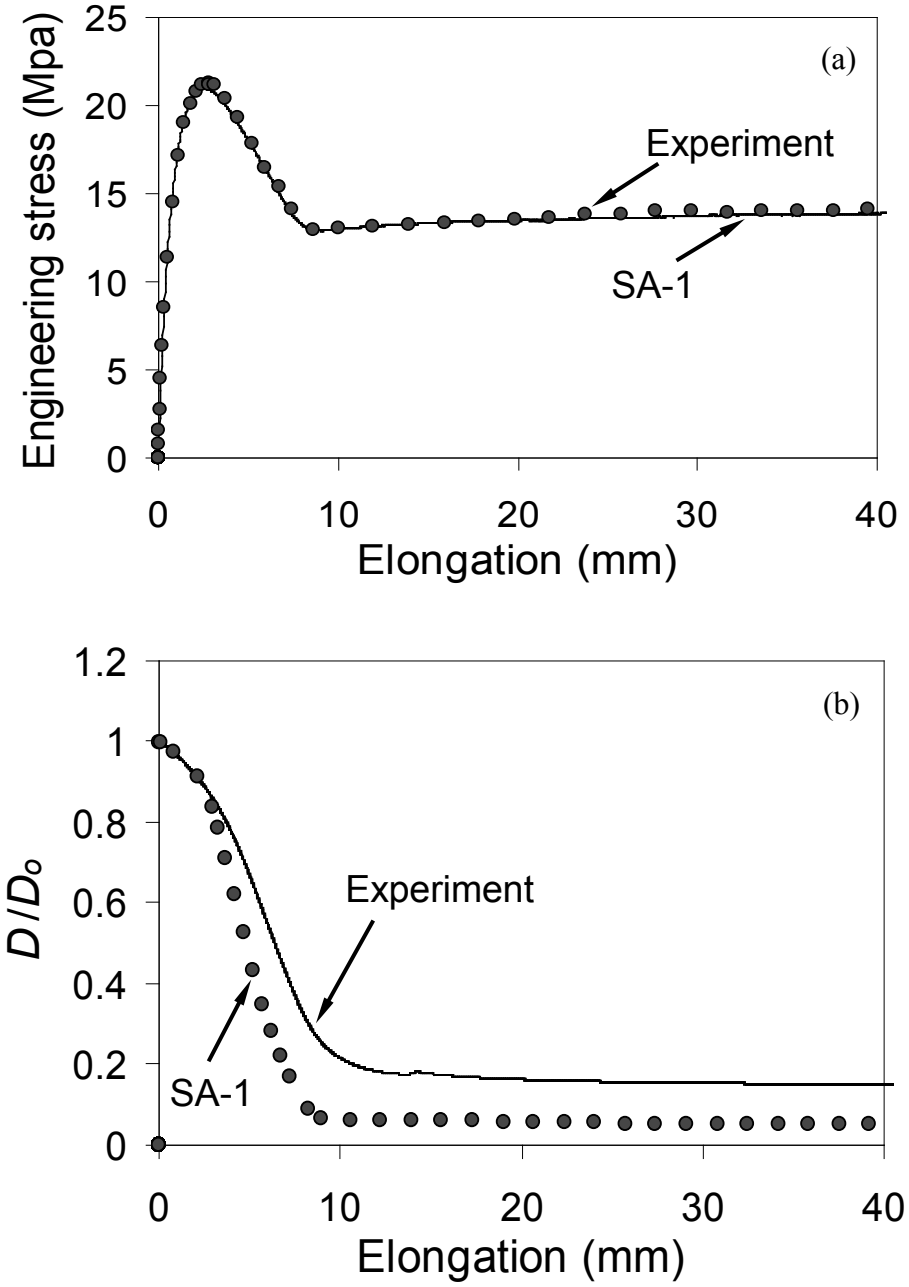

Figure 3-5 Comparison between mechanical testing (Experiment) and FE simulation (SA-1) for cylindrical specimen: (a) engineering stress and (b) normalized diameter (D/D_o), as a function of elongation.

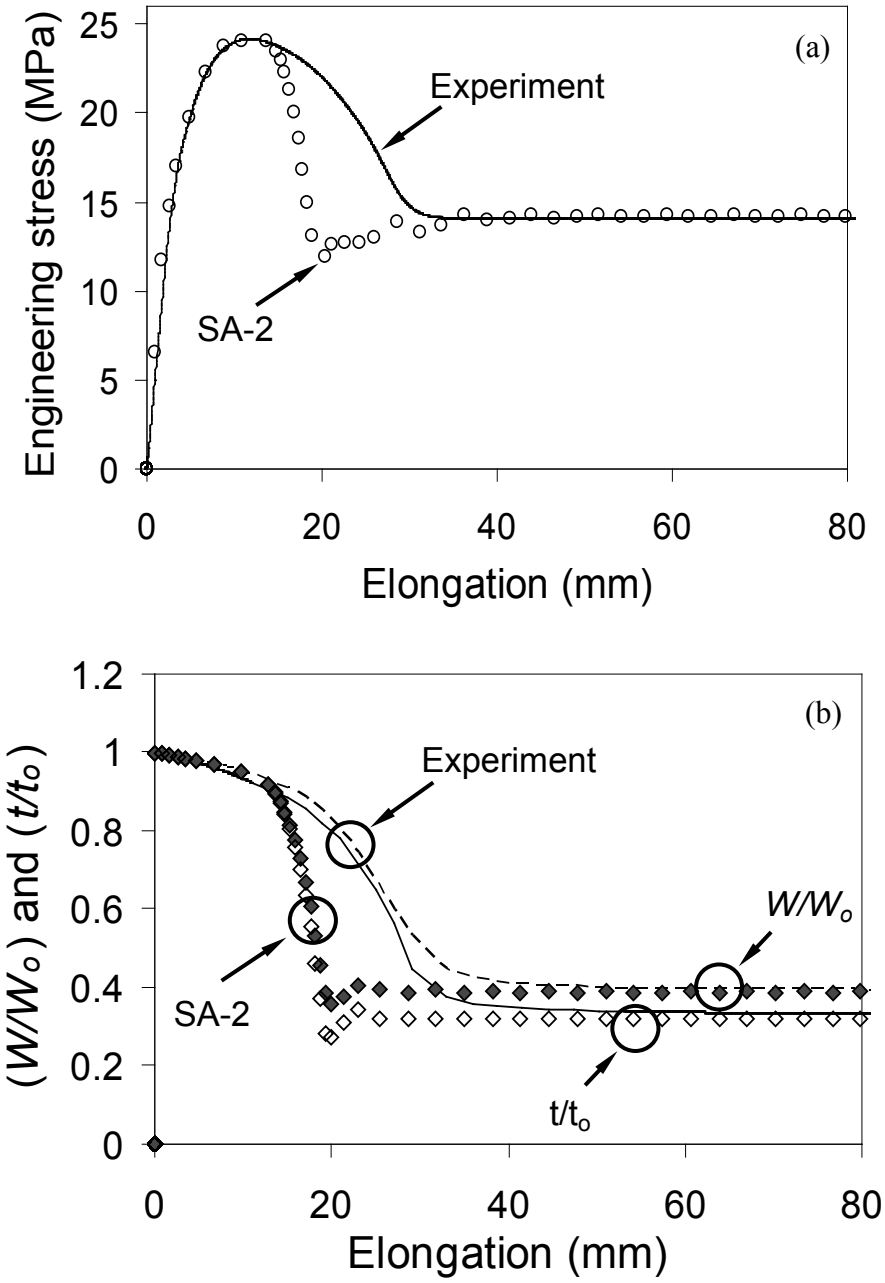

Figure 3-6 Comparison between mechanical testing (Experiment) and FE simulation (SA-2) for dog-bone specimen: (a) engineering stress and (b) normalized width (W/W_o) and thickness (t/t_o), as a function of elongation.

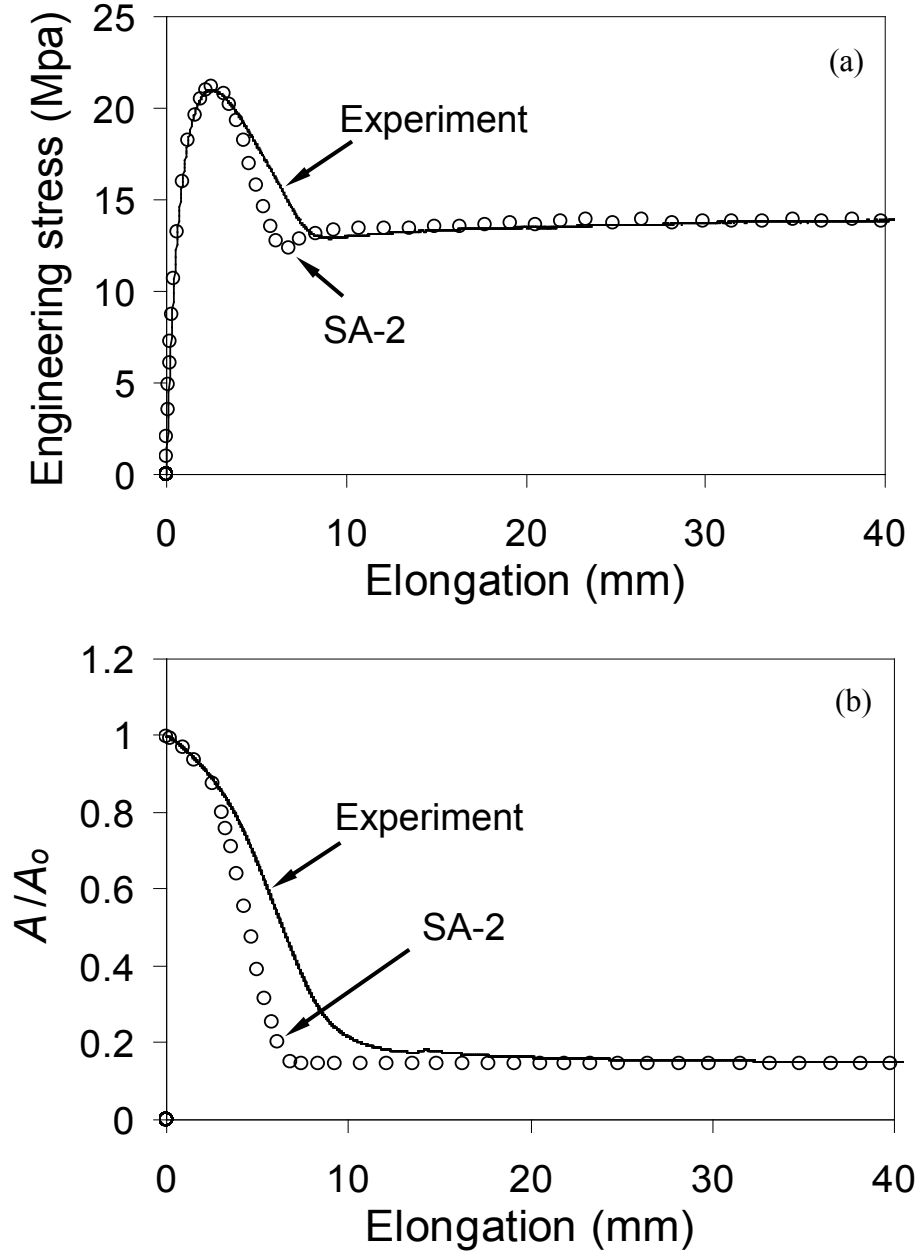

Figure 3-7 Comparison between mechanical testing (Experiment) and FE simulation (SA-2) for cylindrical specimens: (a) engineering stress and (b) normalized diameter (D/D_o), as a function of elongation.

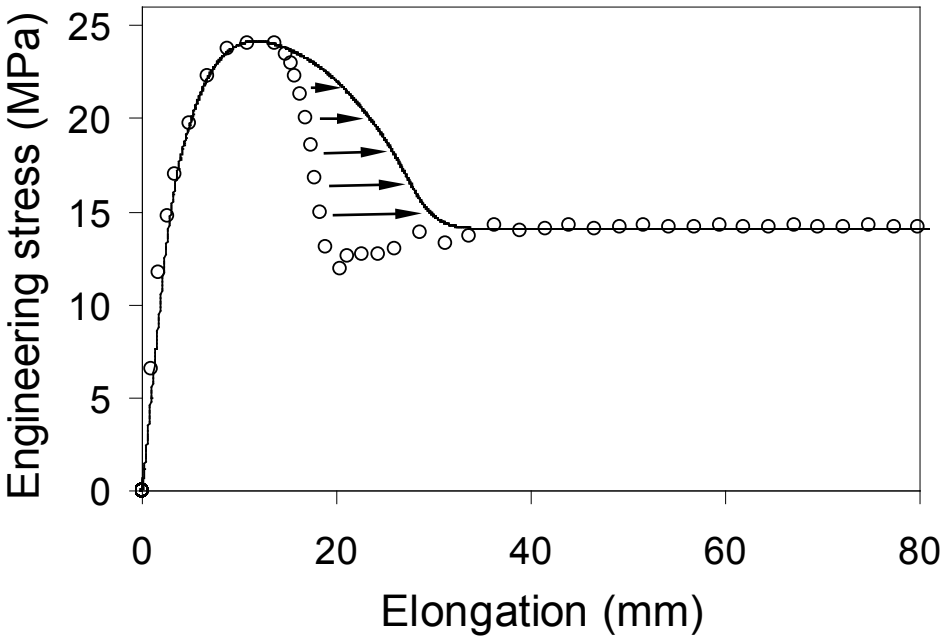

Figure 3-8 Illustration of the approach adopted in the third simulation attempts (SA-3), to bring the simulation results close to those from the mechanical testing.

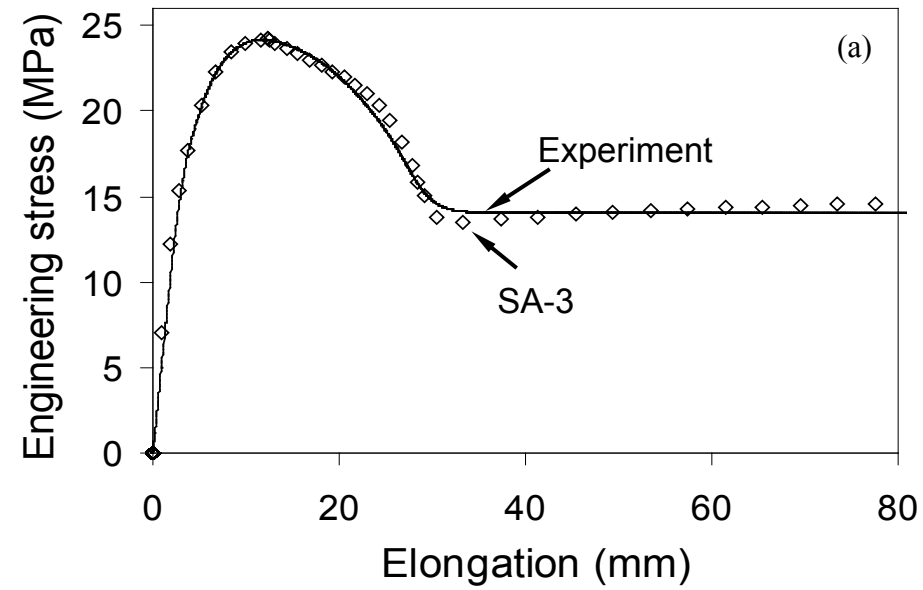
(a)
Engineering stress (MPa)
25
20
15
10
5
0
Experiment
SA-3
0
20
40
60
80
Elongation (mm)

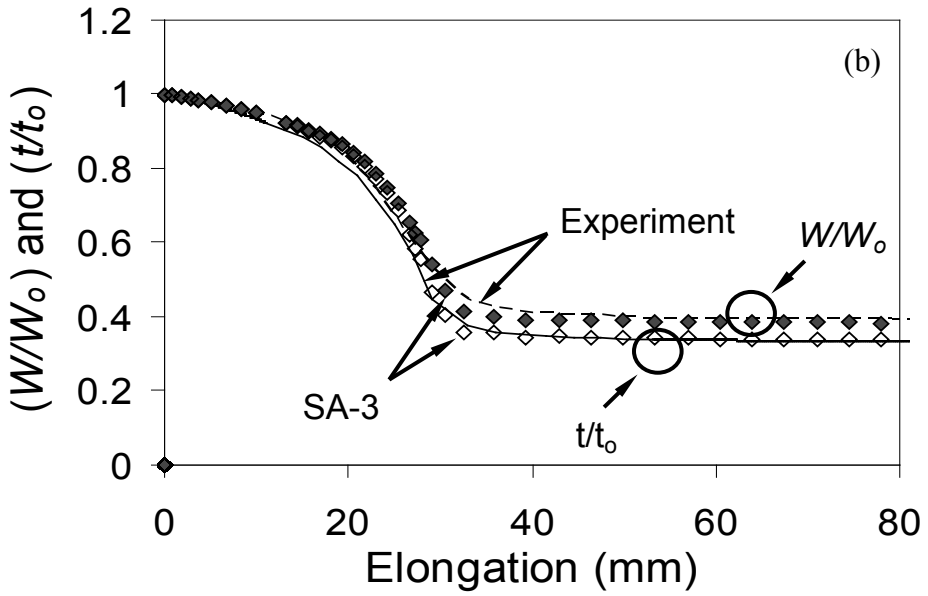
(b)
(W/W_o) and (t/t_o)
1.2
1
0.8
0.6
0.4
0.2
0
Experiment
W/W_o
SA-3
t/t_o
0
20
40
60
80
Elongation (mm)

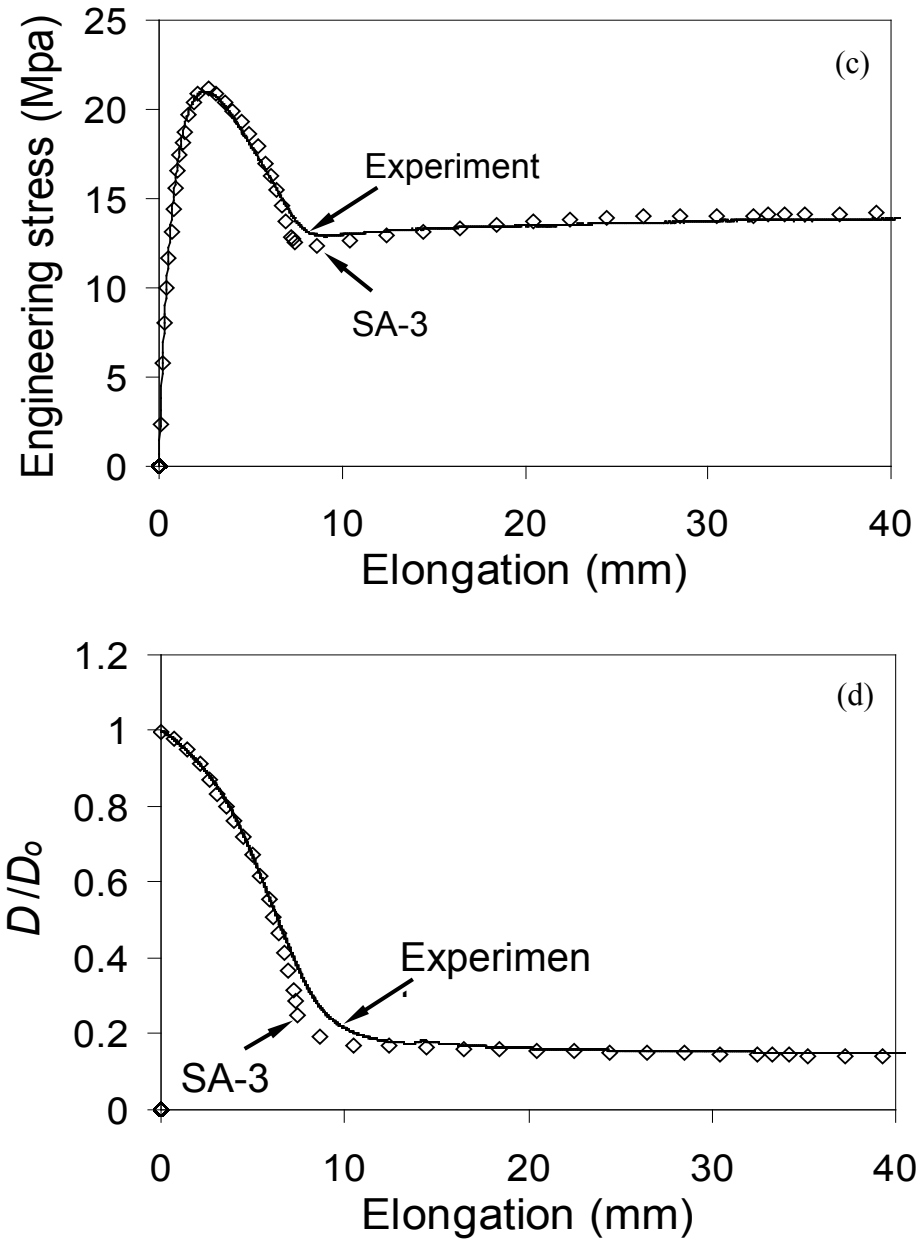

Figure 3-9 Comparison between mechanical testing (Experiment) and FE simulation (SA-3): (a) engineering stress versus elongation for dog-bone specimens, (b) normalized width (W/W_o) and thickness (t/t_o) versus elongation for dog-bone specimens, (c) engineering stress versus elongation for cylindrical specimens, and (d) normalized diameter (D/D_o) versus elongation for cylindrical specimens.

Tables:

Table 3-1 Material characteristics of HDPE (hexane copolymer) used in this study.

Weight-average molecular weight (M_w) (g/mol)	Number-average molecular weight (M_n) (g/mol)	Z-average molecular weight (M_z) (g/mol)	Density, ρ (g/cm^{-3})	M_w/M_n
182000	17000	935000	0.945	10.6

Table 3-2 Values for parameters in Eqn. 3.1.

FE Model				3-D dog-bone		Axis-symmetric cylindrical
Crosshead speed (mm/min)				100	5	5
Parameters for Eqn. 3.2	Linear elastic (Eqn. 3.2(a))		E	800	950	950
			v	0.35	0.35	0.35
	Non-linear deformation (Eqn. 3.2(b))		a	30	27	27
			b	0.02	0.02	0.02
			c	0.01	0.18	0.18
			d	-19	-21	-21
			e	14	13	14
	Hollomon's equation for plastic deformation (Eqn. 3.2(c))		αk	37	32	30
			N	0.14	0.16	0.11
	Work hardening deformation (Eqn. 3.2(d))	Section 1	k	30.2	25. 5	25.1
			M	0.40	0.38	0.31
			β	1.8	1.8	1.8
		Section 2	k	27.2	22.5	21.1
			M	0.50	0.56	0.53
			β	1.8	1.8	1.8
		Section 3	k	23.9	19.0	15.6
			M	0.58	0.70	0.79
			β	1.8	1.8	1.8
		Section 4	k	19.3	22.7	20.7
			M	0.67	0.61	0.65
			β	1.8	1.8	1.8
	Visco-plastic deformation (Eqn. 3.2(e))		$A\times10^{8}$	1.75	1.75	1.75
			n	4.5	4.5	4.5
			m	-0.61	-0.61	-0.61

Table 3-3 Strain ranges in different parts of Eqn. 3.1.

FE Model			3-D dog-bone		Axis-symmetric cylindrical
Cross-head speed (mm/min)			100	5	5
Parameters for Eqn. 3.2	Linear elastic (Eqn. 3.2(a))		0-0.012	0-0.005	0.00-0.005
	Non-linear deformation (Eqn. 3.2(b))		0.013-0.078	0.005-0.10	0.005-0.10
	Hollomon equation (Eqn. 3.2(c))		0.078-0.41	0.10-0.40	0.11-0.40
	Work hardening deformation (Eqn. 3.2(d))	Section 1	0.41-1.03	0.41-0.81	0.41-0.87
		Section 2	1.03-1.34	0.81-1.11	0.87-1.09
		Section 3	1.34-1.59	1.12-1.46	1.09-1.47
		Section 4	1.59-1.99	1.47-1.90	1.48-1.99
	Visco-plastic deformation (Eqn. 3.2(e))		0.13-1.12	0.145-1.00	0.15-0.95

References

[1] P. G. Higgs, R. J. Gaylord, Slip-links, hoops and tubes: tests of entanglement models of rubber elasticity, Polymer 31 (1990) 70-74.

[2] S. F. Edwards, Th. Vilgis, The effect of entanglements in rubber elasticity, Polymer 27 (1986) 483-492.

[3] M. G. Brereton, P. G. Klein, Analysis of the rubber elasticity of polyethylene networks based on the slip link model of S. F. Edwards et al., Polymer 29 (1988) 970-974.

[4] M.C. Boyce, D.M. Parks, A.S. Argon, Large inelastic deformation of polymers, Part I: Rate dependent constitutive model, Mech. Mater. 7(1) (1988) 15-33.

[5] M.C. Boyce, G.G. Weber, D.M. Parks, On the kinematics of finite strain plasticity, J. Mech. Phys. of Solids 37(5) (1989) 647-65.

[6] P.D. Wu, E. van der Giessen, On improved 3-D non-Gaussian network models for rubber elasticity, Mech. Res. Commun. 19(5) (1992) 427-37.

[7] P.D. Wu, E. van der Giessen, On improved network models for rubber elasticity and their applications to orientation hardening in glassy polymers, J. Mech. Phys. Solids 41(3) (1993) 427-56.

[8] J.J. Wu, C.P. Buckley, Plastic deformation of glassy polystyrene: A unified model of yield and the role of chain length, J. Polym. Sci. B 42(11) (2004) 2027-40.

[9] A.D. Drozdov, J. Christiansen, Nonlinear time-dependent response of isotactic polypropylene, J. Rheol. 47(3) (2003) 595-618.

[10] P.D. Wu, E. van der Giessen, On neck propagation in amorphous glassy polymers under plane strain tension, Int. J. Plast. 11 (1995) 211-35.

[11] Q.Z. Fang, T.J. Wang, H.G. Beom, H.P. Zhao, Rate-dependent large deformation behavior of PC/ABS, Polymer 50 (2009) 296-304.

[12] C. G'Sell, J.J. Jonas, Determination of the plastic behavior of solid polymers at constant true strain rate, J. Mater. Sci. 14 (1979) 583-91.

[13] B.D. Coleman, Necking and drawing in polymeric fibers under tension, Arch. Rat. Mech. Analy. 83(2) (1983) 115-37.

[14] J.W. Hutchinson, K.W. Neale, Neck propagation. J. Mech. Phys. Solids 31(5) (1983) 405-26.

[15] K.W. Neale, P. Tugcu, Analysis of necking and neck propagation in polymeric materials, J. Mech. Phys. Solids 33 (1985) 323-37.

[16] Y. Tomita, T. Takahashi, A. Shindo, Neck and bulge propagation in polymeric cylinders under internal pressure, Int. J. Mech. Sci. 32(4) (1990) 335-43.

[17] L.O. Fager, J.L. Bassani, Plane strain neck propagation, Int. J. Solids Struct. 22 (1986) 1243-57.

[18] P. Tugcu, K.W. Neale. Necking and neck propagation in polymeric materials under plane-strain tension. Int. J. Solids Struct. 23(7) (1987a) 1063-85.

[19] P. Tugcu, K.W. Neale, Analysis of plane-strain neck propagation in viscoplastic polymeric films, Int. J. Mech. Sci. 29(12) (1987) 793-805.

[20] P. Tugcu, K.W. Neale, Analysis of neck propagation in polymeric fibres including the effects of viscoplasticity, Trans. ASME, J. Engng. Mater. Tech. 110(4) (1988) 395-400.

[21] Y. Duan, A. Saigal, R. Greif, N.A. Zimmerman, A uniform phenomenological constitutive model for glassy and semicrystalline polymers, Polym. Eng. Sci. 41(8) (2001) 1322-28.

[22] A. Masud, A 3-D model of cold drawing in engineering thermoplastics. Mech. Adv. Mater. Struct. 12 (2005) 457-69.

[23] H.J. Kwon, P.-Y.B. Jar, On the application of FEM to deformation of high-density polyethylene, Int. J. Solids Struct. 45(2008) 3521-43.

[24] A. Muliana, K. R. Rajagopal, Modeling the response of nonlinear viscoelastic biodegradable polymeric stents, Int. J. Solids and Structures 49 (2012) 989–1000.

[25] G.D. Dean, L.N. McCartney, R. Mera, J.M. Urquhart, Modeling nonlinear viscoelasticity in polymers for design using finite element analysis, Polym. Eng. Sci. 51 (2011) 2210-2219.

[26] S.G. Bardenhagen, M.G. Stout, G.T. Gray, Three-dimensional, finite deformation, viscoplastic constitutive models for polymeric materials, Mech. Mater 25(4) (1997) 235-53.

[27] F. Zaïri, M. Naït-Abdelaziz, K. Woznica, J.-M. Gloaguen, Constitutive equations for the viscoplastic-damage behaviour of a rubber-modified polymer, Eur. J. Mech. A/Solids 24(1) (2005) 169-82.

[28] Y. Tomita, K. Hayashi, Thermo-elasto-viscoplastic deformation of polymeric bars under tension, Int. J. Solids Struct. 30 (1993) 225-35.

[29] F. Khan, C. Yeakle, Experimental investigation and modeling of non-monotonic creep behavior in polymers, Int. J. Plasticity 27 (2011) 512–521.

[30] D. A. Serban, L. Marsavina, V. V. Silberschmidt, Response of semi-crystalline thermoplastic polymers to dynamic loading: A finite element study, Comp. Mat. Sci. 64 (2012) 116–121.

[31] S. Muhammad, P.-Y.B. Jar, Effect of aspect ratio on large deformation and necking of polyethylene, J. Mater. Sci. 46 (2010) 1110-23.

[32] C. G'Sell, J.M. Hiver, A. Dahoun, Experimental characterization of deformation damage in solid polymers under tension, and its interrelation with necking, Int. J. Solids Struct. 39(13-14) (2002) 3857-72.

[33] P.-Y.B. Jar, S. Muhammad, Cavitation-induced rupture in high-density polyethylene copolymers, Polym. Eng. Sci. 52(5) (2012) 1005-1014 .

[34] K.W. Neale, P. Tugcu, Approximate methods for analyzing the cold drawing of polymeric fibres and films, Int. J. Numer. Methods Eng. 25 (1988) 99-112.

[35] R.W. Ogden, Large deformation isotropic elasticity: on the correlation of theory and experimental for compressible rubberlike solids, Proc. R. Soc. Lond., Ser. A, Math. Phys. Eng. Sci. 328 (1972) 567-83.

[36] J.H. Hollomon, Tensile deformation, Trans. Metall. Soc. American Institute of Mining and Metallurgical Engineers (AIMME) 162 (1945) 268-290.

[37] "Rate-dependent plasticity: creep and swelling", Section 18.2.4, ABAQUS Analysis User's Manual version 6.7 (2007) ABAQUS, Inc.

[38] D.W. van Krevelen, Properties of Polymers, third ed., Elsevier, Amsterdam, 1997.

[39] A. Peterlin, Drawing and extrusion of semi-crystalline polymers, Colloid Polym. Sci. 265 (1987) 357-382.

[40] H.X. Li, C.P. Buckley, Evolution of strain localization in glassy polymers: A numerical study. Int. J. Solids Structures 46 (2009) 1607-1623.

[41] J. Klepaczko, Thermally activated flow and strain rate history effects for some polycrystalline FCC metals, Mater. Sci. Eng. 18 (1975) 121-135.

[42] K.G. Hoge, A.K. Mukherjee, The temperature and strain rate dependence of the flow stress of tantalum, J. Mater. Sci. 12 (1977) 1666-1672.

[43] R.W. Armstrong, S.M. Walley, High strain rate properties of metals and alloys. Int. Mater. Rev. 53(3) (2008) 105-128.

CHAPTER - 4

Variation of Strain Rate during the Necking Process of High-Density Polyethylene

4.1 Introduction and Background

It is undeniable that in recent years, polymers and polymer based composites are key materials to replace metals for engineering and structural applications in many fast growing areas. As listed by the Society of Automotive Engineering World [1], advanced composites and polymers are expected to be the most favorable materials for engineering design in the next ten years, in contrast to

aluminum and steel which are placed at fourth and sixth, respectively. Among polymers of interest, high-density polyethylene (HDPE) is of utmost importance because of its capability in generating stable necking before fracture. Because of the potential of HDPE in engineering applications, comprehensive understanding of its deformation behavior has become a necessity. Challenge of the task, however, is aggravated by the involvement of visco-plastic strain in the deformation process.

Like many polymers and polymer-based composites [2-10], yield stress of HDPE shows a significant dependence on the strain rate. One study [3] shows the effect of strain rate and temperature on yield stress and morphology of semi-crystalline polymers. For example, the yield stress follows a logarithmic function of strain rate, which could be fit using Eyring's equation [11-12]. A similar trend [13] has also been reported for polypropylene and its nano-composites.

Most of the experimental studies on the strain rate effect rely on simple tensile loading to generate the deformation. For polymers that involve necking in tensile deformation, strain rate could vary significantly during the necking process [14]. Since variation in the strain rate could affect mechanical response of polymers,

quantifying the strain rate variation is an essential step to establish the correct constitutive equations for large deformation. Preferably, the constitutive equation could distinguish explicitly the time-dependent part from the time-independent part.

To our knowledge, only several groups have distinguished the two parts of deformation behaviors. Early work was done by Boyce and Arruda [15] who exploited the feasibility of using a 3-D constitutive model to simulate the necking behavior in glassy polymers. Li and Buckley [16-17] employed a glass-rubber constitutive model at the molecular level to simulate non-linear elastic-visco-plastic deformation in the necking process. Their results show a significant effect of strain rate on the necking behavior. However, Wu and van der Giessen [18] found that necking in a glassy polymer was insensitive to the strain rate. It has also been demonstrated by Kwon and Jar [19] that it is feasible to use only macroscopic behavior, through mimicking both load-displacement curve and cross-sectional reduction during the necking process, to establish the constitutive equation for large deformation. A follow-up study [20] successfully simulated

large deformation and necking in tensile specimens of HDPE with different cross-sectional aspect ratios.

This paper is based on the same approach as that used by Muhammad and Jar [20], to establish the constitutive equations for HDPEs at two different crosshead speeds. The constitutive equations are then implemented in finite element (FE) models to exclude the creep strain component so that the strain for elastic-plastic deformation can be extracted, to be directly correlated with the stress change during the necking process. Strain rates for the elastic-plastic deformation are then determined, and compared with the strain rates determined using total strain that includes the creep deformation.

4.2 Rationale and Objectives

Strain-rate-dependent deformation behaviour has been studied extensively in the past, not only for polymers but also for metals and their alloys. Many studies on metals [21-23] have identified an apparent mismatch of deformation and fracture behavior when the strain rate changes, and attributed the mismatch to the change

of the strain rate. The study of strain rate effect on polymers such as HDPE has additional challenges, due to the involvement of creep deformation that can be significant in the necking process. Since change in creep strain does not necessarily cause stress change, having it included in the calculation of strain rate may cause ambiguity about the effect of strain rate on the stress response to the deformation.

To our knowledge, most studies on polymers do not exclude creep strain from the calculation of the strain rate. We believe that this is partly due to little knowledge about how to separate the creep strain from the elastic-plastic strain, especially at the post-yield stage when necking is involved. In some cases, strain rate determined based on the total strain is even regarded as a synonym of the loading rate, which is varied by changing the crosshead speed used for the test [2-3, 9-10]. This type of analysis, however, leads to uncertainty in predicting the polymer deformation when the change of strain rate occurs at a time scale that is different from the time scale used to establish the database.

In view of the above problem, a study is conducted to determine the amount of creep strain generated in HDPE during the necking process. The strain rate for

elastic-plastic deformation is then calculated after removing the creep strain from the total strain. Variation of the strain rate for the elastic-plastic deformation during the necking process is then compared with that calculated based on the total strain which includes the creep strain, to assess any difference between the two ways for determining the strain rate.

4.3 Methodology

4.3.1 Experimental

Materials, specimen preparation and testing conditions used in this study followed closely to those used previously [20]. Results for the crosshead speed of 100 mm/min were based on the same experimental data reported in ref. [20]. Material designation (PE1 and PE2) used here are also identical to those used in ref. [20]. Additional tests were conducted at 5 mm/min, to determine the strain rate variation during the necking process at the crosshead speed of 5 mm/min.

Note that as mentioned in ref. [20], aspect ratio of the cross section (width to thickness) of the specimens was varied by changing the specimen thickness (3 and

10 mm) while keeping the width fixed (13 mm), resulting in change of the aspect ratio from 4.3 (for 3-mm thick) to 1.3 (for 10-mm thick).

4.3.2 Finite element simulation

Again, the procedure used for finite element simulation followed that used before [20]. As shown in Figure 4-1, two models that consists of C3D20R elements (3-dimensional, 20-node quadratic brick elements) are generated, each for half of the specimen length and quarter of the cross section. Point A in each FE model of Figure 4-1 is the location where the center of the cross section is.

Stress-strain relationship for deformation is described using the following constitutive equations, adopted from works in the literature, that is equation 4.1(a) from Neale and Tugcu [24-26], equation 4.1(b) from Ogden [27], equation 4.1(c) from Hollomon [28], equation 4.1(d) from G'Sell and Jonas [8] and Hutchinson and Neale [29] and equation 4.1(e) from ABAQUS manual [30].

$$\sigma(\varepsilon)=\begin{cases} E\,\varepsilon & for\ \varepsilon \le \varepsilon_y \quad (a) \\ d\left[\left\{a\left(\varepsilon+b\right)\right\}^{(c-1)}-\left\{a\left(\varepsilon+b\right)\right\}^{(-c)}\right]+e & for\ \varepsilon_y \le \varepsilon \le \varepsilon_n \quad (b) \\ k\,\varepsilon^{N} & for\ \varepsilon_n \le \varepsilon \le \varepsilon_t \quad (c) \\ k\exp(M\varepsilon^{\beta}) & for\ \varepsilon \ge \varepsilon_t \quad (d) \\ A^{-\frac{1}{n}}\left(\dot{\bar{\varepsilon}}^{cr}\right)^{\frac{1}{n}} t^{-\frac{m}{n}} & for\ \varepsilon \ge \varepsilon_n \quad (e) \end{cases} \tag{4.1}$$

where σ is equivalent stress in MPa, $\dot{\bar{\varepsilon}}^{cr}$ equivalent, uni-axial creep strain rate, ε_y maximum strain before the transition from linear to non-linear deformation, ε_n strain at the neck initiation, and ε_t strain for the on-set of work hardening.

Following the procedure described in the previous study [20], values for parameters in the above equations (E, a, b, c, d, e, k, N, M, β, A, m, and n) are determined by matching the FE-model-generated nominal stress-elongation curve and cross-section reduction with those obtained from mechanical testing. Note that curves from the FE models cannot match with those obtained experimentally without including equation 4.1(e) in the constitutive equation.

With values for the above parameter determined, elastic-plastic deformation can then be separated from the creep deformation, to assess the influence of the strain rate for the elastic-plastic deformation on the stress response. The information is

then used to assess the feasibility of using the strain rate variation determined from the measured total strain to represent the strain rate variation for the elastic-plastic deformation during the necking process.

4.4 Results and Discussion

4.4.1 Experimental

Plots of engineering stress versus elongation are presented in Figures 4-2(a) and 4-2(b) for PE1 and PE2, respectively. The plots indicate that the curve profile up to the peak load does not show not much influence by the change of crosshead speed from 100 to 5 mm/min, but after the peak load the curve profile is broadened by decreasing the crosshead speed, mainly due to the increase of elongation for the on-set of neck propagation. This is consistent with the findings by Viana [3] in which a significant decrease of the peak load and broadening of the curve profile were observed with the decrease of the strain rate.

Note that following the same procedure as that used previously [20], true stress (σ_{true}) and true strain (ε_{true}) are calculated using the following expressions based on the assumption of volume conservation:

$$\sigma_{true} = \frac{P}{W\ t} \tag{4.2a}$$

$$\varepsilon_{true} = ln\left[\frac{W_o\ t_o}{W\ t}\right] \tag{4.2b}$$

where P is the measured load, W and t the width and thickness, respectively, in the neck section, and W_o and t_o the corresponding initial values.

Figure 4-3 depicts typical true axial stress-strain curves at crosshead speeds of 5 and 100 mm/min. The figure suggests that by reducing the crosshead speed, the maximum achievable levels of stress and strain in the neck are reduced, as indicated by the arrows for the end of each stress-strain curve. The curves suggest that reducing the crosshead speed also results in the decreases of the yield stress, which is consistent with the general phenomenon observed in polymers [2-3, 10, 12-13, 16].

Figure 4-4 presents variation of true strain as a function of elongation, to depict the change of cross-sectional area during the necking process. The figure suggests

that by decreasing the crosshead speed from 100 to 5 mm/min, the maximum true strain decreases by more than 10%. This is consistent with that reported before [16]. That is, severity of strain localization during ductile deformation of polymers decreases with the decrease of deformation rate. Similar behavior but less sensitive to the change of crosshead speed was reported for polycarbonate when subjected to plane-strain tension [18].

Strain rate is known to change significantly during the necking process [14]. Figure 4-5 presents the measured range of strain rate variation (based on total deformation) at two crosshead speeds (5 and 100 mm/min), for specimens of two different thicknesses. Each plot in Figure 4-5 indicates that at a given crosshead speed, the strain rate variation is more significant for thinner specimens.

4.4.2 Numerical simulation

Figure 4-6 compares engineering stress-elongation curves generated by FE models and those measured experimentally. The corresponding comparison of reduction in width (W) and thickness (t) for PE1 during the test is shown in Figure

4-7. Trend similar to that shown in Figure 4-7 was obtained from PE2. Overall, the results suggest that deformation in the FE models is in a reasonable agreement with that obtained from the mechanical testing.

Equivalent elastic-plastic stress-strain curves from the simulation results are given in Figure 4-8. The corresponding parameter values for creep deformation, equation 4.1(e), as presented in Table 4-1, show an interesting pattern. That is, value for A depends only on the type of HDPE used for the testing, m on the specimen thickness, and n being constant, independent of either the HDPE type or the specimen thickness. Furthermore, none of those parameters shows any dependence on the crosshead speed.

It is worth noting that a transition, though not significant, occurs at a strain level around 1.5 for PE1 and 1.3 for PE2, as shown in Figure 4-8. Below this strain level, stress generated at 5 mm/min is lower than that at 100 mm/min, but above it, the trend is reversed. Such a transition is believed to be an indication of more pronounced strain hardening at 5 mm/min than at 100 mm/min.

Figure 4-9 presents plots of true axial stress (σ_{11}) versus true strain for nodal point A of the FE models in Figure 4-1. The figure compares elastic-plastic stress-strain

curves with those including creep deformation. The figure also suggests that the maximum elastic-plastic strain generated by necking is higher at a higher crosshead speed.

Strain rates are determined based on variation of strain versus time from the FE models, either with or without the involvement of creep deformation. The results are summarized in Figure 4-10. For clarity, only variation up to the peak value is presented in the figure. As expected, strain rate varies significantly during the necking process, but the range of the strain rate variation is not much affected by including creep deformation in the calculation. Including the creep deformation in the calculation only affects the profile of the strain rate distribution slightly. Thus, with the existence of non-zero creep strain, the range of variation of creep strain rate found to be close to zero. Therefore, the strain rate determined based on the experimentally measured total deformation provides a reasonable range of the strain rate variation for elastic-plastic deformation that occurs during the necking process.

4.5 Conclusions

By combining mechanical testing and FE modeling, the study separates the creep strain from the elastic-plastic strain for HDPE in tension. The experimental testing depicts extensiveness of the strain rate variation during the necking process, of which the trend changes with the change of the cross-sectional aspect ratio and crosshead speed. The test results indicate that by decreasing the cross-sectional aspect ratio or crosshead speed, the strain rate decreases. However, strain hardening during the necking process is more pronounced at 5 mm/min than at 100 mm/min.

Using the FE modeling technique to exclude the creep deformation, variation of the strain rate for elastic-plastic deformation is established for the necking process. Through comparison of the variation of the strain rates determined from the total deformation and those from the elastic-plastic deformation, the study concludes that the variation of strain rates for the elastic-plastic deformation is closely reflected by the values calculated from the measured total deformation during the necking process. Therefore, it is acceptable to use the experimentally-measured and creep-deformation-included strain rates to represent

the actual variation of the strain rates for the elastic-plastic deformation of HDPE during the necking process.

Figures:

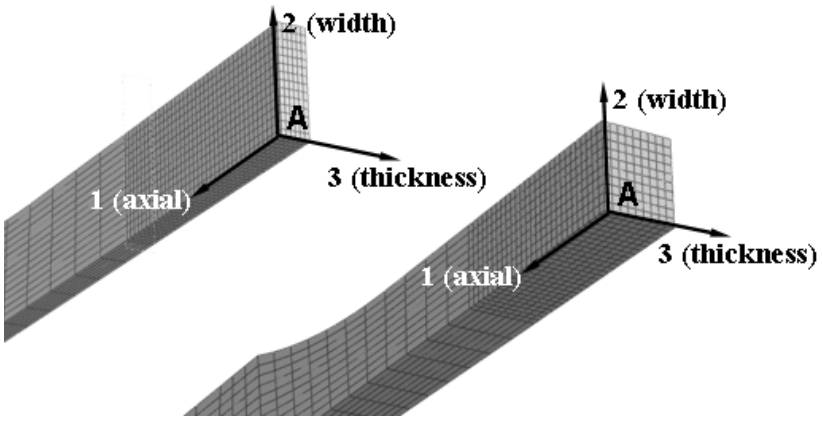

Figure 4-1 Mesh pattern of the dog-bone specimen: 3 mm thick (left) and 10 mm thick (right).

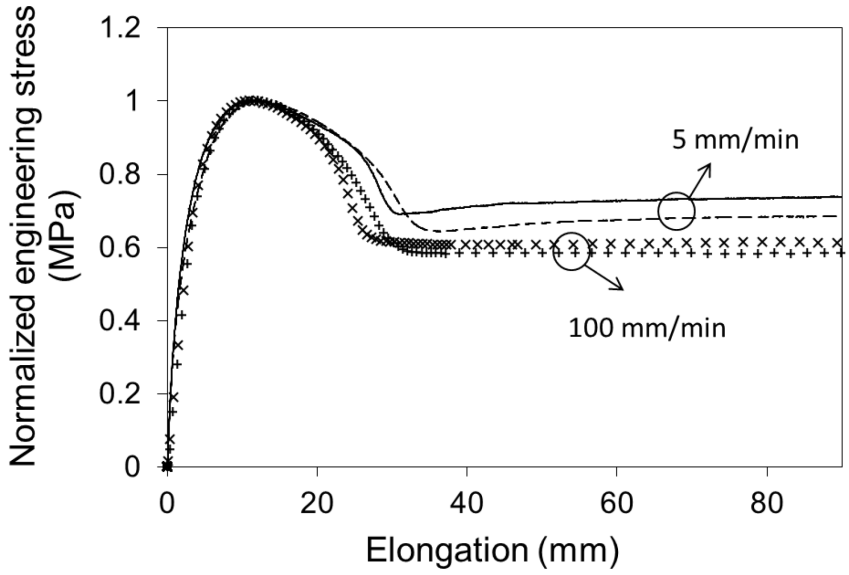

(a)

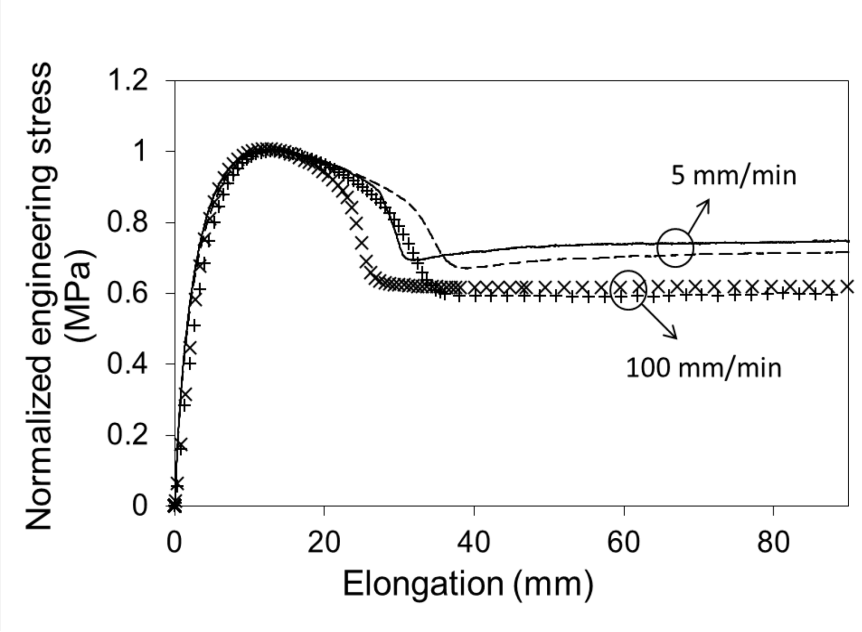

(b)

Figure 4-2 Engineering stress-elongation plots for specimens of different thickness at cross-head speeds of 100 and 5 mm/min, for (a) PE1 and (b) PE2: × for 3 mm thick at 100 mm/min, + for 10 mm thick at 100 mm/min, solid line (—) for 3 mm thick at 5 mm/min, and dotted line (- - -) for 10 mm thick at 5 mm/min.

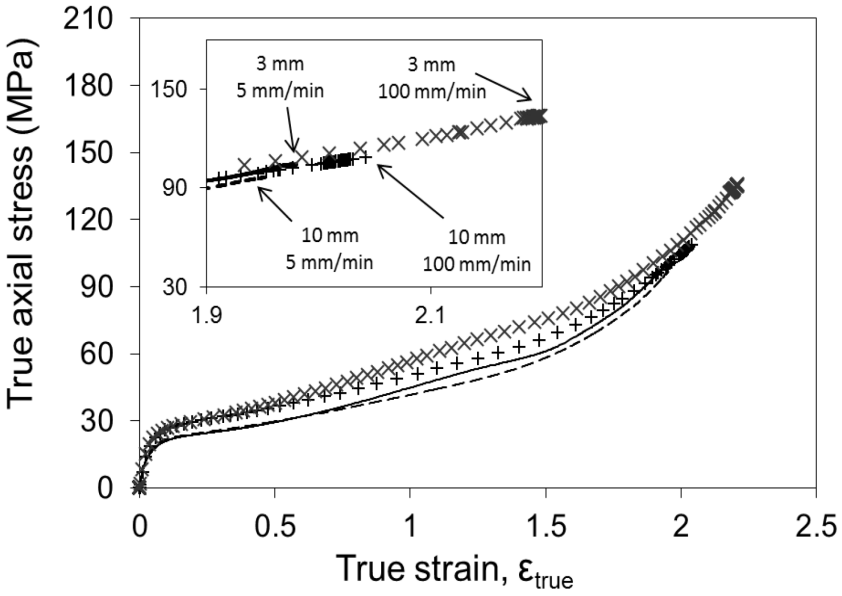

(a)

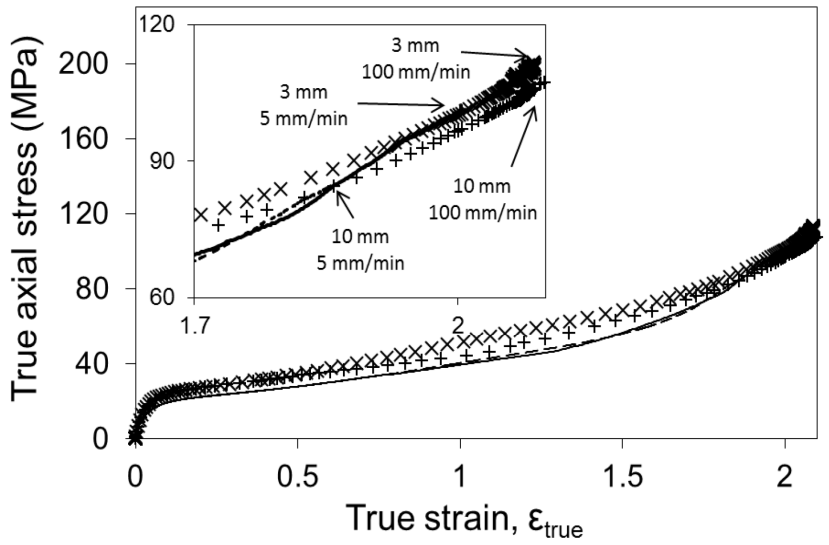

(b)

Figure 4-3 Plots of true axial stress versus true strain for (a) PE1 and (b) PE2 at different thickness and cross-head speeds: × for 3 mm thick at 100 mm/min, + for 10 mm thick at 100 mm/min, solid line (—) for 3 mm thick at 5 mm/min, and dotted line (- - -) for 10 mm thick at 5 mm/min

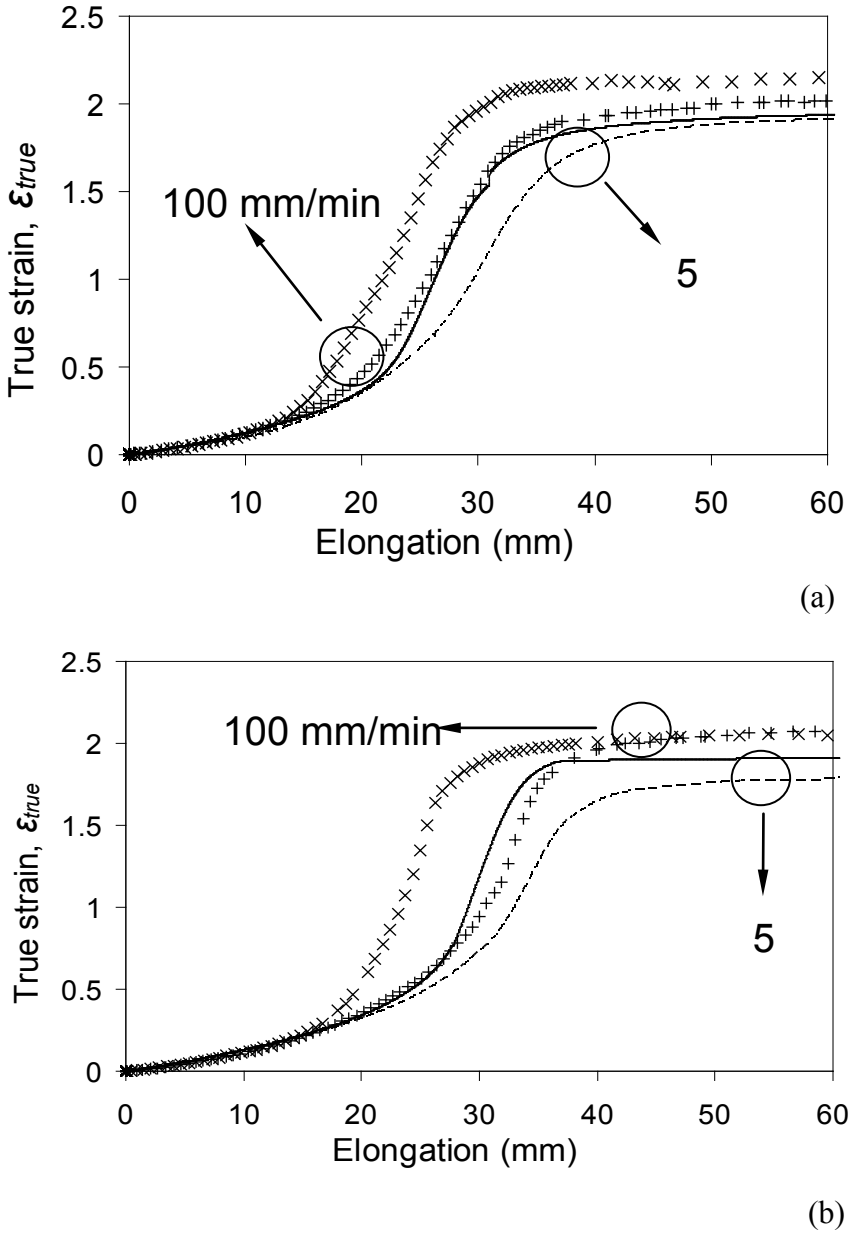

Figure 4-4 Plots of true strain versus elongation for (a) PE1 and (b) PE2 at different thickness and cross-head speed: × for 3 mm thick at 100 mm/min, + for 10 mm thick at 100 mm/min, solid line (—) for 3 mm thick at 5 mm/min, and dotted line (- - -) for 10 mm thick at 5 mm/min.

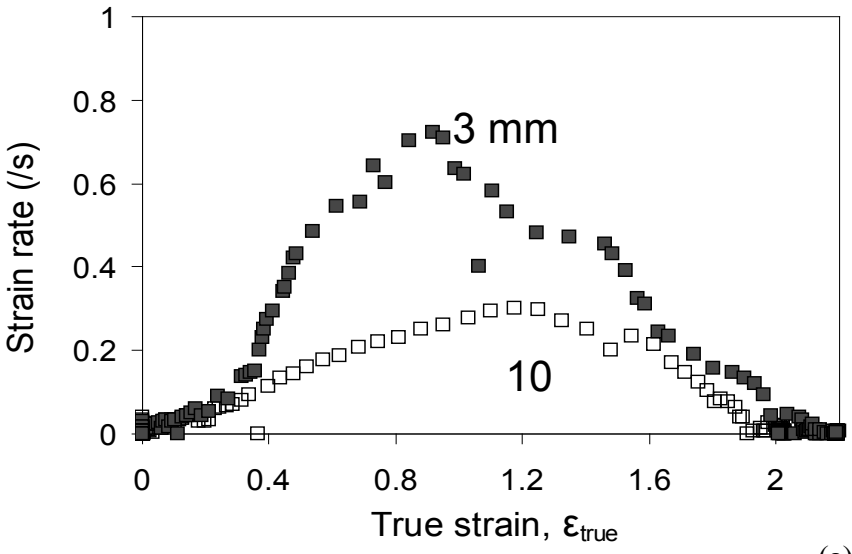
Strain rate (/s)
True strain, ε_{true}
3 mm
10
0
0.2
0.4
0.6
0.8
1
0.4
1.2
1.6
2

(a)

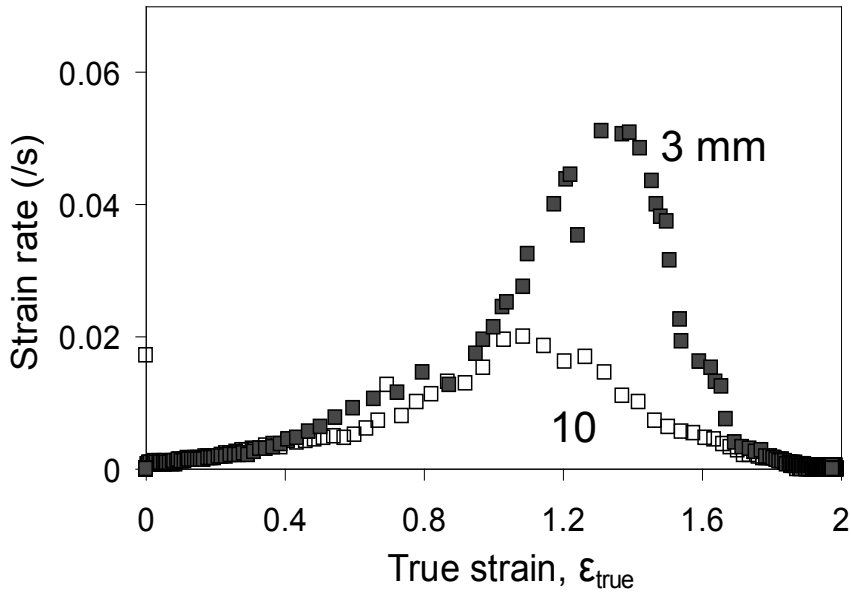
Strain rate (/s)
True strain, ε_{true}
3 mm
10
0
0.02
0.04
0.06
0.4
0.8
1.2
1.6
2

(b)

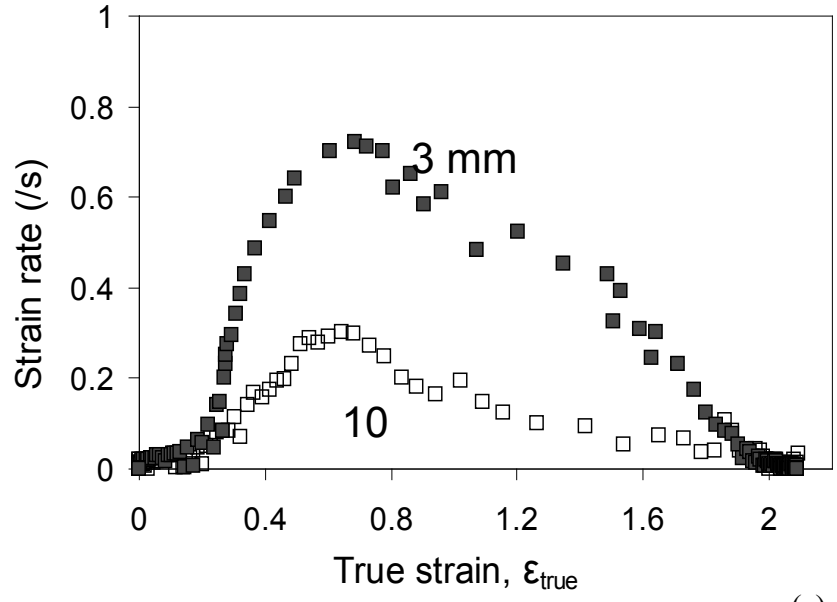

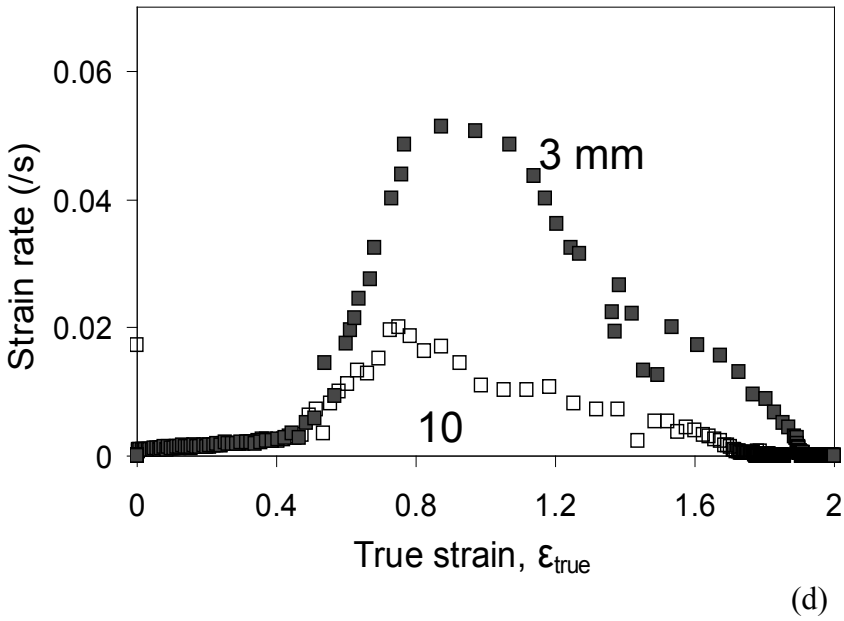

Figure 4-5 Variation of strain rate as a function of true strain for specimens of different thickness in tensile tests: (a) PE1 at 100 mm/min, (b) PE1 at 5 mm/min, (c) PE2 at 100 mm/min, and (d) PE2 at 5 mm/min.

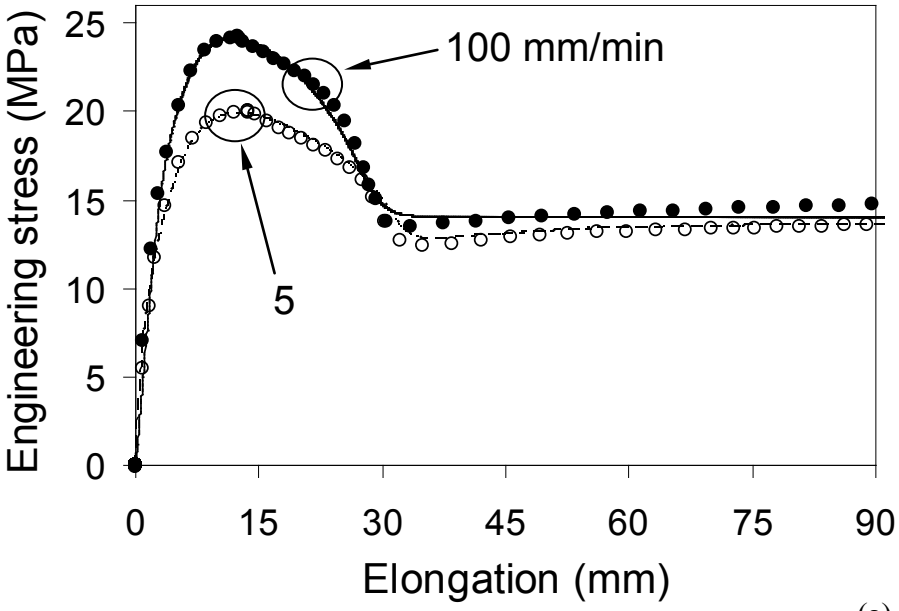
Engineering stress (MPa)
25
20
15
10
5
0
0
15
30
45
60
75
90
Elongation (mm)
100 mm/min
5

(a)

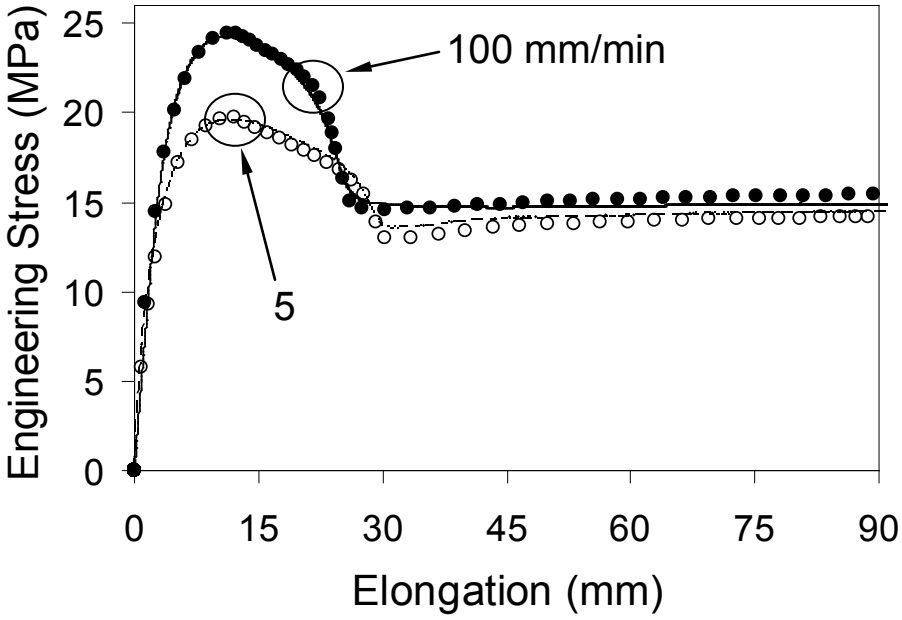
Engineering Stress (MPa)
25
20
15
10
5
0
0
15
30
45
60
75
90
Elongation (mm)
100 mm/min
5

(b)

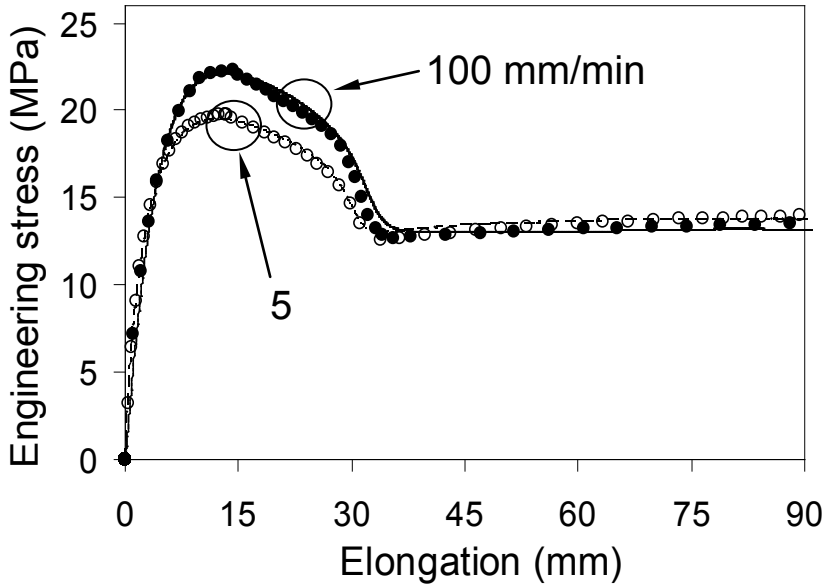

(c)

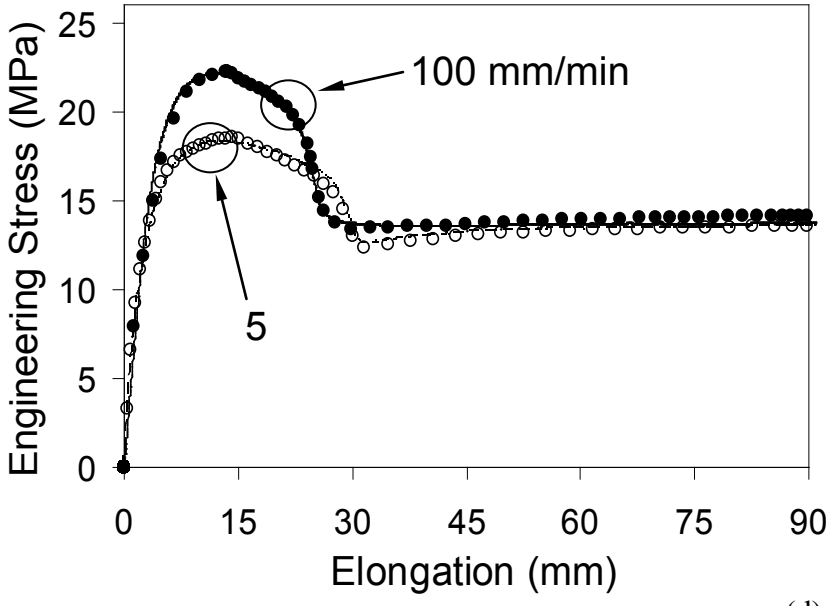

(d)

Figure 4-6 Comparison of engineering stress versus elongation between experimental measurement (solid line for 100 mm/min and dotted line for 5 mm/min) and FE simulation (● for 100 mm/min and ○ for 5 mm/min): for (a) PE1 (10 mm thick), (b) PE1 (3 mm thick), (c) PE2 (10 mm thick), and (d) PE2 (3 mm thick).

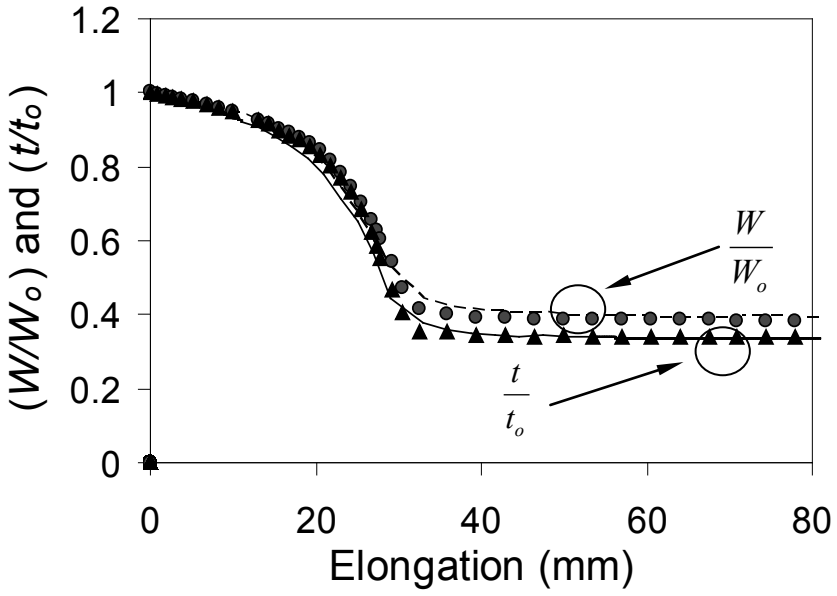
1.2
1
0.8
0.6
0.4
0.2
0
(W/W_o) and (t/t_o)
W/W_o
t/t_o
0
20
40
60
80
Elongation (mm)

(a)

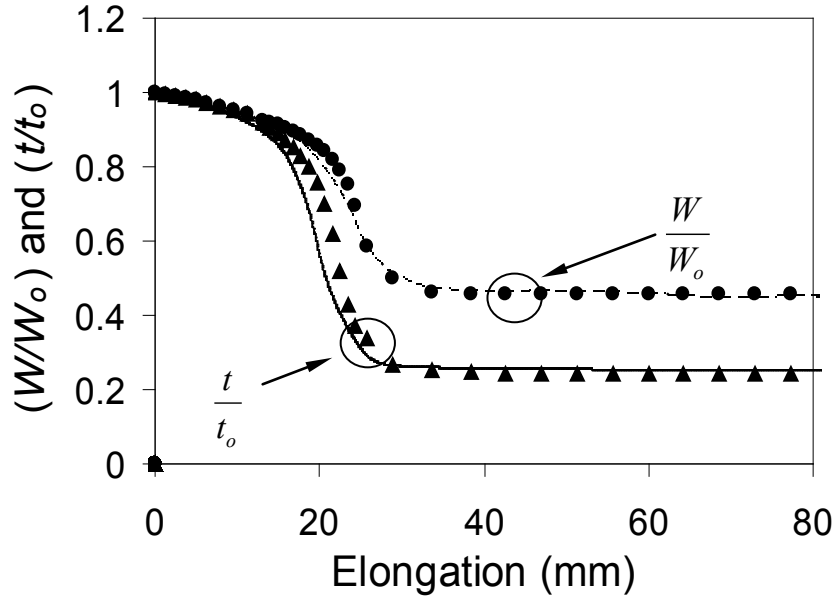
1.2
1
0.8
0.6
0.4
0.2
0
(W/W_o) and (t/t_o)
W/W_o
t/t_o
0
20
40
60
80
Elongation (mm)

(b)

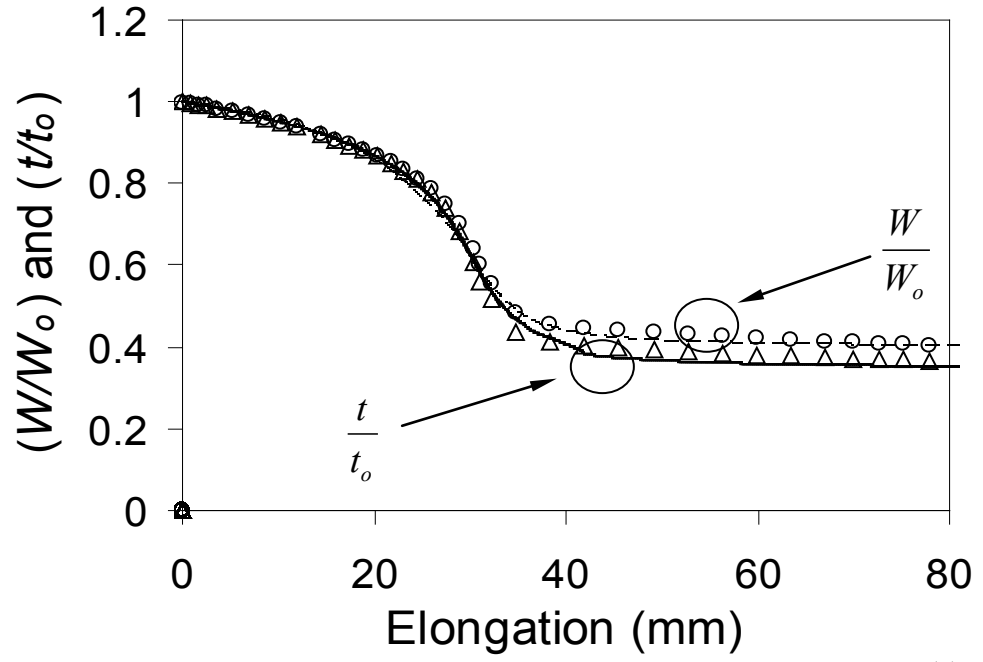

(c)

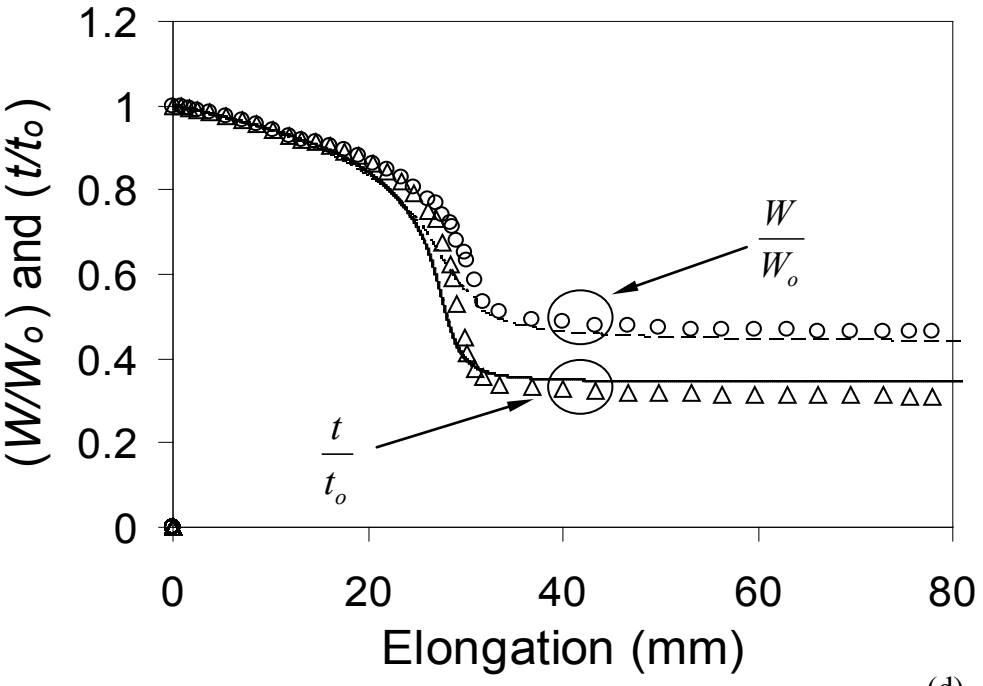

(d)

Figure 4-7 Comparison of the change of normalized width (W/W_o) and normalized thickness (t/t_o) for PE1 during the necking as a function of elongation between experimental measurement and FE simulation, at (a) 100 mm/min (10 mm thick), (b) 100 mm/min (3 mm thick), (c) 5 mm/min (10 mm thick), and (d) 5 mm/min (3 mm

thick). Note that solid line and dotted line represent the experimentally measured t/t_o and W/W_o, respectively, and ▲ and Δ for t/t_o, and ● and ○ for W/W_o from FE simulation.

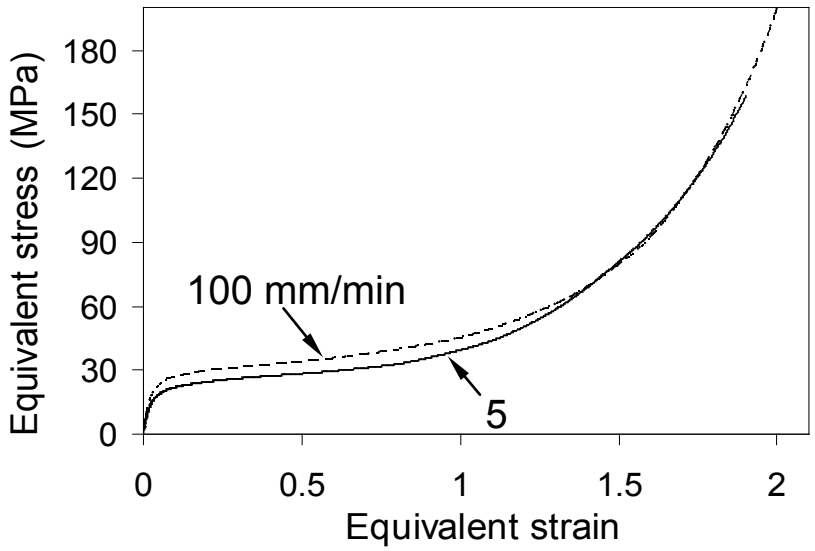

(a)

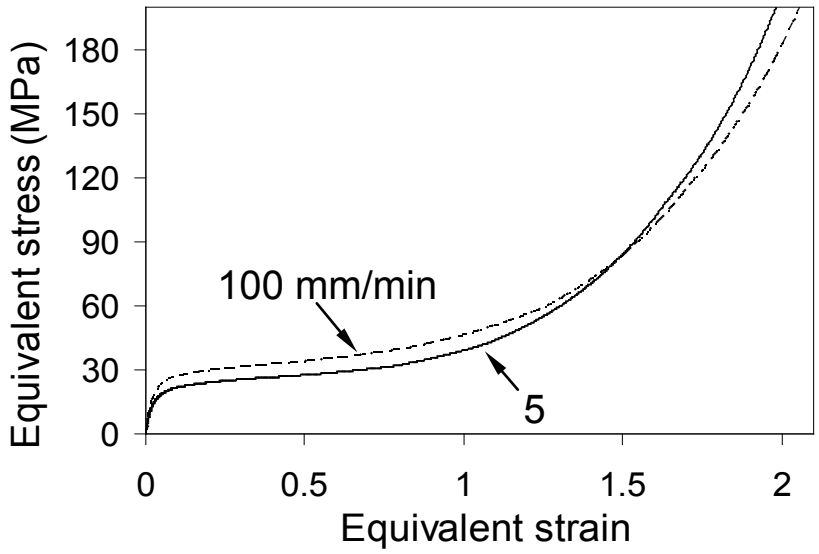

(b)

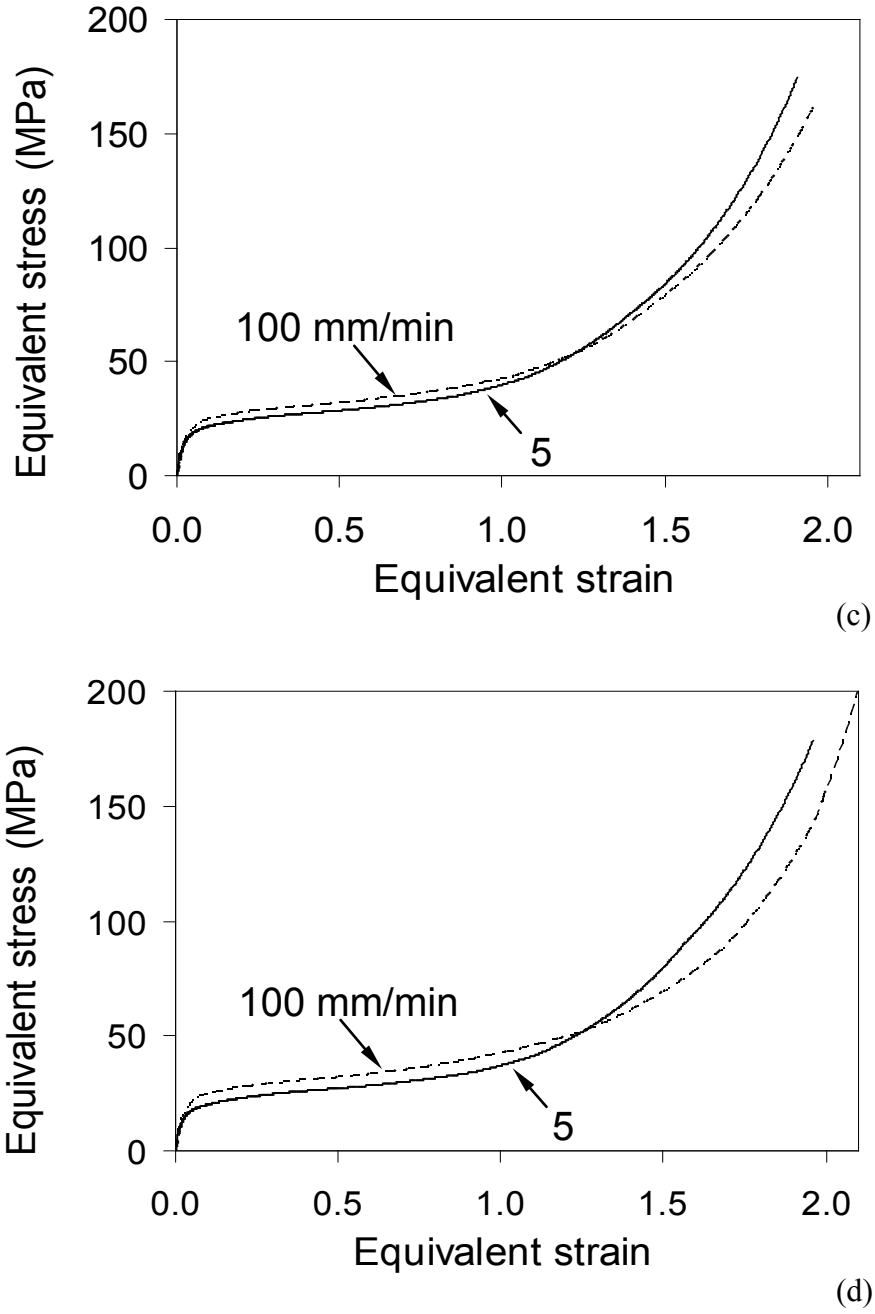

Figure 4-8 Plots of equivalent stress-strain curves at different cross-head speeds: (a) PE1of 10 mm thick, (b) PE1 of 3 mm thick, (c) PE2 of 10 mm thick, and (d) PE2 of 3 mm thick.

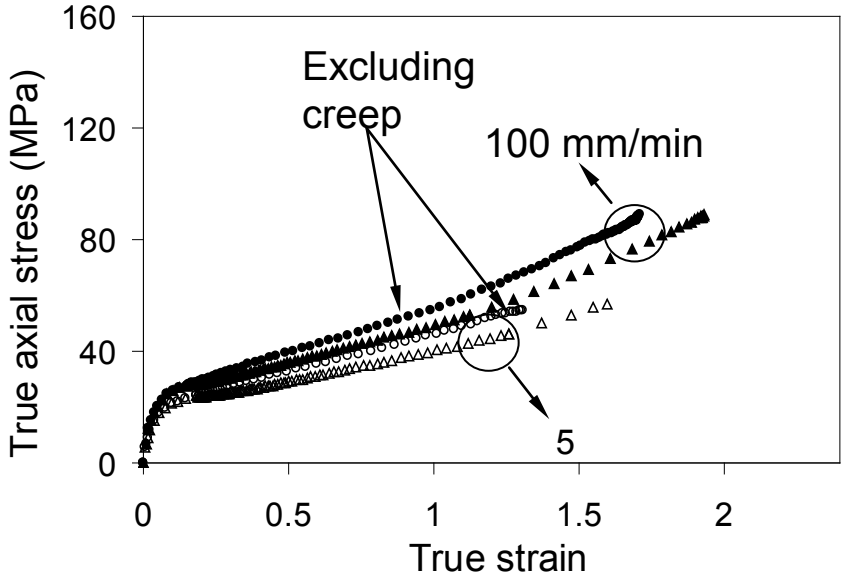
160
120
80
40
0
True axial stress (MPa)
Excluding
creep
100 mm/min
5
0
0.5
1
1.5
2
True strain

(a)

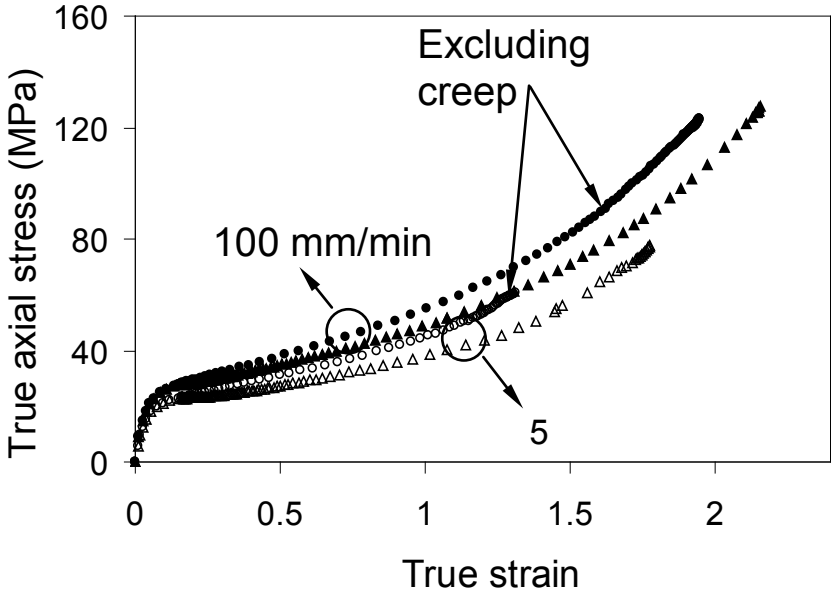
160
120
80
40
0
True axial stress (MPa)
Excluding
creep
100 mm/min
5
0
0.5
1
1.5
2
True strain

(b)

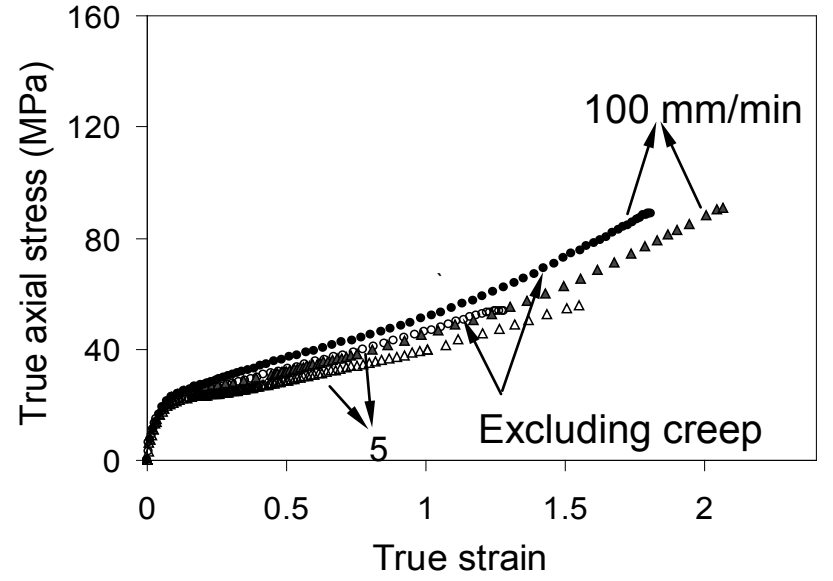

(c)

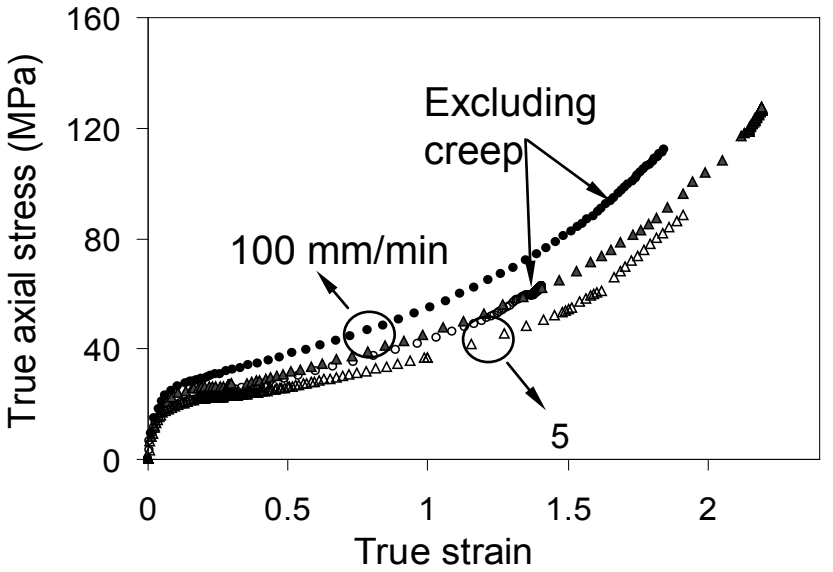

(d)

Figure 4-9 Plots of true axial stress (σ_{11}) versus true strain from FE simulation at crosshead speed of 100 mm/min (▲ with creep and ● without creep), and at crosshead speed of 5 mm/min (Δ with creep and ○ without creep): (a) PE1 of 10 mm thick, (b) PE1 of 3 mm thick, (c) PE2 of 10 mm thick, and (d) PE2 of 3 mm thick.

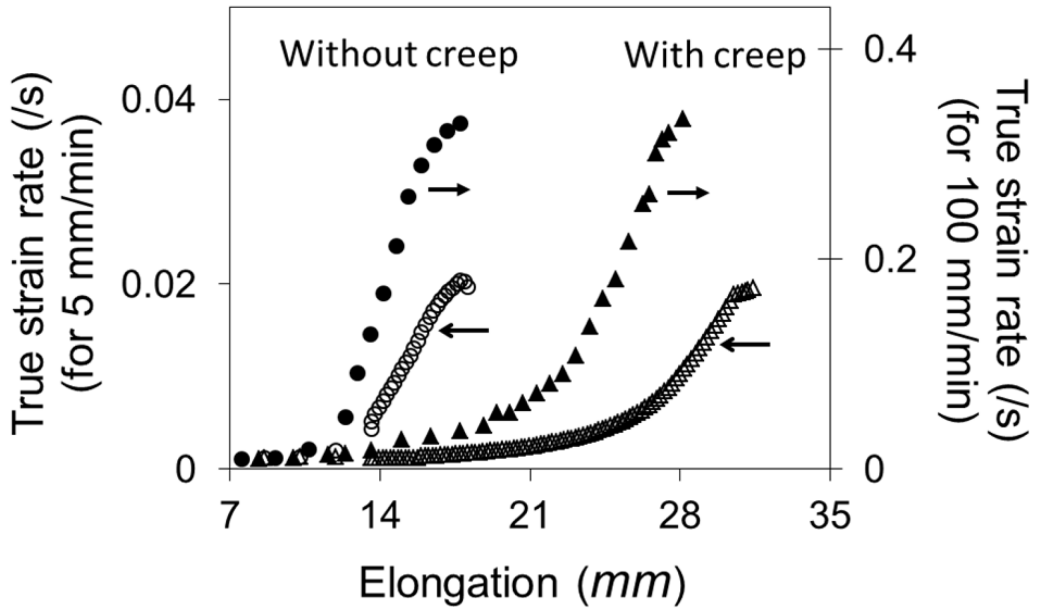
Without creep
With creep
True strain rate (/s)
(for 5 mm/min)
True strain rate (/s)
(for 100 mm/min)
0.04
0.02
0
0.4
0.2
0
7
14
21
28
35
Elongation (mm)

(a)

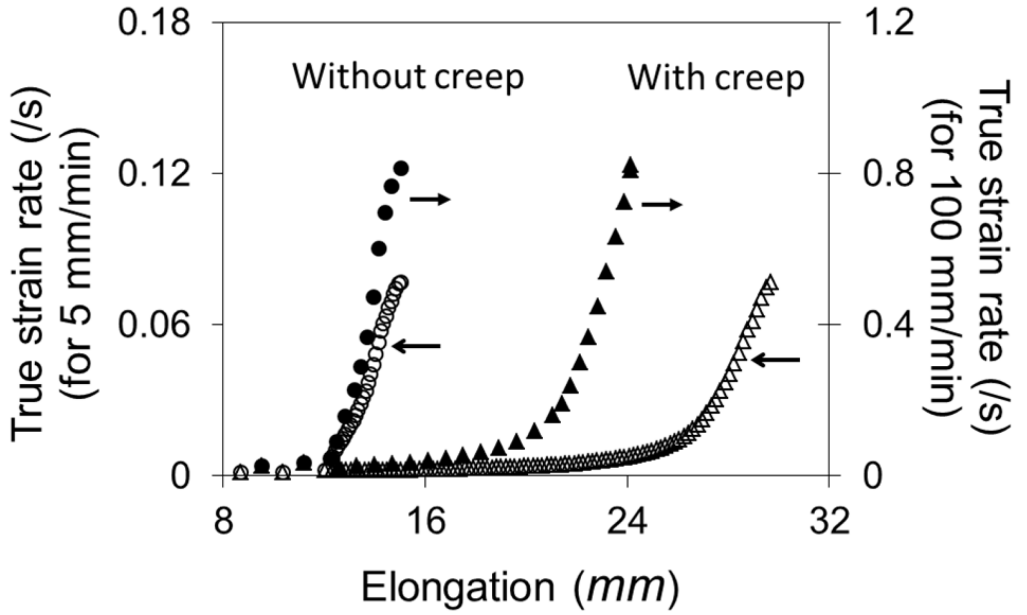
Without creep
With creep
True strain rate (/s)
(for 5 mm/min)
True strain rate (/s)
(for 100 mm/min)
0.18
0.12
0.06
0
1.2
0.8
0.4
0
8
16
24
32
Elongation (mm)

(b)

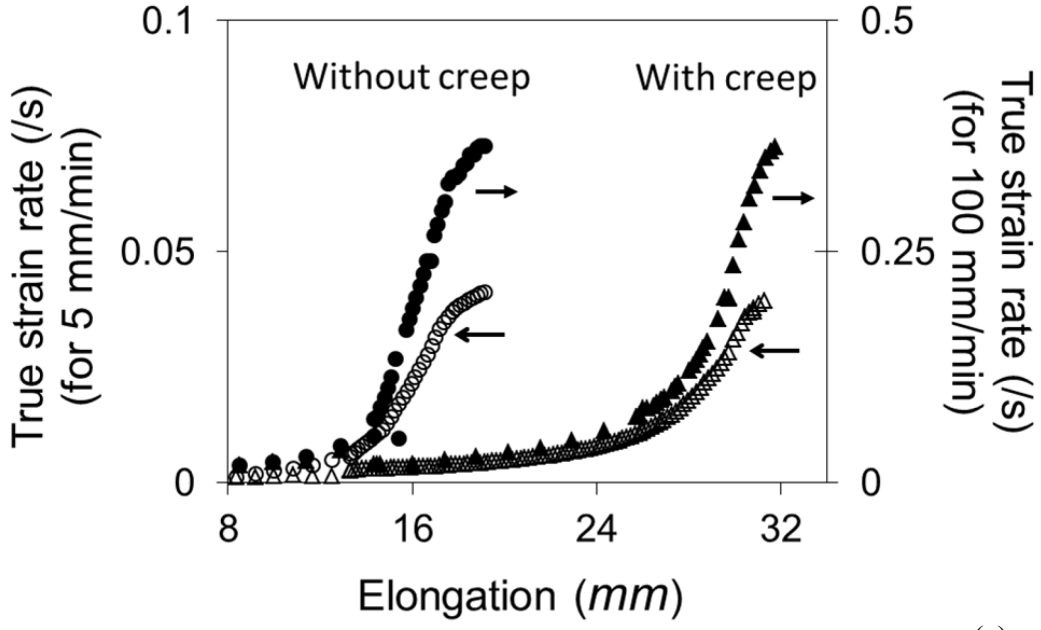

(c)

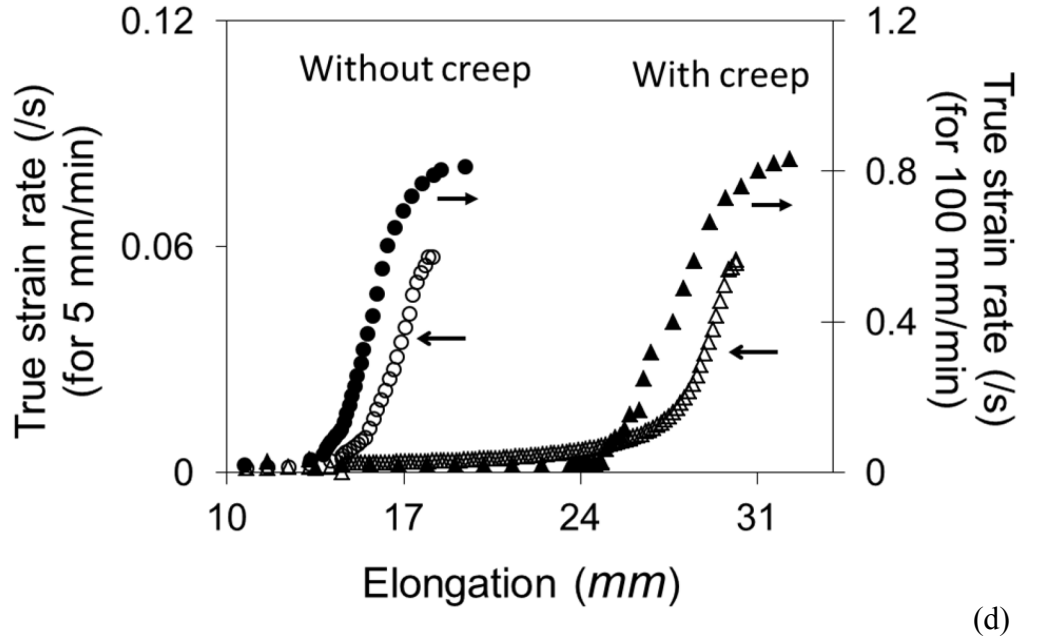

(d)

Figure 4-10 Variation of the range of true strain rate from FE simulation at 100 mm/min (▲ with creep and ● without creep), and at 5 mm/min (Δ with creep and ○ without creep): (a) PE1 of 10 mm thick, (b) PE1 of 3 mm thick, (c) PE2 of 10 mm thick, and (d) PE2 of 3 mm thick.

Tables:

Table 4-1 Parameter values in equation 4.1(e).

Materials	Cross-head Speed (mm/min)	Nominal thickness (mm)	$A \times 10^8$	n	m
PE1	100	10	1.75	4.5	-0.61
		3	1.75	4.5	-0.47
	5	10	1.75	4.5	-0.61
		3	1.75	4.5	-0.47
PE2	100	10	3.35	4.5	-0.61
		3	3.35	4.5	-0.47
	5	10	3.35	4.5	-0.61
		3	3.35	4.5	-0.47

References

1. Automotive Engineering International. April 2007, SAE International, p. 108.

2. Zebarjad, S.M., Sajjadi, S.A.: On the strain rate sensitivity of HDPE/$CaCO_3$ nanocomposites. Mater. Sci. Eng. A 475, 365-367 (2008).

3. Viana, J.C.: Structural interpretation of the strain-rate, temperature and morphology dependence of the yield stress of injection molded semicrystalline polymers. Polymer 46, 11773-11785 (2005).

4. Wesseloo, J., Visser, A.T., Rust, E.: A mathematical model for the strain-rate dependent stress-strain response of HDPE geomembranes. Geotextiles Geomembr. 22, 273 (2004).

5. Osman, M.A., Rupp, J.E.P., Suter, U.W.: Tensile properties of polyethylene-layered silicate nanocomposite. Polymer 46, 1653-1660 (2005).

6. Tabiei, A., Yi, W., Goldberg, R.: Non-linear strain rate dependent micro-mechanical composite material model for finite element impact and crashworthiness simulation. Int. J. Non-Linear Mech. 40, 957-970 (2005).

7. Hadriche, I., Ghorbel, E., Masmoudi, N., Halouani, F.E.: Influence of strain rate on the yielding behavior and on the self heating of thermoplastic polymers loaded under tension. Key Eng. Mater. 446, 63-72 (2010).

8. G'Sell, C., Jonas, J.J.: Determination of the plastic behavior of solid polymers at constant true strain rate. J. Mater. Sci., 14, 583-591 (1979).

9. Roland, C.M., Twigg, J.N., Vu, Y., Mott, P.H.: High strain rate mechanical behavior of polyurea. Polymer 48, 574-578 (2007).

10. Lim, S.H., Yu, Z.Z., Mai, Y.W.: Effects of loading rate and temperature on tensile yielding and deformation mechanisms of nylon 6-based nanocomposites. Composites Sci. Tech. 70, 1994-2002 (2010).

11. Ward, I.M., Hadley, D.W.: Mechanical properties of solid polymers. Wiley, Chichester, UK (2000).

12. Liu, Y., Truss, R.W.: A study of tensile yielding of isotactic polypropylene. J. Polym. Sci. Part B: Polym. Phys. 32(12), 2037-2047 (1994).

13. Bao, S.P., Tjong, S.C.: Mechanical behaviors of polypropylene/carbon nanotube nanocomposites: The effects of loading rate and temperature. Mater. Sci. Eng. A 485, 508-516 (2008).

14. Fang, Q.Z., Wang, T.J., Beom, H.G., Zhao, H.P.: Rate-independent large deformation behavior of PC/ABS. Polymer 50, 296-304 (2009).

15. Boyce, M.C., Arruda, E.M.: An experimental and analytical investigation of the large strain compressive and tensile response of glassy polymers. Polym. Eng. Sci. 30, 1288-1298 (1990).

16. Li, H.X., Buckley, C.P.: Evolution of strain localization in glassy polymers: A numerical study. Int. J. Solids Structures 46, 1607-1623 (2008).

17. Li, H.X., Buckley, C.P.: Necking in glassy polymers: Effects of intrinsic anisotropy and structural evolution kinetics in their viscoplastic flow. Int. J. Plasticity 26, 1726-1745 (2010).

18. Wu, P.D., van der Giessen, E.: On neck propagation in amorphous glassy polymers under plane strain tension. Int. J. Plasticity 11, 211-235 (1995).

19. Kwon, H.J., Jar, P.-Y.B.: On the application of FEM to deformation of high-density polyethylene. Int. J. Solids Structures 45, 3521-3543 (2008).

20. Muhammad, S., Jar, P.-Y.B.: Effect of aspect ratio on large deformation and necking of Polyethylene. J. Mater. Sci. 46, 1110-1123 (2010).

21. Klepaczko , J.: Thermally activated flow and strain rate history effects for some polycrystalline FCC metals. Mater. Sci. Eng. 18, 121-135 (1975).

22. Hoge, K.G., Mukherjee, A.K.: The temperature and strain rate dependence of the flow stress of tantalum. J. Mater. Sci. 12, 1666-1672 (1977).

23. Armstrong, R.W., Walley, S.M.: High strain rate properties of metals and alloys. Int. Mater. Rev. 53(3), 105-128 (2008).

24. Neale, K.W., Tugcu, P.: Analysis of necking and neck propagation in polymeric materials. J. Mech. Phys. Solids 33, 323-337 (1985).

25. Neale, K.W., Tugcu, P.: Approximate methods for analyzing the cold drawing of polymeric fibres and films. Int. J. Numer. Methods Eng. 25, 99-112 (1988).

26. Tugcu, P., Neale, K.W.: Analysis of plane-strain neck propagation viscoplastic polymeric films. Int. J. Mech. Sci. 29, 793-805 (1987a).

27. Ogden R.W.: Large deformation isotropic elasticity: on the correlation of theory and experimental for compressible rubberlike solids. Proc. Royal Soc. London, Ser. A (Math. Phys. Sci.) 328, 567-583 (1972).

28. Hollomon, J.H.: Tensile deformation. Trans. Metall. Soc. Am Inst. Mining and Metallurgical Engineers 162, 268-290 (1945).

29. Hutchinson, J.W., Neale, K.W.: Neck propagation. J. Mech. Phys. Solids 31, 405-426 (1983).

30. ABAQUS manual: Rate-dependent plasticity: creep and swelling. ABAQUS Analysis User's Manual v 6.7, Section 18.2.4. ABAQUS Inc. (2007).

CHAPTER - 5

Cavitation-Induced Rupture in High-Density Polyethylene Copolymers

5.1 Introduction and Background

Cavitation is known to be involved in many polymer products during the failure process. Its occurrence often results in a whitening appearance that is similar to that from crazing or shear yielding [1-2]. However, crazing or shear yielding does not reduce load-carrying capacity of the polymers, but cavitation does. Therefore, ability to detect cavitation, and to distinguish it from crazing or shear yielding, is crucial for characterizing load-carrying capacity of the polymer products.

Previous studies that combined mechanical testing with microscopic examination or X-ray scattering to identify the loading conditions for cavitation, have suggested that cavitation in semi-crystalline polymers usually starts between lamellae or among spherulites, and that cavitation is likely to be responsible for the ductile-brittle transition in semi-crystalline polymers [e.g. 3-7]. Unfortunately, the amount of cavities reported in most studies is too small to register any disturbance in the test results (i.e. load and displacement). Later, sharp notches are considered to encourage bulk cavitation [5-6]. But, due to crack growth from the notch tips, loading conditions for the bulk cavitation are extremely difficult to identify.

One attempt to generate cavitation without the involvement of crack growth is through the use of diabolo specimens [8]. The idea came from the similarity between the significantly narrowing profile of diabolo shape and the necking profile. Therefore, it was expected that the use of diabolo specimens could induce a significant increase in the hydrostatic stress level, thus encouraging cavitation in the specimens. It turned out that the amount of cavities generated in this type of specimens was still too small to register any noticeable disturbance in the

recorded signals, thus not suitable for establishing the loading conditions for cavitation. In another approach, G'Sell et al. [9] proposed the use of rectangular bars that contained a section of slightly reduced width to encourage cavitation. The results showed that at an axial strain about 4%, volume strain in the reduced section started to rise steadily. However, the increase in volume strain could not be completely attributed to the cavitation, as crazing could also cause the volume strain increase. Furthermore, examination of the post-tested specimens did not show any evidence to suggest that cavitation is responsible for the volume strain increase.

Despite difficulties in generating bulk cavitation in semi-crystalline polymers, such behaviour has been observed in rubber more than half a century ago. Gent and Lindley [10] demonstrated the bulk cavitation behaviour in short cylindrical specimens of rubber when subjected to tensile loading. The bulk cavitation caused a noticeable disruption on the load-displacement curve, but afterwards, the load resumed the initial trend of increase with further stretch until the final breakup. Disruption on the load-displacement curve by the cavitation was found to be highly reproducible and clearly identifiable using specimens of the short length.

Based on the observation, Gent and Lindley suggested that the hydrostatic tensile stress level (also known as negative pressure) be responsible for the occurrence of bulk cavitation. This argument has since been supported by several works in the literature [11-13].

Results to be presented in this paper will show that bulk cavitation can also be generated in coupon specimens of high-density polyethylene copolymer (HDPE) without the presence of sharp notches. Study presented here investigates bulk cavitation in two types of HDPE, one with broad molecular weight distribution and the other narrow. Both experimental study and finite element simulation are used to characterize the cavitation generated in the specimens and the associated hydrostatic stress level. The results are used to discuss the specimen design order to encourage bulk cavitation, loading conditions for its occurrence, and characterization of the post-cavitation deformation behaviour.

It should be noted that for the purpose of comparison, necking behaviour in those HDPEs are also presented. The corresponding load-displacement curves, along with finite element simulation, are used to establish constitutive equations that are

then applied to a finite element model of specimen with short gauge length, to determine the hydrostatic stress level involved for the bulk cavitation.

5.2 Material and Test Set-up

Four HDPEs were used in the study, two containing hexene co-monomers (H-series) and the other two octene co-monomers (O-series). Characteristics of the HDPEs, such as number-averaged (M_n) and weight-averaged (M_w) molecular weights, molecular weight distribution (M_w/M_n) and density, are listed in Table 5-1. All polymers used in this study were supplied by NOVA Chemicals as rectangular plates that were compression-molded with nominal thickness of 10 mm. Isotropy and constant crystallinity were ensured by NOVA Chemicals. Cylindrical rods of 9 mm in diameter and 140 mm in length were machined from the plates, with a gauge section of 6 mm in diameter introduced in the middle part of the rods. Length of the gauge section was either 20 or 1.8 mm, thus referred to as “long” or “short” specimens, respectively. Photographs of the long and short specimens are shown in Figure 5-1(a), and details of dimensions in the gauge

section in Figure 5-1(b). Note that due to symmetry, Figure 5-1(b) only presents upper half of the gauge section, and to save space, drawing of the long specimen does not follow the geometrical proportionality except the dimensions specified in the drawing. For the long specimen in Figure 5-1(b), diameter in the middle part of the gauge section is slightly reduced, in order to ensure that necking is always initiated there. In the rest of the chapter, specimens are referred to according to the type of HDPE used (H- or O-series) and gauge length of the specimens (long or short). For example, specimens made of H-1 HDPE in Table 5-1 with gauge length of 1.8 mm will be referred to as H-1 short specimens.

The above two gauge lengths were chosen to generate distinctively different deformation behaviour, that is, the long specimens for necking and the short ones for cavitation. Contraction of the cross section, due to axial elongation followed by either necking or cavitation, was recorded using a standard MTS axial extensometer of which the clamps had been modified to be attachable to a chosen cross section during the test. To ensure that the diameter was measured in consistent accuracy, the extensometer was calibrated before each series of tests. Note that after bulk cavitation has occurred in the short specimens, the measured

diameter can no longer be used to determine the true cross sectional area. But, those values are still used in this study to determine the "true stress" for the plots presented here. This is because the plots that include those true stress values provide a clear indication for the occurrence of the bulk cavitation.

In this study, axial strain is defined based on the change of the cross sectional area. That is, the axial strain value is assumed to be equal to $ln\ (A_o/A)$, where A_o is the initial cross sectional area and A the cross sectional area at the moment of the measurement. Such a definition of strain is based on volume conservation during the plastic deformation, which is obviously violated after the bulk cavitation has occurred. However, plots presented in this paper still include strains determined in this way after the bulk cavitation, as the change of the trend line in those plots provides a clear indication for the occurrence of the bulk cavitation.

As the short specimens used in this study do not contain any sharp notch, their deformation process does not involve crack growth from the notch tip. Rather, breakage of the short specimens is through the split of cylindrical shell that is formed from the bulk cavitation. This kind of breakage is different from the

fracture process reported in the literature. The latter, such as that reported in refs. [5-6], always involves crack growth from the notch tips.

Design of the short specimens is inspired from a finite element analysis that is initially for simulation of neck forming process in HDPE [14]. The analysis shows that hydrostatic stress rises at a relatively fast rate just before the neck reaches the final dimensions. This phenomenon is consistent with the suggestion from an early study [15]. The fast rise of hydrostatic stress in the necking process made us wonder whether the hydrostatic stress could be further increased by restricting the neck development, achieved through shortening the gauge length. Through the observation of the necking process in the long specimens, a minimum gauge length of around 6 mm was found to be necessary for the gauge section to reach the final dimension of a neck. Therefore, specimens with a gauge length shorter than 6 mm should impose some constraint on the neck development. Effectiveness of the constraint should increase by decreasing the gauge length from 6 mm. However, the gauge length could not be extremely short. Otherwise, stress concentration at the end of the gauge section, where the original cross sectional diameter changes from 6 to 9 mm, would have dominated

the stress state in the gauge section, resulting in crack initiation from the end of the gauge section.

In addition to the above limiting factor for the shortness of the gauge length, shortness of the gauge length has another restriction, which is to accommodate an extensometer for the measurement of the cross sectional diameter during the test. A preliminary investigation suggests that a gauge length of 1.8 mm is appropriate for the short specimens. As to be shown in the results section, bulk cavitation can be generated in all HDPEs using short specimens with such a gauge length.

Mechanical tests were conducted at room temperature, using a universal testing machine (QUASAR 100) at a crosshead speed of 5 mm/min. At least 3 tests were conducted for each type of specimens. Specimens were first firmly held using special steel clamps to prevent slippage of the grip during the test. Gripping length was set to be 50 mm from each end of the specimen, to leave 40 mm in the middle for stretch during the tests (i.e. twice of the gauge length of the long specimens).

Testing of long specimens was terminated when the stroke reached 60 mm, because at this point the neck had been fully developed and propagated a

sufficient distance in the loading direction. On the other hand, testing of short specimens was allowed to continue after the cavitation had occurred, until the specimens were fully broken into two halves. Breakage of the short specimens, however, occurred at a relatively short stroke of less than 12 mm.

In addition to the above mechanical tests, one H-1 short specimen was unloaded immediately after a fast load drop had occurred. The specimen was then cut open to reveal the cavity that had been generated in the central part of the gauge section.

5.3 Finite Element Simulation

Finite element modeling (FEM), using ABAQUS v6.7, was conducted to estimate hydrostatic stress level generated in short specimens. The models were based on CAX8R axis-symmetric 8 node elements. Due to symmetry, each model corresponds to a quarter of the cut-off section, as shown in Figure 5-2(a) for the long specimen and Figure 5-2(b) for the short specimen. Note that contour profile in those models follows closely the true specimen geometry, even for the corner profile at the end of the gauge section and the defect shape in the middle of the

long specimen. The model of long specimen has 909 elements and 2918 nodes, and the model of short specimen 1064 elements and 3385 nodes.

Constitutive equation was established following a procedure described in the previous study [14], based on test results from long specimens of H-1 and O-2 that were also used in ref. [14], but in the previous work, the specimens were standard dog-bone specimens of rectangular cross section. The constitutive equation enables the model of the long specimen to generate load-displacement curve and cross section reduction that mimic those obtained experimentally, including the deformation during the neck forming process. However, similar to that discovered before [14], the FEM cannot mimic both the experimentally-determined load-displacement curve and cross section reduction without the consideration of creep deformation. Therefore, following the previous approach, a simple power-law creep function is introduced here to adjust the strain increase during the necking process, in order for the FEM-generated load-displacement curve and deformation behaviour to match with the experimentally-measured data. Expression for the power-law creep function is:

$$\dot{\varepsilon}_{cr} = Aq^n t^m \tag{5.1}$$

where $\dot{\varepsilon}_{cr}$ is the creep strain rate, q the equivalent stress, t the time with zero set at the maximum load, and A, m, and n constants.

5.4 Test Results and Rupture Behaviour

Results presented in this section are based on data from one specimen for each type of HDPE, as specimens of the same type produce very similar results that contain only minor difference.

Figure 5-3 presents typical test results from long (marked L in the figure) and short (marked S) specimens: Figure 5-3(a) for engineering stress versus stroke and Figure 5-3(b) for true axial stress versus *ln* (A_o/A). Arrow in each figure indicates the point where the bulk cavitation occurs in the short specimen. Figure 5-3(a) suggests that the occurrence of bulk cavitation induces fast load drop, causing significant reduction of data density in this part of the curve, while in Figure 5-3(b) the corresponding change is the trend line of the curve. As

mentioned earlier, although values calculated for true axial stress and cross-sectional area do not bear any physical meaning after the bulk cavitation has commenced, the data are still included in Figure 5-3(b) to illustrate the possibility of using the change of the trend line to identify the occurrence of bulk cavitation.

Figure 5-3(b) contains two additional vertical lines, each drawn from the abscissa to intersect with either curve S or curve L. The point where the vertical line intersects with the curve corresponds to the point of maximum load in Figure 5-3(a). Its position in the figure clearly suggests that true axial stress continues to increase after the maximum load has been reached, and its rate of increase for the short specimen is faster than that for the long specimen.

Figure 5-4 presents photographs taken from the post-tested specimens. Figure 5-4(a) shows the typical necking behavior for all long specimens of both H- and O-series HDPEs. The necked region has a fairly constant cross section that is distinctly smaller than the un-necked section. Figure 5-4(b) shows the typical rupture behavior of the H-series short specimens, and Figure 5-4(c) the O-series. Clearly, the O-series short specimens survived a longer stroke than the H-series

counterparts, but none of them developed a full neck as that shown in Figure 5-4(a).

Figure 5-4(d) was taken from a cut-off gauge section of an H-1 short specimen that had been unloaded immediately after the sharp load drop to ensure that cavities are fully developed and to avoid shrinkage of cavities at unloading. Direction of the specimen gauge length is indicated by a double arrow at the bottom of Figure 5-4(d). The photograph shows a flattened cavity in the core of the gauge section, suggesting that after the sharp load drop, cavity is formed in the core of the gauge section.

Figure 5-5 presents photographs for a close view of the rupture behaviour in the short specimens. Bulk cavitation is indicated by the presence of a crate at the centre of the cross section. The crate was formed by stretching the cavity before the final breakage. The two photographs in Figure 5-5 also suggest that at the rupture location the cylindrical shell of H-series is thinner than that of O-series.

Plots of engineering stress (defined as load per unit area of original cross section) versus stroke for all long specimens (2 H-series and 2 O-series) are shown in Figure 5-6. Note that in order to exclude minute difference among the curves,

which comes from the difference in the tensile strength (varying from 20 to 22 MPa, as shown in Table 5-1), engineering stress in Figure 5-6 has been normalized using the maximum stress value for each curve. Those plots are nearly identical except during the stress drop section. Similar difference has been reported previously [14] using the same H-1 and O-2, but obtained from standard dog-bone specimens of rectangular cross section. As suggested before, the slight, but noticeable difference in the stress-drop section is probably due to the difference in the creep resistance. That is, H-series has better creep resistance than O-series.

Figure 5-7 summaries normalized engineering stress versus stroke from all short specimens. Those plots show little difference before the cavitation. But after the cavitation, the plots for the O-series (open symbols) lie above those for H-series (solid symbols), and the former survive a stroke that is about 50% longer than the latter. This phenomenon is consistent with the difference in the residual stretch between H- and O-series short specimens, as illustrated in Figures 5-4(b) and 5-4(c).

Figure 5-8 compares reduction of the external diameter in the gauge section of H- and O-series short specimens. The figure also includes data from long specimens as a reference. Curve profiles among those from long specimens show slight variation, with the curves for O-series lying to the right of H-series. However, such a difference, though small, does not exist at all among curves from the short specimens, suggesting that outer diameter of all short specimens contracted in a very similar manner, even after bulk cavitation had occurred.

5.5 Results from FEM Simulation

Figure 5-9 depicts the input of equivalent stress and strain for H-1 and O-2 HDPEs, to enable the FEM model of long specimens to mimic the load-displacement curve and cross section reduction in their necking process. The corresponding values for constants in the power-law creep function, Eqn. (5.1), are listed in Table 5-2. Based on those input data, engineering stress-elongation curves generated from the FEM model are presented in Figure 5-10 (discrete points), and compared with those from the experimental testing (solid lines). The

comparison suggests a reasonably good agreement between simulation and experimental testing.

At the strain level for bulk cavitation (about 0.3 for $ln\ A_o/A$), the two curves in Figure 5-9 are almost identical, except the initial slope in the linear region, as indicated by Young's modulus in Table 5-2. Values of the constants m and n in Eqn. (5.1) are also identical, but constant A for O-2 is nearly twice of that for H-1. This suggests that O-2 has lower creep resistance than H-1, consistent with that shown in Figure 5-6 in which the load-drop section for the O-2 curve lies to the right of the H-1 curve. Note that the same conclusion has been drawn from a previous study using dog-bone specimens of a rectangular cross section [14].

By applying the equivalent stress-strain relationships given in Figure 5-9 to the FEM model of short specimen, Figure 5-2(b), hydrostatic stress in the core of the gauge section is determined and plotted as a function of axial strain in Figure 5-11, marked "S" in the figure. Figure 5-11 also includes plots from the model of long specimens for comparison (marked "L" in the figure). Solid lines in Figure 5-11 are for H-1 and dashed lines for O-2. Plots in the figure clearly suggest that hydrostatic stress level in the short specimens can be raised to around 30 MPa at

an axial strain level less than 0.2, which is about three times of the hydrostatic stress level in long specimen at the same axial strain level. However, since the current FEM models cannot mimic the cavitation process, the simulation was terminated by choosing an arbitrary criterion, that is, after the load has dropped about 5% from the maximum value. As a result, the maximum hydrostatic stress given in Figure 5-11 does not necessarily represent the critical hydrostatic stress level for the bulk cavitation. Nevertheless, the figure clearly shows the effectiveness of using short specimen to raise the hydrostatic stress level in HDPE.

Figure 5-12 presents contour plots of hydrostatic and maximum principal stresses of the short specimen at the maximum elongation used in the simulation (around 2 mm). The contour plots indicate that high stress is located in the core region, away from the corner at the end of the gauge section. Therefore, stress concentration at the end of the gauge section, due to the change of cross sectional area, has a negligible influence on the maximum hydrostatic and maximum principal stress values.

5.6 Discussion

Specimen design to initiate cavitation

In view of the cavitation behaviour observed in the study, it is natural to relate its occurrence to the level of hydrostatic stress level generated by the applied load. Several concepts, based on the change in specimen design, have been previously suggested to raise the hydrostatic stress level in test specimens. The most common one, as described in ASTM F1473 [16], is to introduce sharp notches to the specimens. Indeed, study shows [6] that such sharp notches can induce brittle fracture in specimens that otherwise involve ductile deformation in the fracture process. Unfortunately, presence of sharp notches also causes crack growth from the notch tips, and thus complicates the stress distribution and hinders identification of the loading conditions for the cavitation. Because of those difficulties, specimens containing sharp notches cannot be used to identify the loading conditions for cavitation.

An alternative concept is to use dumbbell- or diabolo-shaped specimens. As mentioned earlier, this type of specimen design is to mimic the necking process in simple tensile test, as hydrostatic stress level is known to rise during the necking

process. However, the amount of cavitation developed in this type of specimens turned out to be insufficient to dominate the deformation [8]. Consequently, results from this type of specimens are also not suitable for determining the loading conditions for the cavitation.

Specimen design used in this study takes a different approach. Instead of mimicking the necking process, the necking is suppressed in the new design. As indicated by the results, the neck suppression can be achieved via shortening the gauge length. This feature raises the hydrostatic stress level by obstructing the contraction flow. Idea for the new specimen design is similar to that proposed by Gent and Lindley [10] who generated cavitation in rubber. Gent and Lindley suggested that shorter the gauge length, higher the hydrostatic stress level. However, the gauge length should not be too short. Otherwise, stress concentration at the end of the gauge section may affect stress distribution in the core region. Results presented here suggest that a gauge length of 1.8 mm is sufficiently short to introduce bulk cavitation in all HDPEs used in the study, but without the influence of stress concentration at the end of the gauge section on the stress distribution in the core region.

Identification of loading condition for cavitation

Since our short specimens do not contain sharp notches, disturbance in the test results, such as the fast load drop shown Figure 5-3(a), comes from the bulk cavitation only, not accompanied by the crack growth. Therefore, the test results can be used to identify loading conditions for cavitation. However, the level of clarity in Figure 5-3(a) for identifying the occurrence of cavitation depends on the scale used in the plot. In some cases, especially when a high sampling rate is used for data recording, change of the load drop rate can be difficult to identify in a plot like Figure 5-3(a). In this case, an alternative plot is preferred to identify the loading condition for cavitation.

Figure 5-13 compares three types of plots for results obtained from the study, all of which have a common abscissa (stroke), but different ordinate that is engineering stress (σ_{eng}), true axial stress (σ_{true}), or cross sectional diameter (D_n), normalized to have the values in terms of the fraction of the maximum engineering stress, the true axial stress at the peak load, and the initial cross sectional diameter, respectively. A vertical line is included in each figure to mark

the stroke that corresponds to the commencement of fast load drop. For clarity, the stroke value marked by the vertical line is also given explicitly in each figure.

Among the three types of plots in Figure 5-13, the σ_{true} plots give the clearest indication for the occurrence of bulk cavitation. Those plots suggest that when cavitation occurs, the σ_{true} value drops slightly for the H-series, and the trend line changes for the O-series. As such changes can be easily detected even at a high data acquisition rate the σ_{true} plot is most suitable (among the three in Figure 5-13) to identify the condition for bulk cavitation. Figure 5-13 suggests that for the 4 HDPEs used in the study, only O-2 requires a noticeably different stroke for the bulk cavitation. All of the other HDPEs have cavitation occur at a stroke around 2.15±0.05 mm.

Cavitation and post-cavitation deformation

Cavitation in semi-crystalline polymers is known to start in the inter-crystalline regions [5]. Therefore, difference in the resistance to cavitation may be useful for distinguishing mechanical properties for those regions. At this stage, however, no

tool is available to characterize molecular properties in selected regions, thus direct evidence cannot be obtained to correlate the cavitation resistance with the molecular properties. Nevertheless, work in the literature has suggested that cavitation plays a key role in disentanglement of polymer molecules, resulting in a loosened network structure [17]. In view of the very different molecular weight distribution between the two series of HDPEs, it is reasonable to believe that the H-series HDPEs have more short molecules in the inter-crystalline regions than the O-series. Based on this rationale, cavitation-induced network weakening should have a bigger impact on the former than the latter. Mechanical test results presented in this paper provide some support to this speculation, as after the cavitation O-series specimens have thicker cylindrical shell (Figure 5-5) and show better resistance to deformation (Figure 5-7) than H-series. Furthermore, post-ruptured H-series specimens show thinner cylindrical shell and have shorter stretch before the final breakup than the O-series. However, further study is needed to provide additional evidence to support the speculation.

5.7 Conclusions

Experimental testing and finite element simulation are conducted to study bulk cavitation in HDPE. Results show that a new type of cylindrical specimens can suppress neck formation in HDPE, and to raise the hydrostatic stress level to induce bulk cavitation. The new specimen geometry results in different features from the standard one in that the latter contains sharp notches, thus involving crack growth during the cavitation. Since deformation in the new specimen does not involve crack growth, the results can be used to quantify the loading condition for cavitation. However, further investigation is required to determine whether specimen dimensions used in the study are also applicable to other polymers for generating the bulk cavitation.

Using the new specimen geometry, bulk cavitation behaviour is compared between two types of HDPE that have distinctively different molecular weight and molecular weight distribution. The results show that post-cavitation behaviour is very different between the two types of HDPE, even though their necking behaviour (without cavitation) is similar. Therefore, standard short-term tensile

test that always generates necking in HDPE and is commonly used to characterize mechanical behaviour cannot reflect the cavitation resistance.

Three plots from test data are explored to identify loading conditions for the bulk cavitation, among which the plot of true axial stress versus stroke gives the clearest indication for the occurrence of bulk cavitation.

Using the new specimen design, a future study is planned to investigate the cavitation resistance of semi-crystalline polymers, or other polymers that involve necking in the standard test specimen. It is believed that results from the new type of specimens will lead to identification of key parameters that govern cavitation in polymers. Results presented in this paper show a promising possibility for achieving this objective in the near future.

Figures:

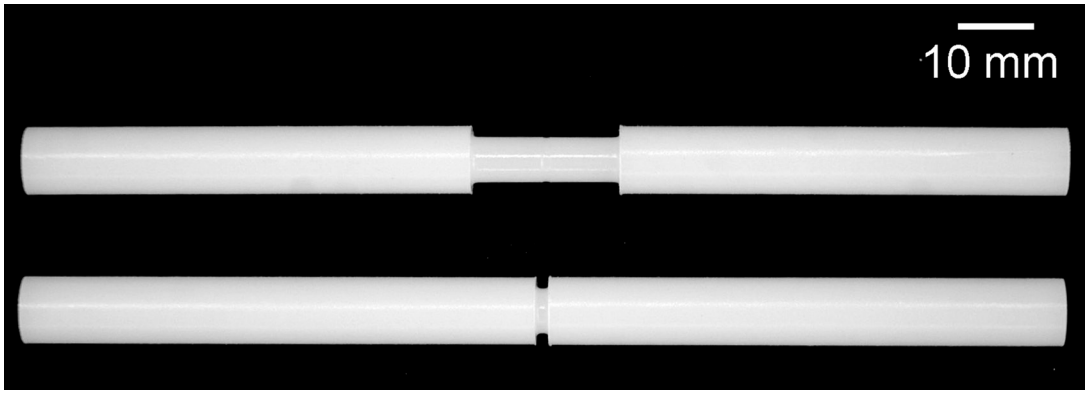

(a)

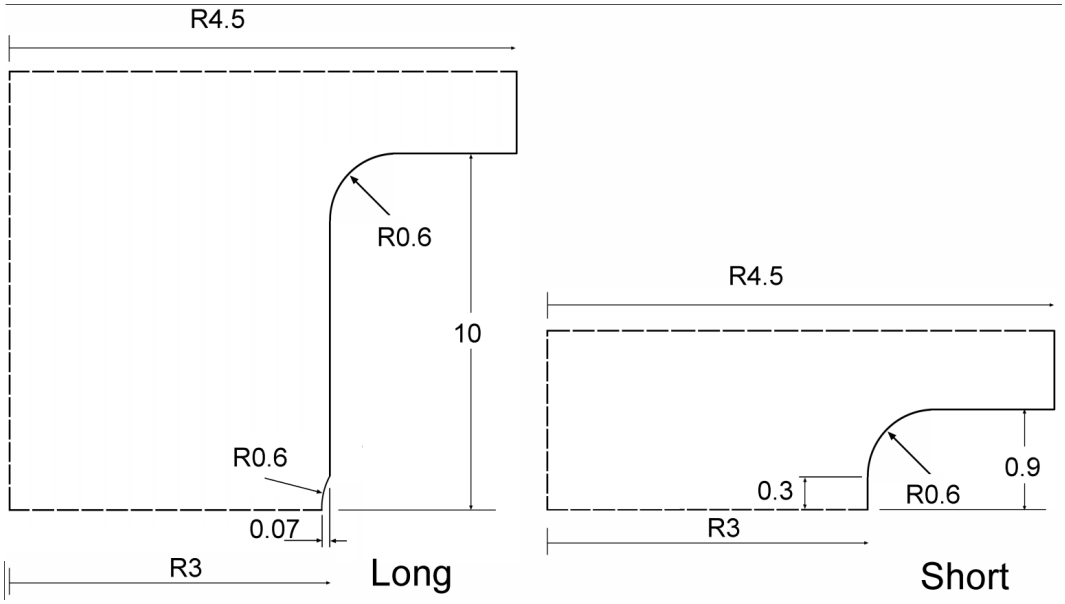

(b)

Figure 5-1 (a) Photographs of two types of cylindrical specimens used in the study: long specimen (top) and short specimen (bottom), and (b) dimensional details, in mm, for the gauge section: long specimen (left) and short specimen (right).

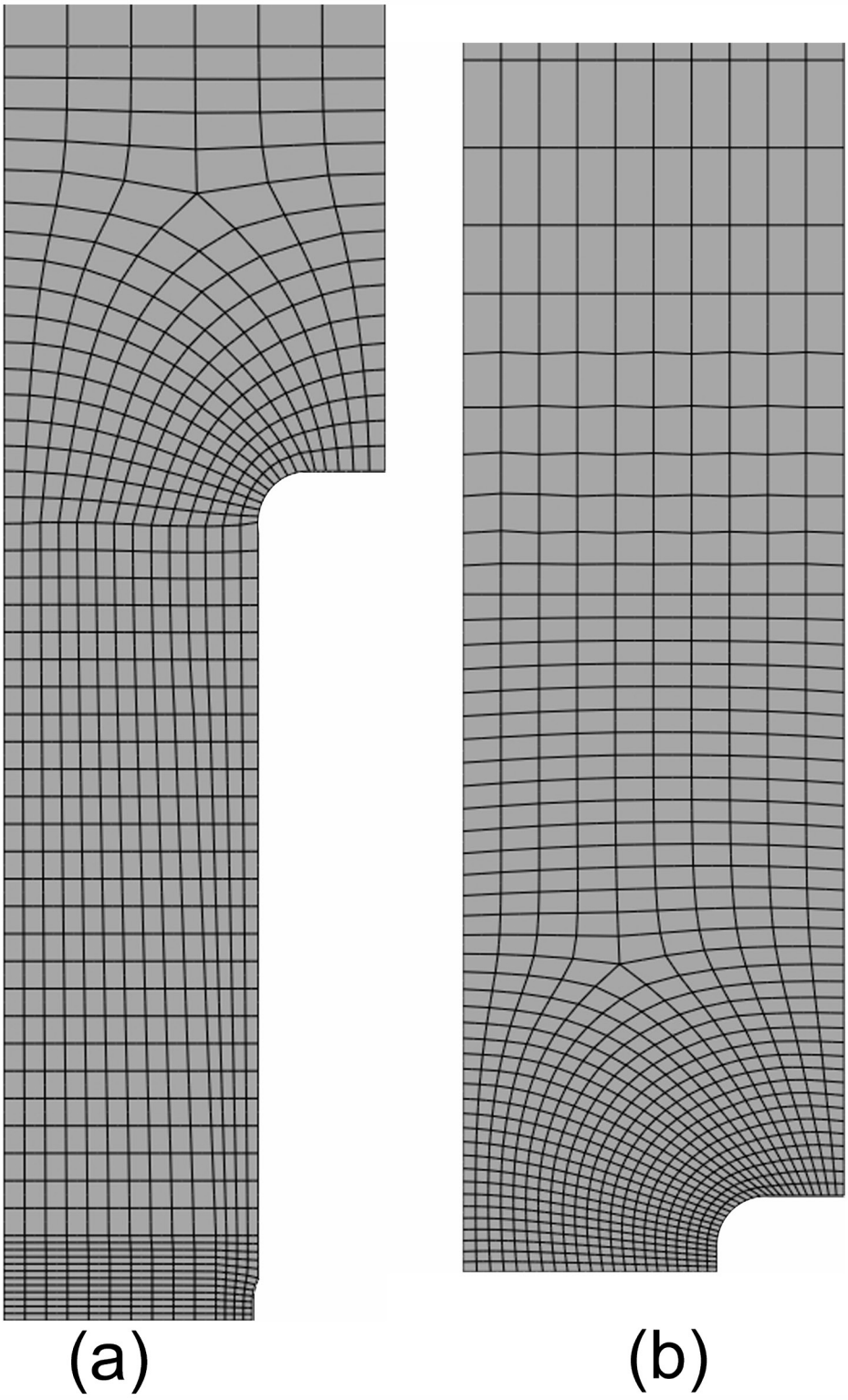

Figure 5-2 FEM models: (a) long specimen and (b) short specimen.

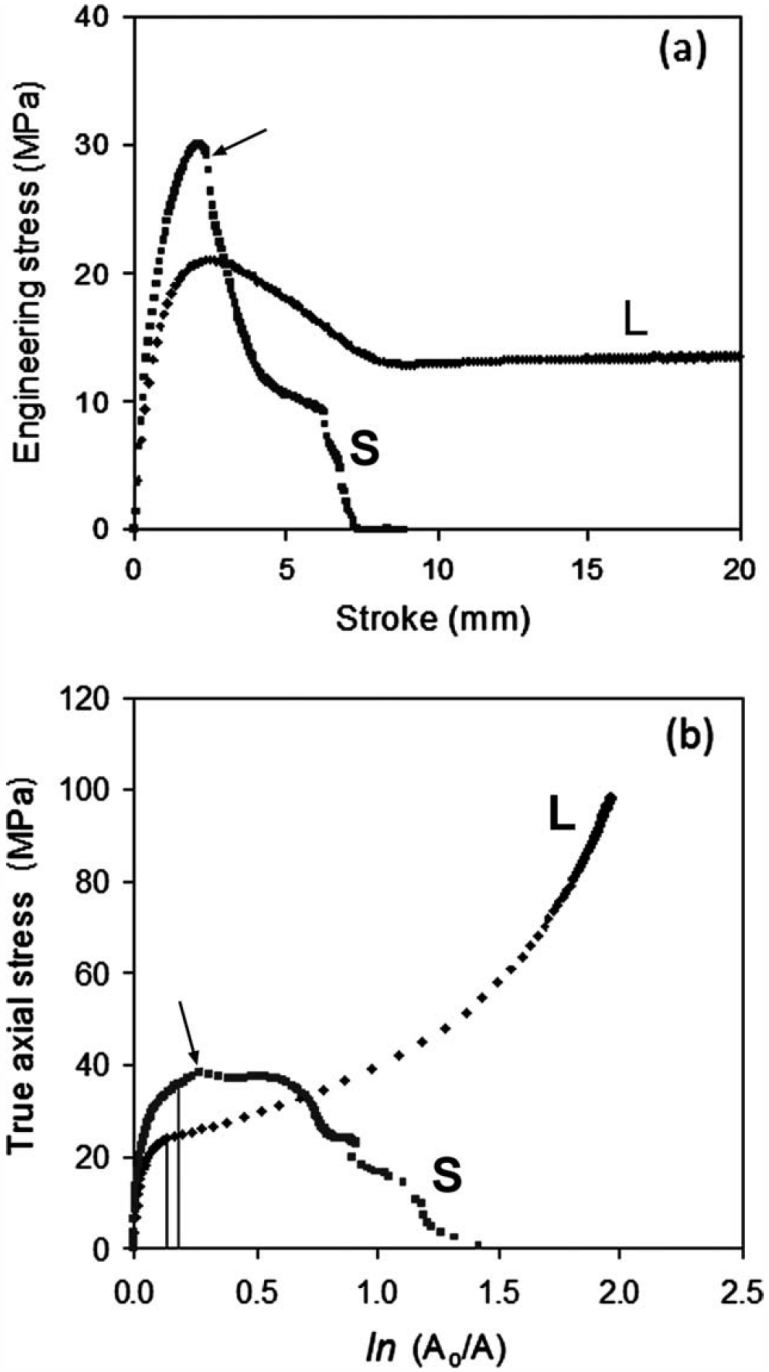

Figure 5-3 Typical test results from long (L) and short (S) specimens: (a) plots of engineering stress versus stroke, and (b) plots of true axial stress versus natural logarithmic area ratio, $ln(A_o/A)$. The vertical lines in (b) intersect with curves at the point where the peak load is. Arrow in the plots indicates the commencement of the fast load drop during the test. Note that those plots are for a H-1 specimen.

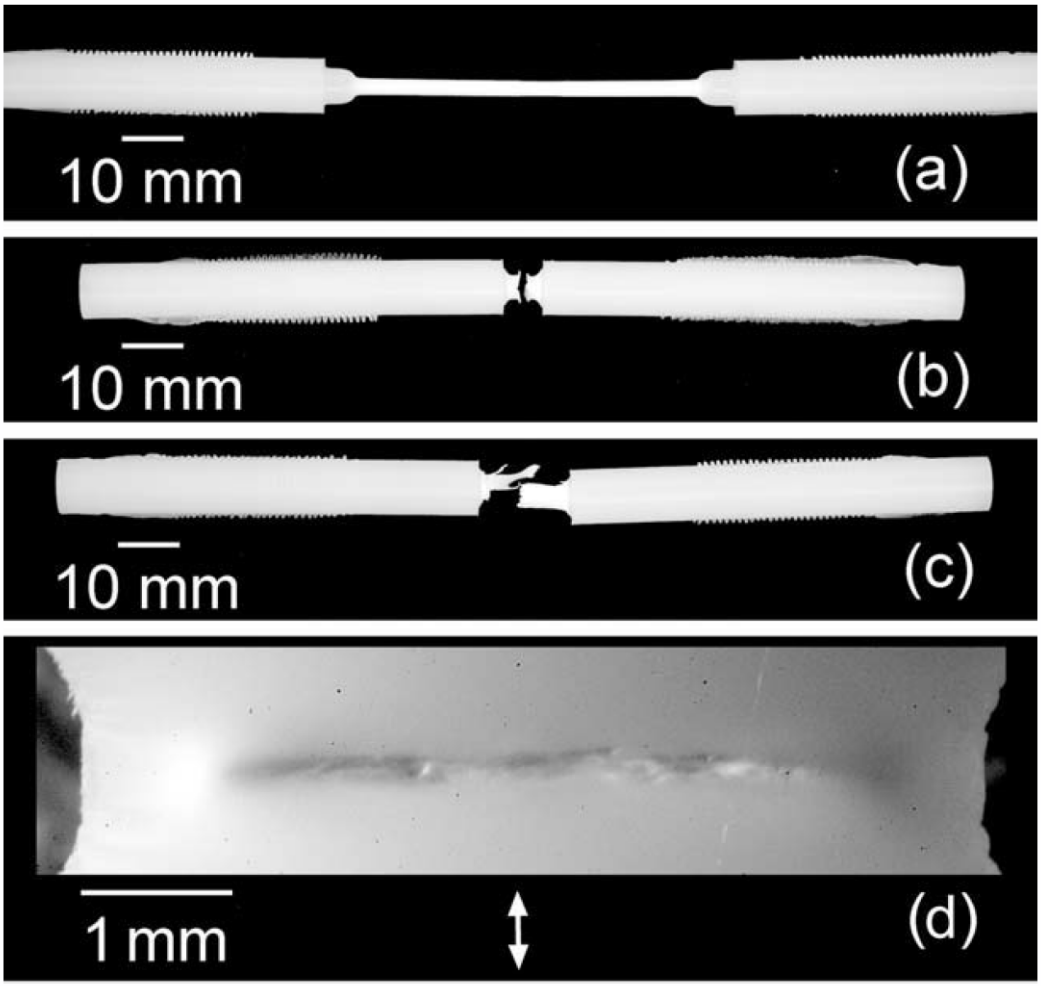

Figure 5-4 Photographs of typical specimens after the tests: (a) long specimen of both H- and O-series HDPE, (b) short specimen of H-series, (c) short specimen of O-series, and (d) cut-off view of a short H-1specimen that was unloaded immediately after the cavitation. Double arrow at the bottom of (d) indicates the loading direction.

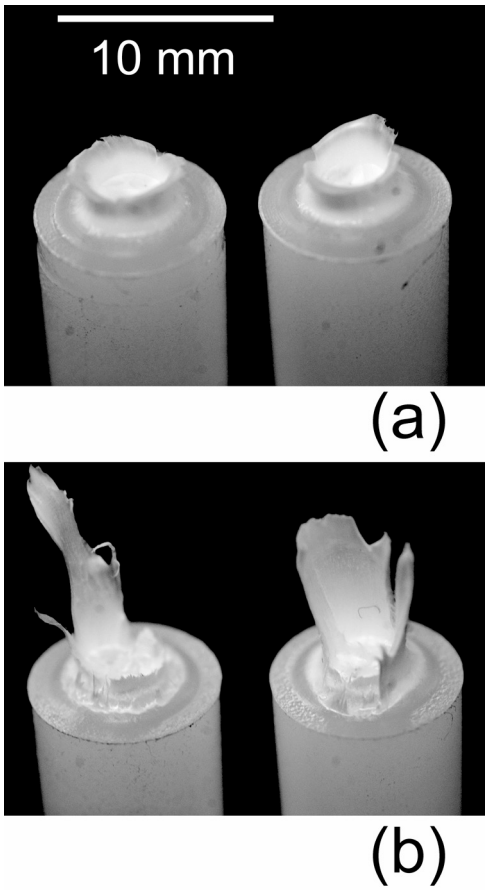

Figure 5-5 Typical residual deformation after the tests: (a) H-series, and (b) O-series. The scale is applicable to both photographs.

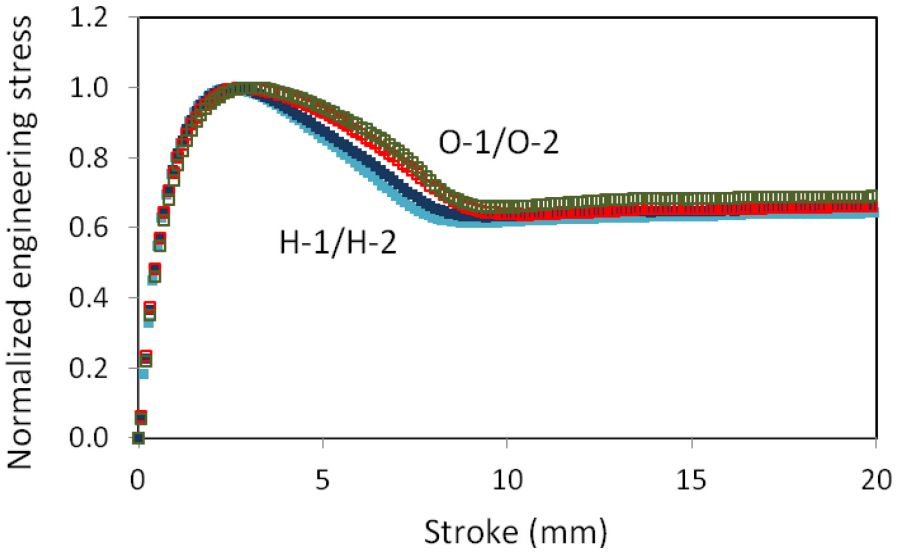

Figure 5-6 Summary of normalized engineering stress versus stoke from long specimens.

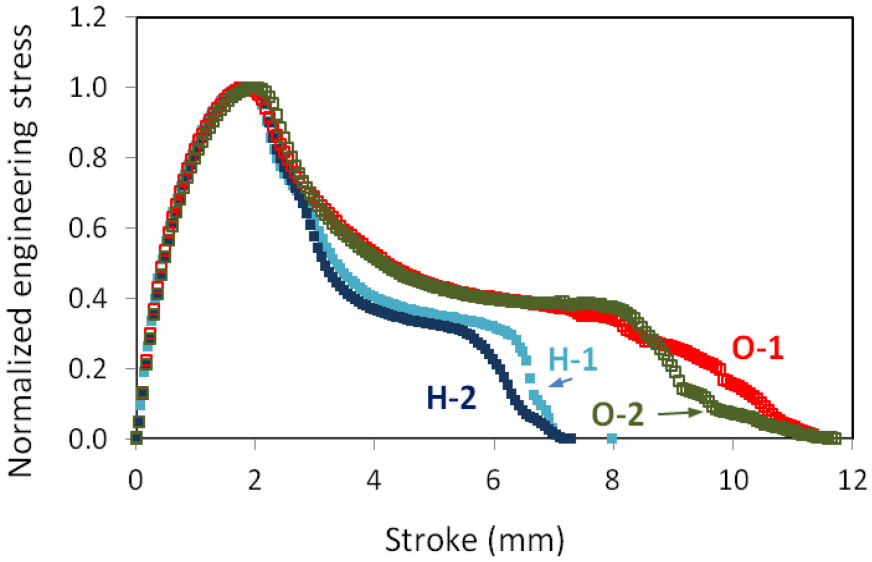

Figure 5-7 Summary of normalized engineering stress versus stroke from tensile tests of short specimens.

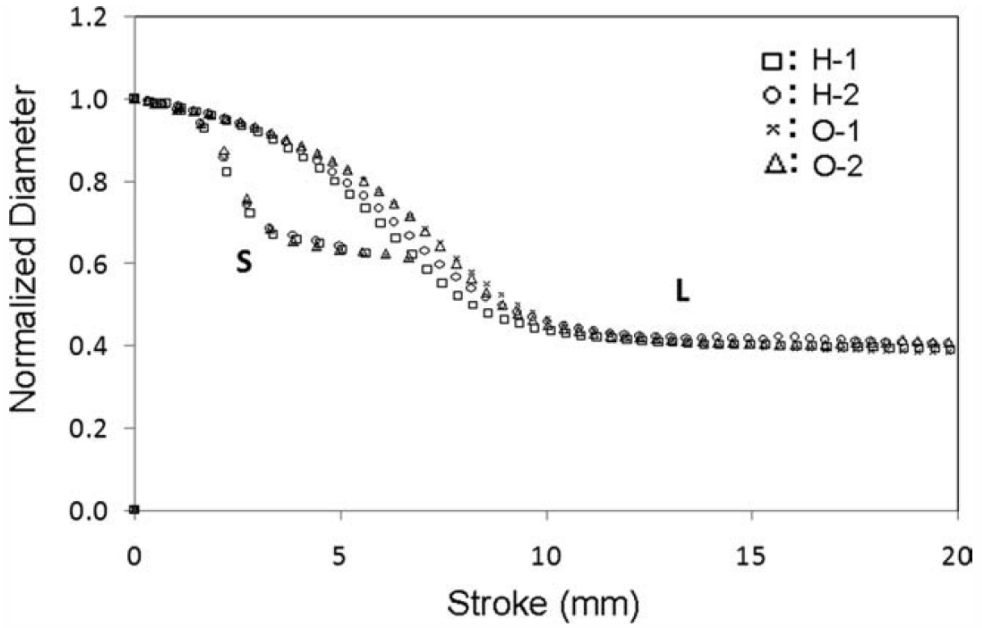

Figure 5-8 Summary of the change of cross-sectional diameter (after normalized by the original diameter) as a function of stroke for all specimens: S for short specimens and L long specimens. Open symbols are for O-series and solid ones H-series.

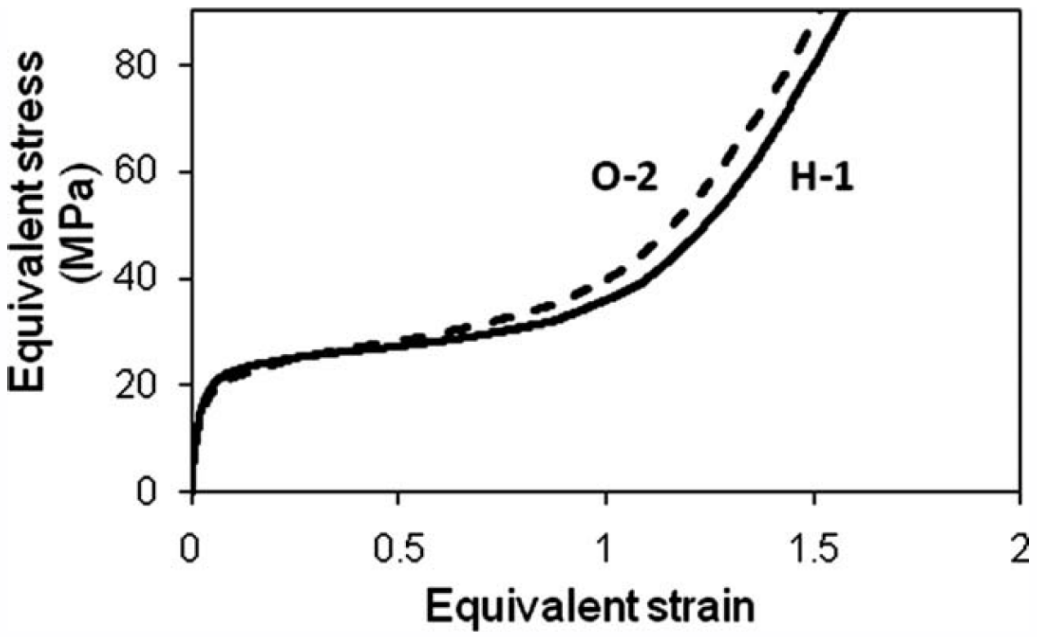

Figure 5-9 Equivalent stress-strain relatinship determined from the FEM simulation: (a) H-1 HDPE and (b) O-2 HDPE.

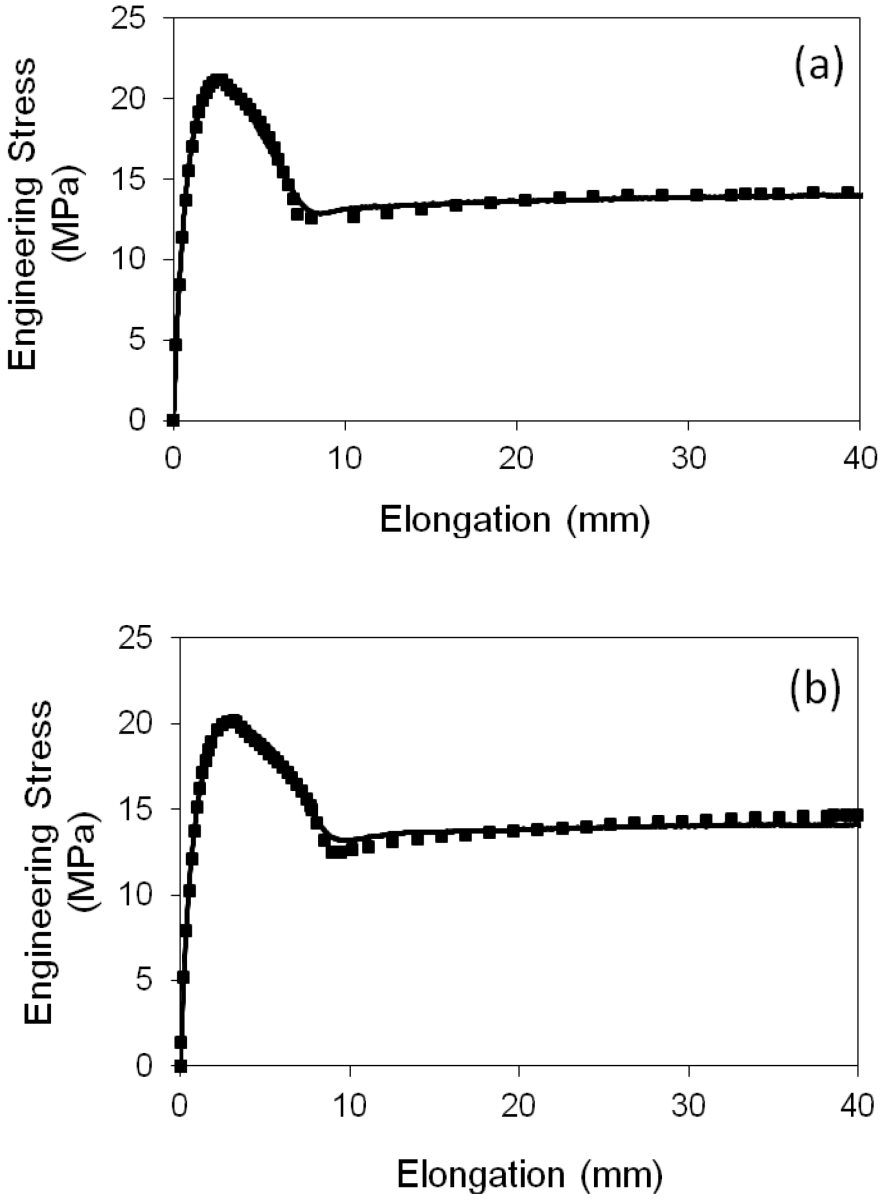

Figure 5-10 Comparison of engineering stress-elongation curve from experimental measurement (solid line) and from FEM simulation (discrete points): (a) H-1 HDPE and (b) O-2 HDPE.

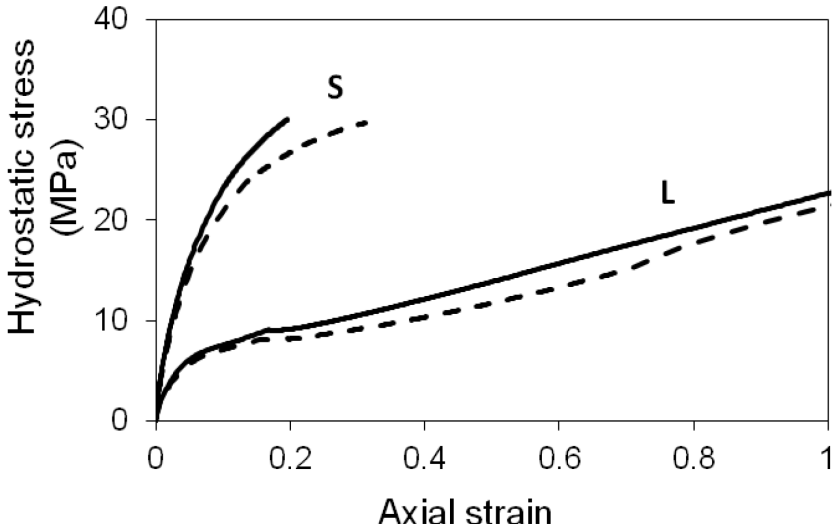

Figure 5-11 FEM results of hydrostatic stress versus axial strain: short specimen (S) and long specimen (L). Solid line respresents H-1 HDPE and dashed line O-2 HDPE.

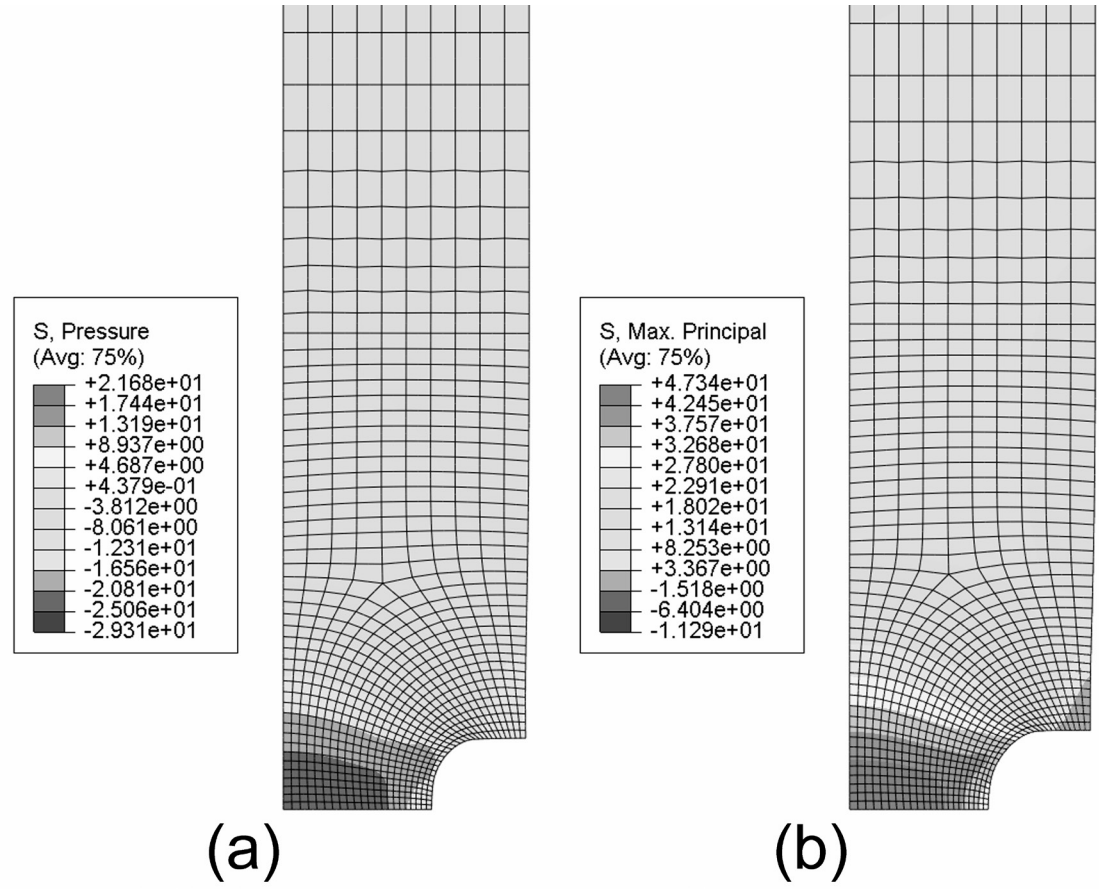

Figure 5-12 Contour plots from FEM model of short specimen based on constitutive equation for H-1 HDPE: (a) hydrostatic stress and (b) maximum principal stress.

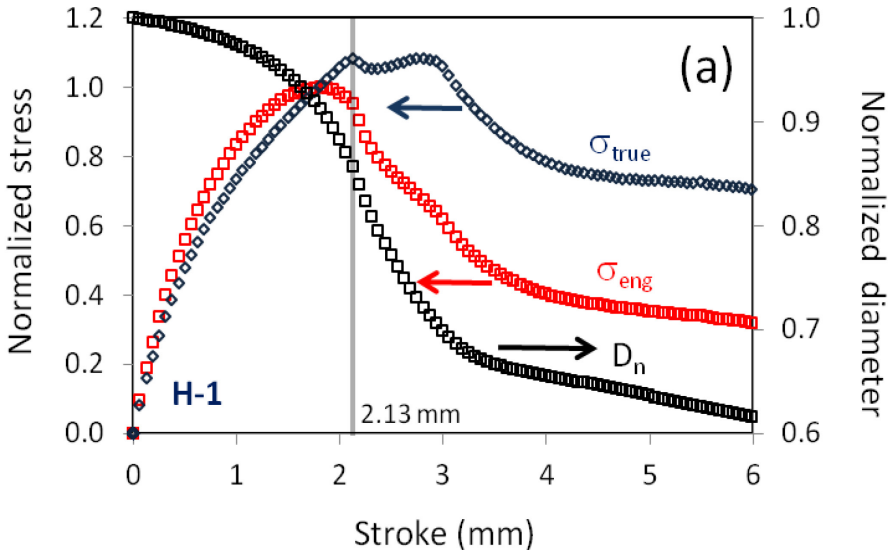
(a)
H-1
2.13 mm
σtrue
σeng
Dn
Normalized stress
Normalized diameter
Stroke (mm)
1.2
1.0
0.8
0.6
0.4
0.2
0.0
0.9
0.7
0
1
2
3
4
5
6

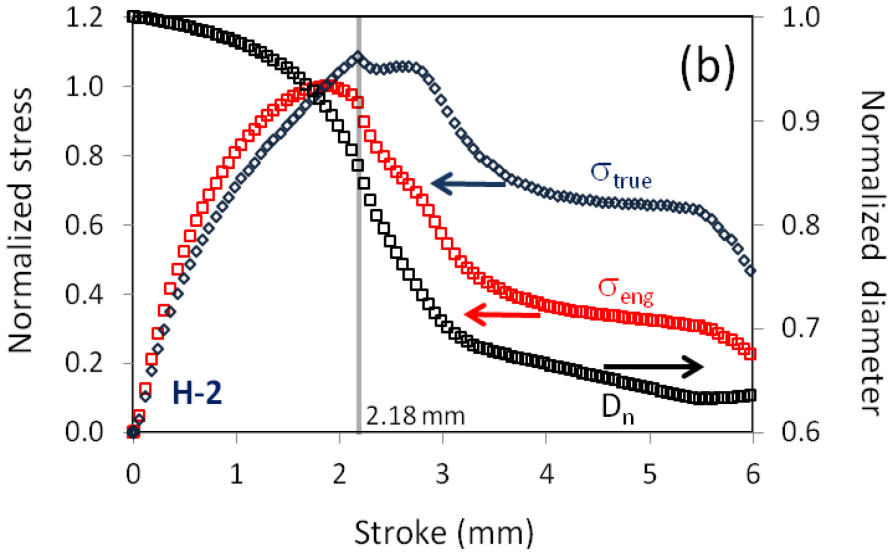
(b)
H-2
2.18 mm
σtrue
σeng
Dn
Normalized stress
Normalized diameter
Stroke (mm)
1.2
1.0
0.8
0.6
0.4
0.2
0.0
0.9
0.7
0
1
2
3
4
5
6

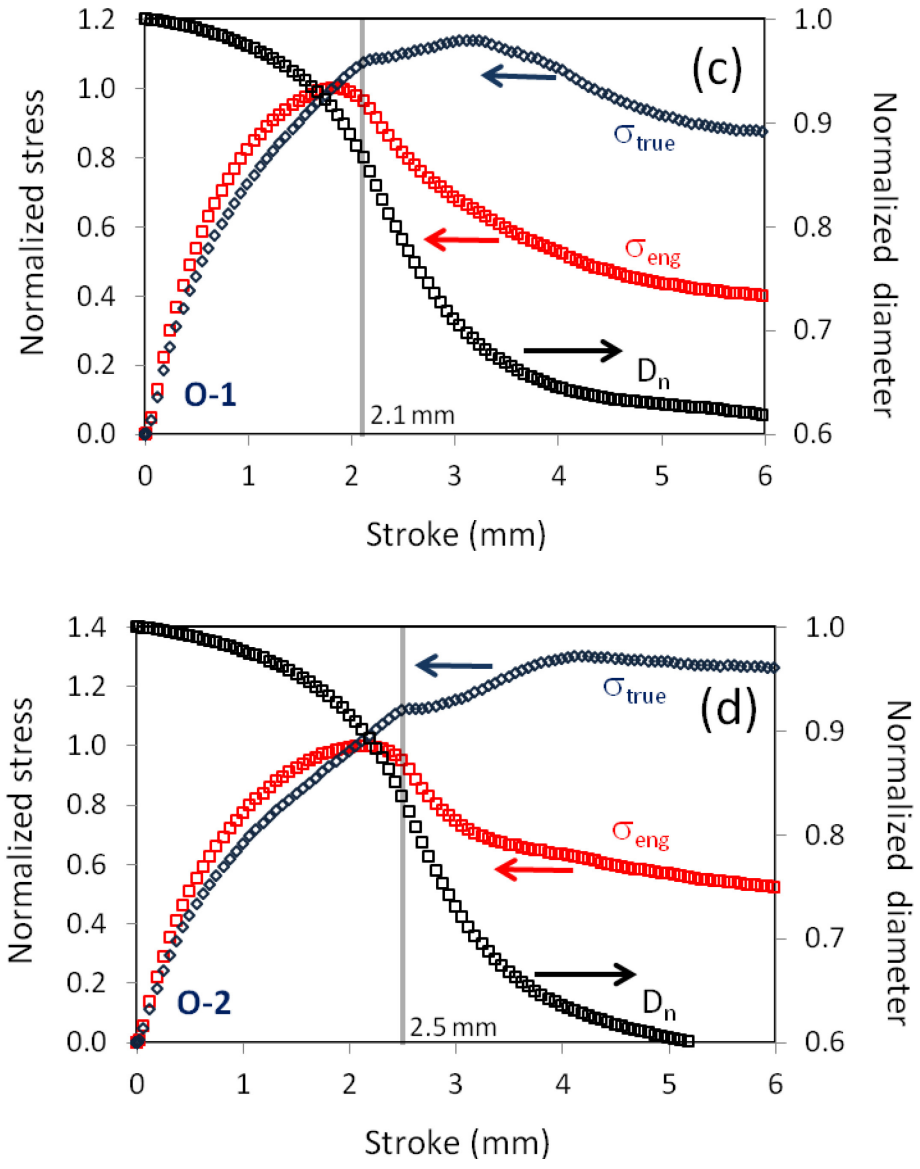

Figure 5-13 Plots of true axial stress (σ_{true}), engineering stress (σ_{eng}) and cross sectional diameter (D_n) in the stroke range for bulk cavitation: (a) H-1, (b) H-2, (c) O-1, and (d) O-2. The vertical line, at the stroke around 2 mm (the exact value is shown in each figure), gives the stroke value for the bulk cavitation.

Tables:

Table 5-1 Information of high-density polyethylene copolymers used in this study.

Resin		**Number-averaged molecular weight, Mn**	**Weight-averaged molecular weight, Mw**	**Mw/Mn**	**Branches / 1000 C**	**Density (g/cm^3)**	**Tensile strength at peak load (MPa)**
Hexene copolymer	H-1	17,100	182,000	10.6	2.5 - 2.9	0.945	21.0
	H-2	14,400	154,000	10.7	4.7 - 5.3	0.940	20.5
Octene copolymer	O-1	40,700	89,000	2.2	2.0 - 2.4	0.944	21.9
	O-2	30,400	73,100	2.4	3.4 - 4.2	0.941	20.0

Table 5-2 Constants of the power-law function for the creep deformation.

Materials	**Creep model parameters**			**Elastic properties**	
	A	***n***	***m***	**Young's Modulus (E) (MPa)**	**Poisson's Ratio (v)**
H-1	1.75×10^{-08}	4.51	-0.608	950	0.35
O-2	3.35×10^{-08}	4.51	-0.608	850	0.35

References

1. A. Galeski, *Prog. Polym. Sci.*, **28**, 1643 (2003).

2. A.S. Argon and R.E. Cohen, *Polymer*, **44**, 6013 (2003).

3. S. Castagnet, S. Girault, J.L. Gacougnolle, and P. Dang, *Polymer*, **41**, 7523 (2000).

4. X.C. Zhang, M.F. Butler, and R.E. Cameron, *Polymer*, **41**, 3797 (2000).

5. C.J.G. Plummer, A. Goldberg, and A. Ghanem, *Polymer*, **42**, 9551 (2001).

6. P.A. O'Connell, R.A. Duckett, and I.M. Ward, *Polym. Eng. Sci.*, **42**, 1493 (2002).

7. L.-Z. Liu, B.S. Hxiao, B.X. Fu, S. Ran, S. Toki, B. Chu, A.H. Tsou, and P.K. Agarwal, *Macromolecules*, **36**, 1920 (2003).

8. S. Castagnet, and Y. Deburck, Mater. Sci. Eng., **A448**, 56 (2007).

9. C. G'Sell, J.M. Hiver, and A. Dahoun, Inter. J. Solids and Structures **39**, 3857 (2002).

10. A.N. Gent, and P.B. Lindley, *Proc. R. Soc. London A*, **249**, 195 (1959).

11. A. Cristiano, A. Marcellan, R. Long, C.-Y. Hui, J. Stolk, and C. Creton, J. Polym. Sci. B: Polym. Phys. **48**, 1409 (2010).

12. M.H.B.M. Shariff, *Appl. Math. Modelling*, **17**, 430 (1993).

13. W.W. Klingbeil, and R.T. Shield, *ZAMP* (*J. Appl. Math. Phys.*), **17**, 281 (1966).

14. S. Muhammad and P.-Y.B. Jar, *J. Mater. Sci.*, **46(4)**, 1110 (2011).

15. C. G'Sell, N.A. Aly-Helal, and J.J. Jonas, *J. Mater. Sci.* **18**, 1731 (1983).

16. ASTM F1473-07, *American Society for Testing and Materials* (2007).

17. A. Pawlak, and A. Galeski, *Macromolecules*, **38**, 9688 (2005).

CHAPTER - 6

Effect of Hydrostatic Stress Level on Bulk Cavitation in Polyethylene

6.1 Introduction and Background

Many semi-crystalline polymers involve cavitation in their failure process. The most common one is crazing which consists of micro-fibrils developed within a narrow space. Size of this type of cavities is very small [1-4], and their presence causes whitening of the polymers [5-12]. Another type of cavitation, named

bulk cavitation here, involves cavities of the size that is visible by the naked eyes. Bulk cavitation is detected in polymers when subjected to the plane-strain loading [13], leading to a relatively brittle fracture even for polymers that show excellent ductility under the plane-stress loading.

Condition to generate the bulk cavitation has been studied extensively for rubber-like materials, using specimens with an extremely short gauge length [14-15]. A similar specimen design has recently been used to generate bulk cavitation in polyethylene (PE) [16]. Since the bulk cavitation occurs with a noticeable disturbance on the load-displacement curve, critical loading conditions for its occurrence can be identified. Work presented here is a follow-up study from ref. [16], using finite element (FE) modeling to investigate the role of hydrostatic stress on the generation of bulk cavities. By varying the gauge section geometry, to be long cylindrical, diabolo, or short cylindrical, the hydrostatic stress level for initiation of either necking or bulk cavitation is determined. The results are then used to understand the role of the hydrostatic stress level on the transition from ductile necking to bulk cavitation in PE.

Although bulk cavitation can also be generated using a sharp notch [17-18], the high stress gradient in front of the notch tip and the nearly simultaneous occurrence of bulk cavitation and crack growth make it difficult to use this type of specimen to quantify the hydrostatic stress level for the initiation of the bulk cavitation.

This chapter presents details of using the experimental testing and finite element modeling to establish the constitutive equation, based on which the stress state for each of the three types of gauge sectional geometry is established for understanding the influence of the stress state on the change of the deformation behavior. Since the study is concerned about transition from necking to bulk cavitation, FE modeling of diabolo and short specimens is limited to a strain range that is only slightly over the maximum load at which the necking or bulk cavitation should have been initiated.

6.2 Methodology

6.2.1 Experimental

Compression-molded PE plates of nominally 10 mm thick, provided by NOVA Chemicals with material characteristics given in Table 6-1, were used to machine cylindrical rods of 9 mm in diameter and 140 mm in length. Specimens of three different profiles in the gauge section were used in the study, all of which have axi-symmetric profile. Those for long cylindrical and short cylindrical specimens are identical to those used previously [16], with the gauge section of 6 mm in diameter, and 20 and 1.8 mm in length, thus named "long' and "short" specimens, respectively. The third one, named diabolo specimen, was inspired from the work described in ref. [19], with 5 mm for the radius of curvature and 6 mm for the minimum cross-sectional diameter in the gauge section. As to be shown here, testing the long, short, and diabolo specimens generated necking, bulk cavitation, and micro-cavitation-then-necking, respectively. Dimensions for the three types of specimens are given in Figure 6-1, along with a photograph of the specimens before the testing.

Note that raw data obtained from the mechanical testing of long and short specimens are same as those used for the previous study [16], but constitutive equation for the FE modeling conducted here is based on mechanical test results

for the corresponding specimen geometry; while in the previous study, it was assumed that the constitutive equation determined from the long specimen can be applied to the FE modeling of the short specimen. Mechanical tests for the diabolo specimens were conducted in the same condition as that used for the long and short specimens [16], that is, at a cross-head speed of 5 mm/min using a universal testing machine (QUASAR 100) at room temperature. Three identical specimens were tested for all three types of specimens to ensure the reproducibility of the test results.

6.2.2 Finite Element Analysis

Following the methodology described in a previous work [16, 20], FE analysis was conducted on axis-symmetric models of the same dimensions as the specimens used for the testing, containing CAX8R 8-node axis-symmetric elements, generated using ABAQUS standard v6.7-1. For the long specimen, the FE model has 909 elements and 2918 nodes, for the short specimen 1064 elements and 3385 nodes, and for the diabolo specimen 1241 elements and 3904 nodes. Mesh patterns of the FE models are depicted in Figure 6-2.

Since the methodology to establish the constitutive equation is described in detail in ref. [20], only a brief description is provided here. The constitutive equation consists of four expressions for the elastic-plastic deformation, each to cover a specific strain range. In addition, creep deformation is considered when the strain is larger than ε_n (strain at the peak load, as specified below). Note that exponential strain hardening, Eqn. 6.1(d), was used only to determine the constitutive equation for the long specimen, as this deformation level for diabolo and short specimens would have resulted in a significant amount of cavities to invalidate the use of continuum solid element to simulate the deformation behavior without considering the presence of the cavities.

$$\sigma(\varepsilon)=\begin{cases} \dfrac{3}{2(1+\upsilon)}E\,\varepsilon & for\ \varepsilon \le \varepsilon_y\ [21-23] \quad (a) \\ d\left[\left\{a\left(\varepsilon+b\right)\right\}^{(c-1)}-\left\{a\left(\varepsilon+b\right)\right\}^{(-c)}\right]+e & for\ \varepsilon_y \le \varepsilon \le \varepsilon_n\ [24] \quad (b) \\ \alpha k\,\varepsilon^{N} & for\ \varepsilon_n \le \varepsilon \le \varepsilon_t\ [25] \quad (c) \\ k\exp(M\varepsilon^{\beta}) & for\ \varepsilon \ge \varepsilon_t\ [26-27] \quad (d) \\ A^{-\frac{1}{n}}\left(\dot{\bar{\varepsilon}}^{cr}\right)^{\frac{1}{n}} t^{-\frac{m}{n}} & for\ \varepsilon \ge \varepsilon_n\ [28] \quad (e) \end{cases} \tag{6.1}$$

where σ is the equivalent stress in MPa, ε_y the strain for transition from linear to non-linear deformation, ε_n the strain at the peak load, ε_t the strain for the on-set of

exponential strain hardening, and $\dot{\bar{\varepsilon}}^{cr}$ the equivalent creep strain rate. Similar to that reported previously [20], the FE model has to consider the time-dependent deformation, as specified by Eqn. 6.1(e), in order to regenerate the experimentally observed variation of both engineering stress and cross-section reduction as a function of elongation.

6.3 Results and Discussion

Figure 6-3 compares typical mechanical test results from the three types of specimens in which true axial stress is depicted as a function of elongation in Figure 6-3(a), and typical post-test specimens in Figure 6-3(b). As concluded from the previous study [16], a plot of true axial stress versus elongation gives a clear indication for the onset of bulk cavitation in short specimens, by showing a sudden dip of the curve when the cavity is formed. The sudden dip was only detected in the curve from the short specimens, not from diabolo or long specimens.

As shown in Figure 6-3(b), only post-test short specimens contain a crate on the fracture surface, as the result of bulk cavitation. Deformation in diabolo and

long specimens was dominated by necking with stress whitening, suggesting that a significant amount of micro-cavities was generated during the tests.

The experimentally measured values of engineering stress and cross sectional area are presented in Figure 6-4 as line plots. Using the technique described in ref. [20], constitutive equation was determined for each type of the specimens, and was used for the corresponding FE model to mimic the deformation development during the testing. Results from the FE modelling are also presented in Figure 6-4 as discrete points. Note that in order to avoid ambiguity among the curves, due to the slight variation of the absolute values, data presented in Figure 6-4(b) have been normalized by the original cross sectional area. As mentioned earlier, data from the FE models for the short and diabolo specimens (open circles and open squares, respectively) are only up to the elongation level that is slightly over the maximum load, as the presence of cavities invalidates the use of apparent cross sectional area to determine the stress and the corresponding strain. Figure 6-4 suggests that results from the FE models show a reasonable agreement with the experimental measurements.

The constitutive equations in terms of equivalent stress-strain curves are presented in Figure 6-5. It is interesting to point out that the three curves in the figure are slightly different, with the strain hardening rate in the order of short > diabolo > long. The corresponding values for parameters in Eqn. 6.1 are summarized in Table 6-2 and compared graphically in Figure 6-6. As suggested in Figure 6-6, key parameters that cause the difference among the three curves in Figure 6-5 are b and c in Eqn. 6.1(b) and αk and N in Eqn. 6.1(c).

The variation of hydrostatic stress as a function of the equivalent strain is shown in Figure 6-7. The corresponding contour plots of the hydrostatic stress distribution at the peak load are presented in Figure 6-8. The two figures indicate that among the three types of specimens, the short specimen generates the highest hydrostatic stress level with the largest size at the peak load. The long specimen, on the other hand, has the lowest hydrostatic stress level, with very little variation detected in the entire gauge section.

To further investigate the relevance between the constitutive equations in Figure 6-5 and the hydrostatic stress level in Figure 6-7, various types of stress and strain values at the peak load were determined from the FE models, and summarized in

Table 6-3. Values in the table suggest that short and diabolo specimens have similar values for the maximum principal stress, 39.1 and 38.0 MPa, respectively, which are much higher than that for the long specimen (24.3 MPa). However, between the short and the diabolo specimens, the former has a higher hydrostatic stress level than the latter. In view that the bulk cavitation only occurs in the short specimen, it is reasonable to believe that high principal stress itself is not sufficient to generate the bulk cavitation. The high principal stress should be accompanied by a high hydrostatic stress in order to be in favor of the bulk cavitation.

As suggested by Vincent [29], stable necking occurs when the ratio of tangent modulus to axial stress is equal to 1, i.e. $\partial\sigma/\partial\varepsilon = \sigma$. To evaluate the variation of this ratio among the three types of specimens, ratio of tangent modulus to axial stress was calculated at the peak load using results from the FE models. The ratio was indeed found to be equal to 1 for the long specimen and close to 2 for the short specimen, as summarized in Figure 6-9. This suggests that the short specimen has the strongest resistance to the neck formation, and is in favor of the

bulk cavitation. For the diabolo specimen, the ratio is only slightly bigger than 1, thus necking still prevails in the deformation process.

6.4 Conclusions

Conditions for bulk cavitation and necking were investigated based on experimental testing and FE modeling. Three profiles for the gauge section were used to demonstrate the transition between two distinctively different deformation mechanisms, i.e., bulk cavitation and necking. The study investigated the effect of hydrostatic stress level on the mechanisms involved in the deformation process, and the corresponding change for the constitutive equation.

Using results from the FE modeling, the study discovered that the hydrostatic stress level generated at the peak load in the short specimen is nearly 3 times of that in the long specimen, suggesting that the high hydrostatic stress level facilitates the deformation transition from necking to bulk cavitation. The significantly different hydrostatic stress level also causes change in the

constitutive equation for the stress-strain relationship, though the change is not as significant.

Figures:

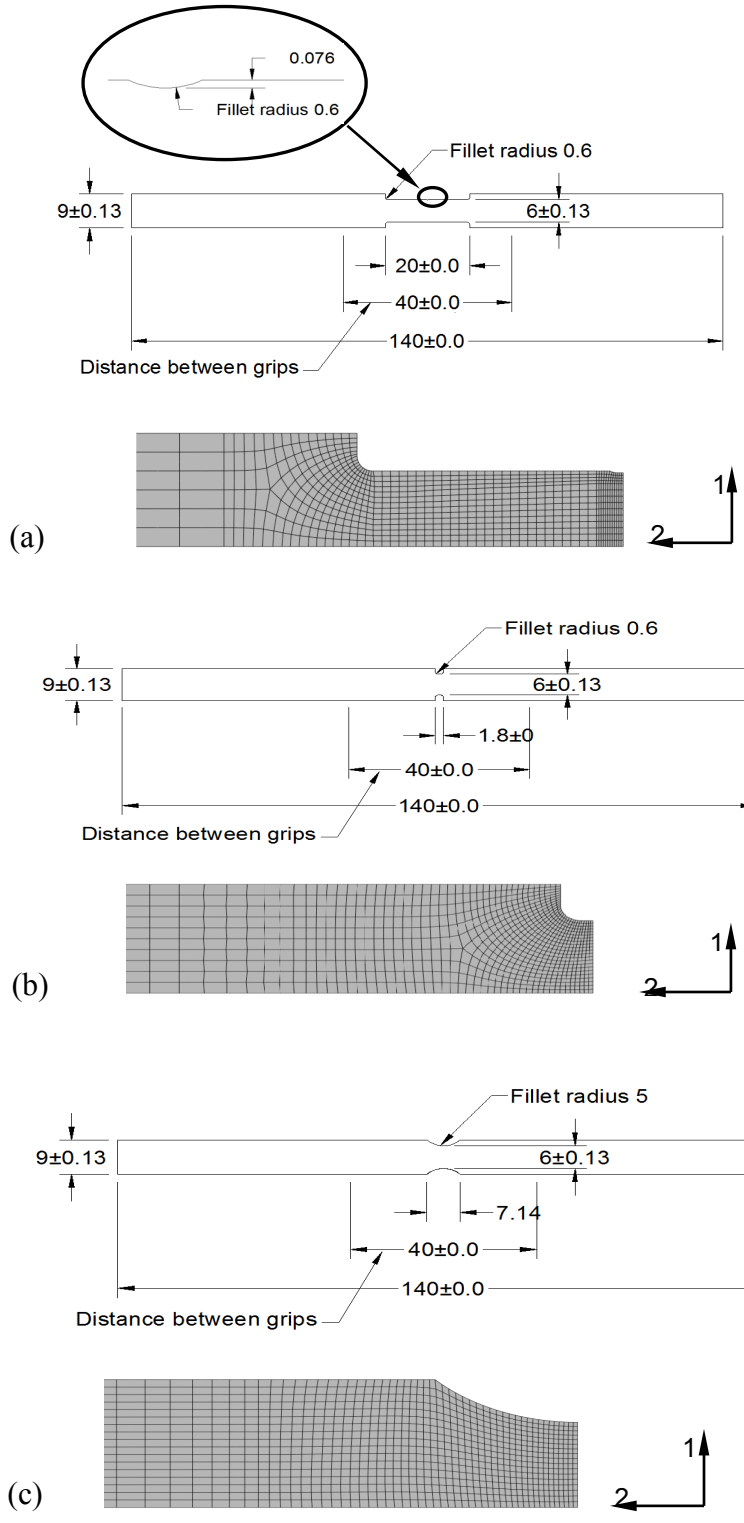

Figure 6-1 Specimen geometry and dimensions for the mechanical testing: (a) Long specimen, (b) Diabolo specimen, and (c) Short specimen.

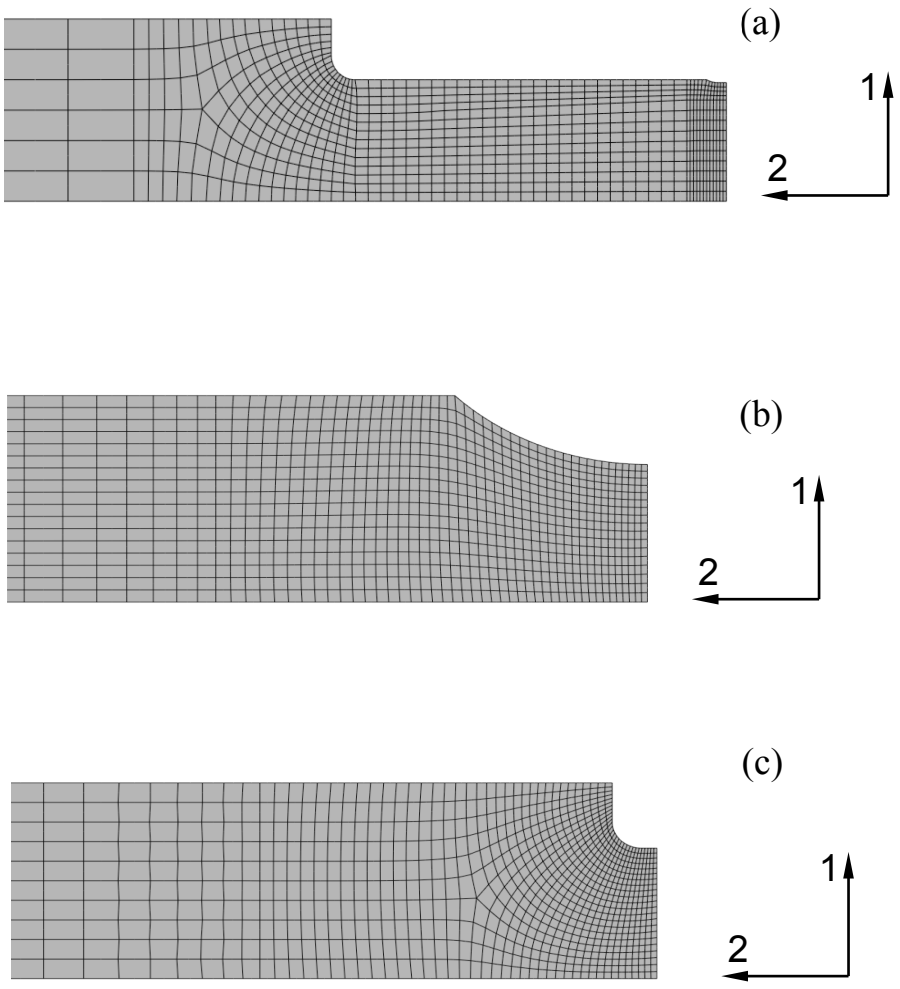

Figure 6-2 Axisymmetric models for the FE analysis: (a) long specimen, (b) diabolo specimen, and (c) short specimen, with co-ordinates 1 and 2 representing radial and axial direction, respectively.

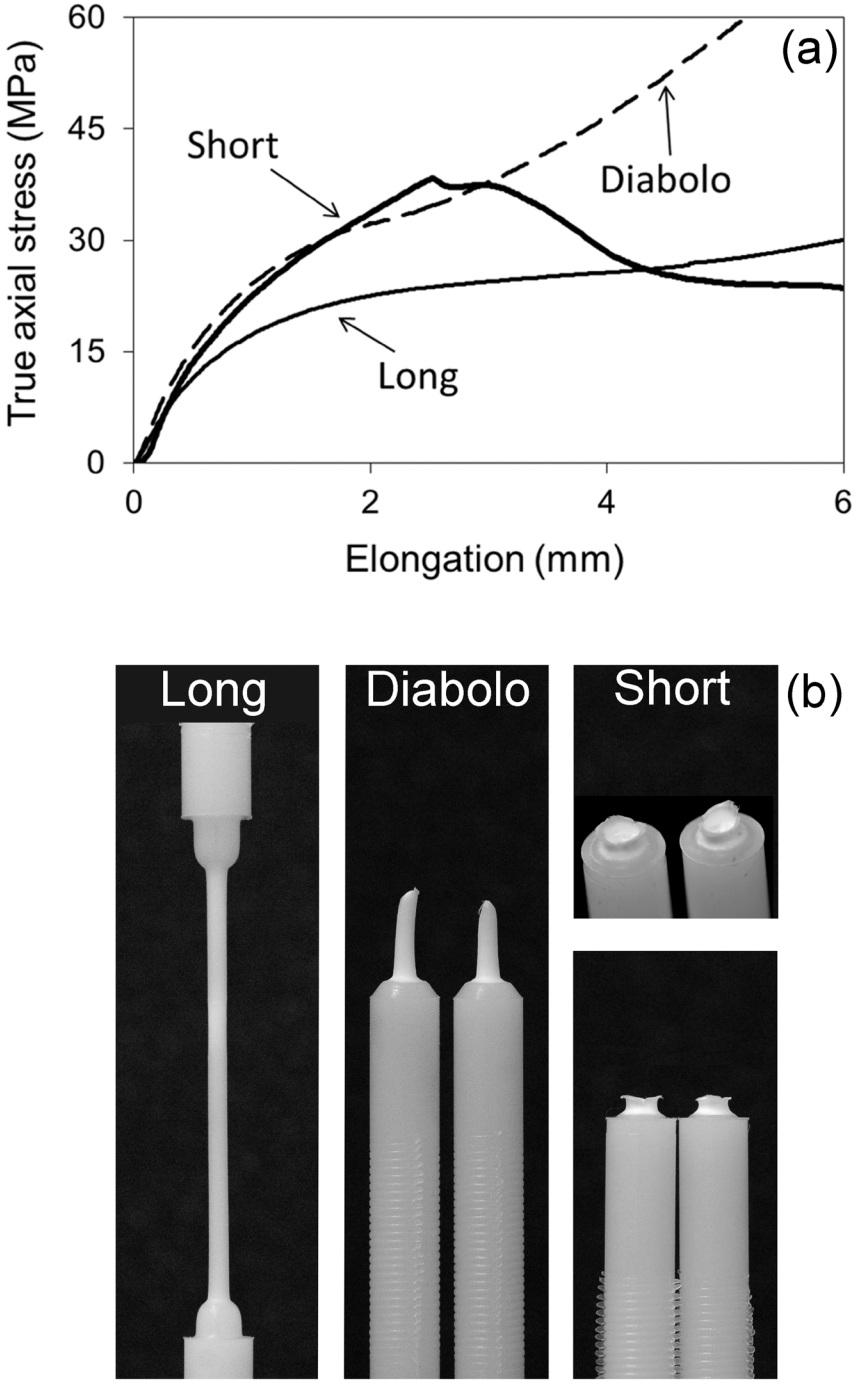

Figure 6-3 Experimental results: (a) true axial stress versus elongation, and (b) photographs of post-test specimens.

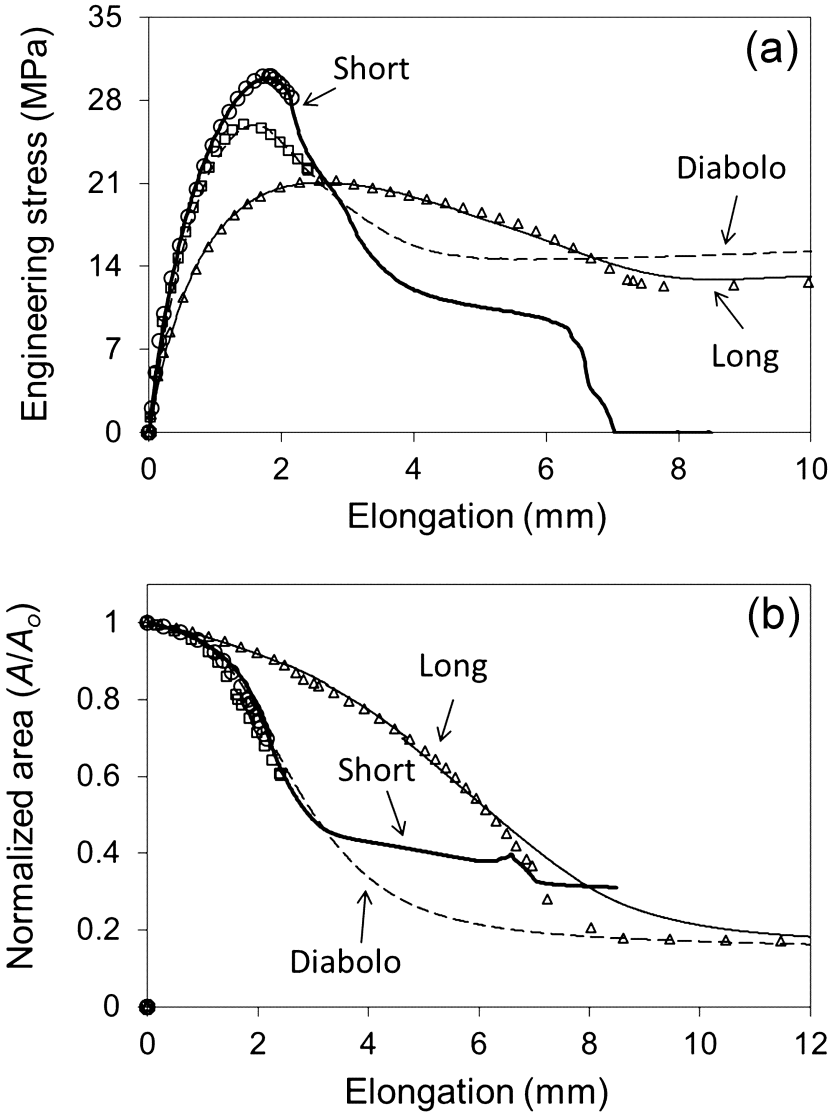

Figure 6-4 Comparison of results from experimental testing and FE simulation: (a) Plots of engineering stress versus elongation, and (b) normalized cross sectional area versus elongation. Line curves are from experimental testing and discrete points from FE simulation.

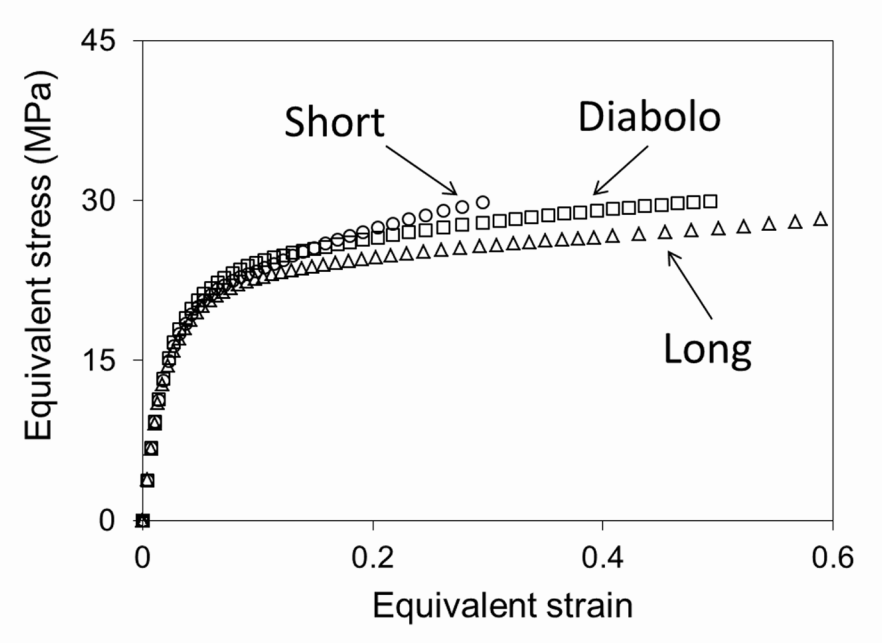

Figure 6-5 Plots of equivalent stress versus equivalent strain in the strain range for initiation of necking or cavitation.

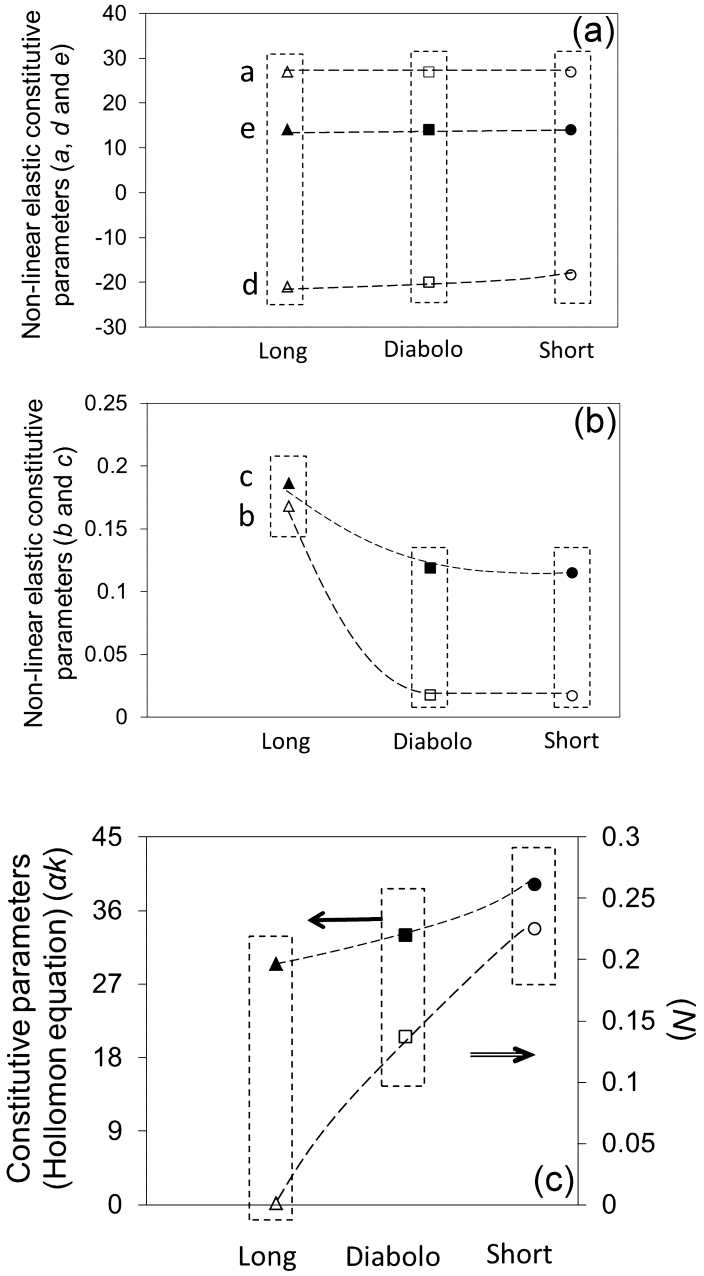

Figure 6-6 Comparison of parameter values in Eqn. 6.1 among three models: (a) non-linear equation (a, d, and e), (b) non-linear equation (b and c), and (c) Hollomon equation (αk and N). A dotted line shows the approximate trend for each parameter.

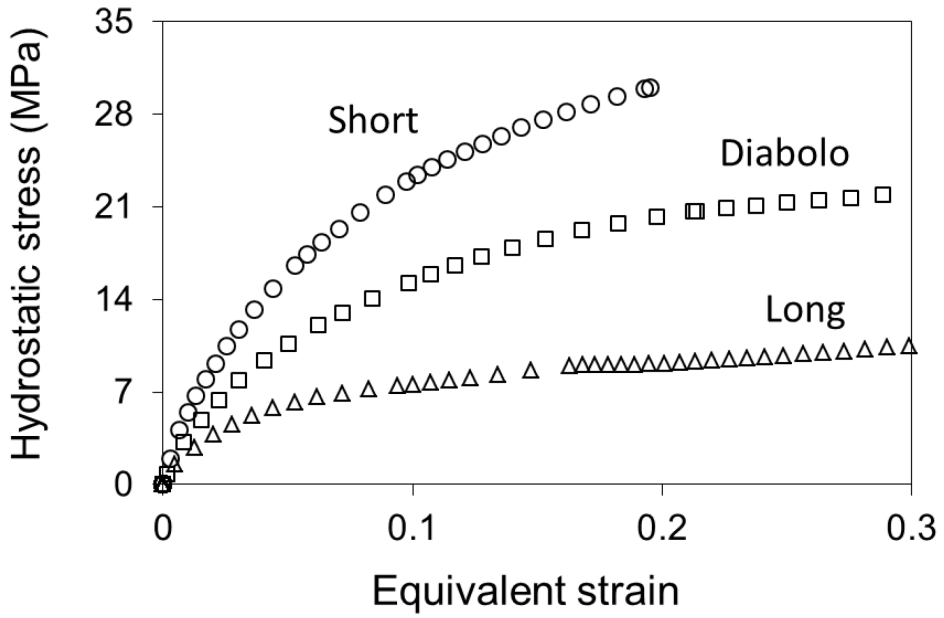

Figure 6-7 Comparison of hydrostatic stress as functions of area strain for the three types of specimens.

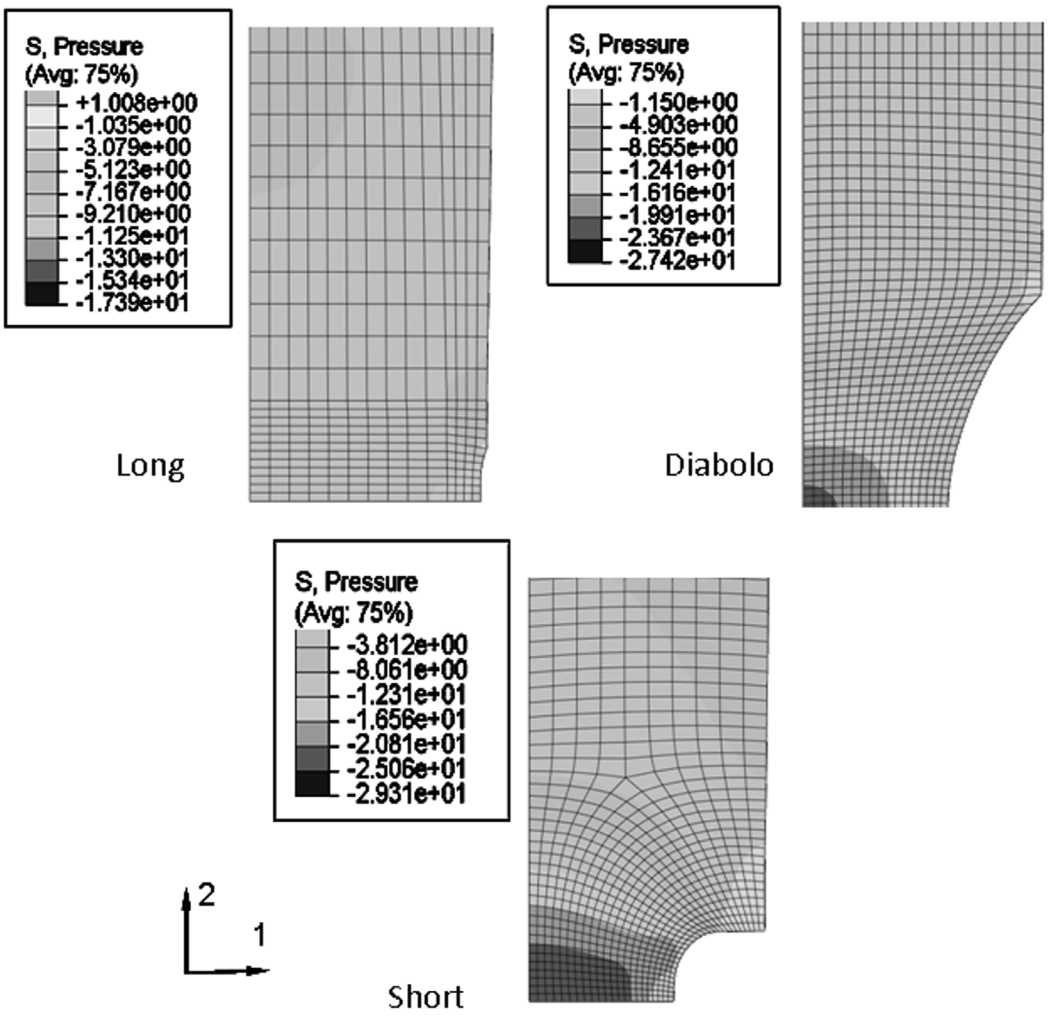

Figure 6-8 Contour plots of hydrostatic stress at peak load: (a) long, (b) diabolo, and (c) short specimens.

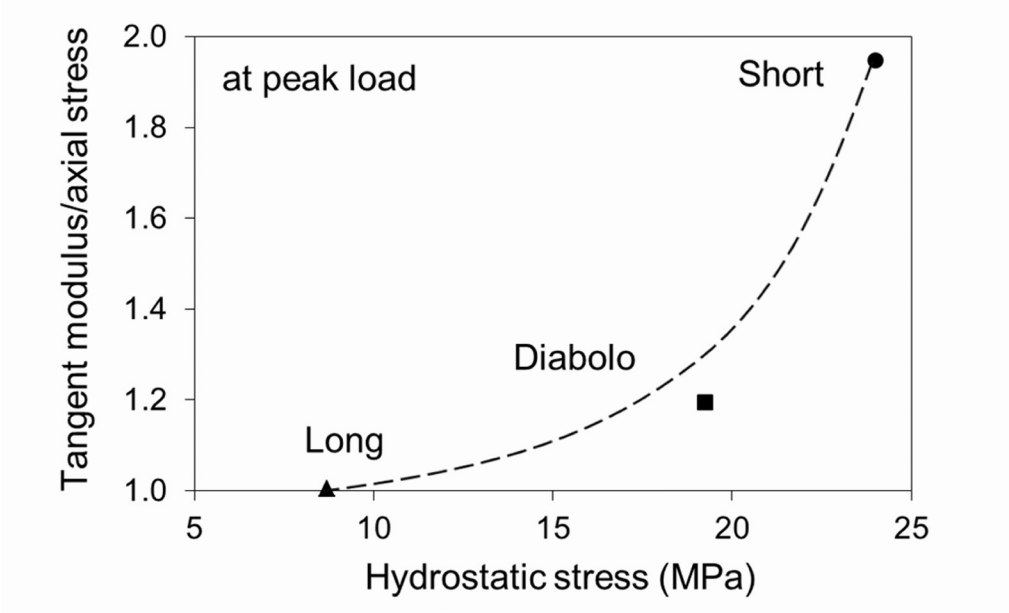

Figure 6-9 Plot of tangent modulus/axial stress versus hydrostatic stress at peak load. Dotted line shows the trend.

Tables

Table 6-1 Material characteristics for polyethylene used in this study

Material	M_w[a] (gm mol^{-1})	M_n[b] (gm mol^{-1})	M_z[c] (gm mol^{-1})	Density, ρ (gm cm^{-3})	M_w/M_n
polyethylene (hexene copolymer)	182000	17000	935000	0.945	10.6

[a] weight-average molecular weight

[b] number-average molecular weight

[c] Z-average molecular weight

Table 6-2 Values of parameters in Eqn. 6.1

FE Model		Long	Diabolo	Short
Linear elastic	E	950	950	950
	v	0.35	0.35	0.35
Non-linear elastic	a	27.0	27.0	27.0
	b	0.168	0.018	0.017
	c	0.186	0.119	0.115
	d	-21.0	-20.0	-18.3
	e	14.0	14.0	14.0
Hollomon equation for plastic deformation	αk	29.5	33.0	39.3
	N	0.113	0.137	0.225
Visco-plastic deformation	$A\times10^8$	1.75	1.75	1.75
	n	4.5	4.5	4.5
	m	-0.61	-0.61	-0.61

Table 6-3 Summary of stress and strain from three FE models at the peak load

Model designation	**Long**	**Diabolo**	**Short**
Engineering stress (MPa)	21.2	25.9	30.1
True axial stress (MPa)	24.3	38.0	39.1
True axial strain	0.151	0.168	0.117
Equivalent stress (MPa)	23.5	25.3	23.1
Equivalent strain	0.151	0.164	0.112
Hydrostatic stress (MPa)	8.69	19.2	24.0
Maximum Principal stress (MPa)	24.3	38.0	39.1

References

1. Lu X., Brown N.: Transition from ductile to slow crack growth failure in a copolymer of polyethylene. Journal of materials science, **25**, 411-416 (1990).

2. Ward A.L., Lu X., Huang Y., Brown N.: Mechanism of slow crack growth in polyethylene by an environmental stress cracking agent**.** Polymer, **32(12)**, 2172-2178 (1991).

3. Brown N., Wang X.: Direct measurement of the strain on the strain on the boundary of crazes in polyethylene. Polymer, **29(3)**, 463-466 (1988).

4. Jang B. Z., Uhlmann D. R., Vander Sande J. B.: Ductile-brittle transition in polymer. Journal of Applied Polymer Science, **29**, 3409-3420 (1984).

5. Galeski A.: Strength and toughness of crystalline polymer systems. Progress in Polymer Science, **28**, 1643-1699 (2003).

6. Argon A.S., Cohen R.E.: Toughenability of polymers. Polymer**, 44**, 6013-6032 (2003).

7. Castagnet S., Girault S., Gacougnolle J.L., Dang P.: Cavitation in strained polyvinylidene fluoride: Mechanical and X-ray experimental studies. Polymer**, 41,** 7523- 7530 (2000).

8. Cessna L. C.: Dilatometric studies of polymers undergoing high and low rate tensile deformation. Polymer Engeering & Science, **14**, 696-701 (1974).

9. Friedrich K.: Crazes and shear bands in semi-crystalline thermoplastics. in 'Crazing in Polymers'(ed.: Kausch H.H.) Advances in polymers science, 52/53, Springer, Berlin, 225-274 (1983).

10. Volynskii A. L., Shmatok Ye A., Ukolova Ye M., Arzhakova O. V., Yarsheva L.M., Lukovkin G. M., Bakeyev N.F.: Two types of crazing realized in the course of strain of polymers. Polymer science USSR, **33(5)**, 917-923 (1991).

11. Dettenmaier M., Kausch H. H.: Some observations by scanning electron microscopy on a new craze phenomenon in bisphenol-A polycarbonate. Polymer Bulletin, **3**, 571-578 (1980).

12. Dettenmaier M., Kausch H. H.: Studies on a new craze phenomenon in bisphenol-A polycarbonate: Craze initiation by stress-activated molecular disentanglement. Colloid and Polymer Science, **259**, 937-945 (1981).

13. Adianto R., Jar P.-Y. B.: Determination of plane-strain fracture toughness of polyethylene copolymer based on the concept of essential work of fracture. Polymer Engineering & Science, **50(3),** 530-535 (2010).

14. Gent A. N., Lindley P. B.: Internal rupture of bonded rubber cylinders in tension. Proceedings of the Royal Society of London. Series A, Mathematical and Physical Sciences, **249**, 195-205 (1959).

15. Cristiano A., Marcellan A., Long R., Hui C.-Y., Stolk J., Creton C.: An experimental investigation of fracture by cavitation of model elastomeric networks. Journal of Polymer Science, Part B: Polymer Physics, **48**, 1409-1422 (2010).

16. Jar P.-Y. B., Muhammad S.: Cavitation-induced rupture in high-density polyethylene copolymers. Polymer Engineering and Science**, 52**, 1005-1014 (2012).

17. Plummer C. J. G., Goldberg A., Ghanem A.: Micromechanisms of slow crack growth in polyethylene under constant tensile loading . Polymer, **42**, 9551-9564 (2001).

18. O'Connell P. A., Duckett R. A., Ward I. M.: Brittle-ductile transitions in polyethylene. Polymer Engineering and Science, **42(7)**, 1493-1508 (2002).

19. Castagnet S., Deburck Y.: Relative influence of microstructure and macroscopic triaxiality on cavitation damage in a semi-crystalline polymer. Materials Science and Engineering A, **448(1-2)**, 56-66 (2007).

20. Muhammad, S.; Jar, P.-Y. B.: Determining Constitutive Equation for Necking in Polymers based on Macro Deformation Behavior. Finite Elements in Analysis and Design (in press).

21. Neale K. W., Tugcu P. J.: Analysis of necking and neck propagation in polymeric materials. Journal of the Mechanics and Physics of Solids, **33(4)**, 323-337 (1985).

22. Tugcu P., Neale K. W.: Necking and neck propagation in polymeric materials under plane-strain tension. International Journal of Solids and Structures, **23(7)**, 1063-1085 (1987).

23. Neale K. W., Tugcu P.: Approximate methods for analysing the cold drawing of polymeric fibres and films. International Journal for Numerical Methods in Engineering, **25**, 99-112 (1988).

24. Ogden R. W.: Large deformation isotropic elasticity: On the correlation of theory and experiment for compressible rubberlike solids. Proceedings of the Royal Society A: Mathematical, Physical and Engineering Sciences, **328**, 567-583 (1972).

25. Hollomon J. H.: Tensile deformation. American Institute of Mining and Metallurgical Engineers - Transactions - Iron and Steel Division**, 162**, 268-290 (1945).

26. G'Sell C., Jonas J. J.: Determination of the plastic behaviour of solid polymers at constant true strain rate. Journal of Materials Science, **14**, 583-591 (1979).

27. Hutchinson J. W., Neale K. W.: Neck propagation. Journal of the Mechanics and Physics of Solids, **31(5)**, 405-426 (1983).

28. ABAQUS Analysis User's Manual. Version 6.7 **2007**, section 18.2.4. "Rate-dependent plasticity: creep and swelling." ABAQUS, Inc.

29. Vincent, P. I.: The necking and cold-drawing of rigid plastics. Polymer, **1**, 7-19 (1960).

CHAPTER - 7

Conclusions and Recommendations

7.1 Main Conclusions

Semi-crystalline polymers like high-density polyethylene (HDPE) is capable of generating stable necking before fracture, which is an important factor for load-bearing applications, such as pipeline and pressure vessels that are used in the distribution network for oil and gas. In addition, production of high-strength

polymer fibre involves large straining that requires the knowledge on necking to facilitate control on the production process. However, in spite of the importance of polymer necking in many industrial applications and extensive studies on its occurrence, mechanisms involved and criteria required for polymer necking are yet to be fully quantified and thus the scope of the work is widely open for researchers in this field. For polyethylene, the challenge is aggravated by the involvement of time-dependent deformation behaviour that plays a critical role in the long-term service. Several researchers realized that there are no alternatives but to use numerical simulation to avoid costly, time-consuming experiments and their associated uncertainty in the prediction accuracy. The challenge in this study is to produce constitutive relationship between stress and strain which is capable of generating deformation behaviour accurately with the ease of application to any polymer. This study addresses those challenges.

Conventionally, studies on brittle fracture of polymers have been biased by rupture accompanied with crack growth. Due to the presence of sharp notches, all studies in the literature failed to generate pure cavitation-induced rupture. Some studies that are believed to produce cavitation, cannot ascertain that crazing is not

involved. The thesis proposes a new specimen design along with test method for generating pure, bulk cavitation-induced rupture and evaluating loading condition that is responsible for the bulk cavitation.

The study identified influence of cross-sectional aspect ratio on the tri-axial stress state developed by necking in tensile specimens of polyethylene. The experimental study shows that specimens with higher aspect ratio have lower neck propagation speed and higher flow stress that invariably contribute to the higher rate of energy consumption for the neck propagation. The finite element simulation that mimics the experimental behaviour accurately, supports the observation that necking in specimens with higher aspect ratio, i.e. thinner specimens, generates higher percentage of reduction in the thickness direction but lower in the width direction, thus increasing anisotropy in the deformation behaviour. The overall capability for the deformation endurance was found to improve by reducing the specimen thickness. Results from the study indicate that plane-stress condition prevails when the aspect ratio increases, i.e. by decreasing the specimen thickness. The study concludes that finite element simulation has successfully demonstrated the influence of aspect ratio of the cross section on the

stress state in the necking process. The study also concludes that by combining experimental testing and finite element simulation, time-dependent deformation behaviour can be separated from the time-independent counterpart, which is almost impossible to achieve based on the techniques that rely purely on the experimental measurements.

An approach, based on mechanical testing and finite element modeling, is presented to establish the constitutive relationship for polymers when localization of strain evolves under tensile loading. A phenomenological model using a piecewise iteration technique has been developed that is extremely easy to apply, but exceptionally powerful to capture different deformation behaviour with outstanding accuracy, especially with the involvement of the visco-plastic deformation.

The above technique was further explored to establish proper constitutive model and demonstrated the inevitability of the existence of visco-plastic behaviour of HDPE. Standard numerical implementation (based on a piecewise progressive iteration technique) of the developed constitutive model within the frame work of finite element analysis, demonstrates the necking that occurs spontaneously

during the uni-axial extension. Highly non-linear visco-plastic material model is based on two pieces of physical evidence: (a) experimental engineering stress and (b) cross-section reduction as functions of elongation. A few approaches are available in the literature, which use both micro and macroscopic models to simulate large deformations of different polymers. The current method has the advantage in that it is capable of achieving better accuracy with less complexity. The scheme is easy and accurate enough like the other phenomenological models but its robustness is comparable to the theoretical models. In this study, the method has been successfully applied to specimens of different geometries and loading rates with reasonable accuracy.

In this thesis, enumeration of rate-dependent deformation behavior of HDPE in large deformation, especially when necking occurs, is presented. The current study investigates the effect of visco-plastic deformation on the strain rate variation during the uni-axial tensile test. The results show that at a given crosshead speed, limit of the strain rate range decreases significantly (about 60%) with the decrease of cross sectional aspect ratio from 4.3 to 1.3 (i.e., specimen thickness increases from 3 to 10 mm); while by decreasing the crosshead speed

from 100 to 5 mm/min, significant deviation in the nominal stress-strain and true stress-strain curves during the neck formation phase is observed. Also as a consequence of decreasing the crosshead speed, effect of cross sectional aspect ratio on the final necked dimension, i.e., anisotropy during the necking, decreases. The results reveal that the range of the strain rate involved during the necking process remains the same after the visco-plastic strain is removed from the calculation. Therefore, it is concluded that for the uni-axial tensile test, the strain rate determined directly from the experimental measurement gives a reasonable estimation of the strain rate range for the elastic-plastic deformation.

A new specimen design is proposed with which, bulk cavitation is successfully generated in HDPE. This method is different from that in literature in that the latter must use sharp notches to generate bulk cavitation. Since no sharp notch is used in the new specimen design, its deformation does not involve crack growth, and therefore, is purely governed by the cavitation-induced rupture process. Bulk cavitation is investigated in two types of HDPE that have different molecular weight distribution characteristics. Test results indicate that bulk cavitation can be introduced in both types of HDPE and that the loading level for the bulk

cavitation is most easily identified using plots of true axial stress versus stroke, which shows a clear, easily recognizable load drop. It is found that the whitening starts at the peak load, which means cavity nucleation starts and specimen collapses just after the peak load when the nucleated cavities coalesces with each other. The main difference between the two types of HDPE used in the study is during the post-cavitation stretch. The study also investigates necking behaviour of the HDPEs, from which constitutive equations are established for finite element modeling (FEM) of the deformation before the bulk cavitation. The FEM results indicate that hydrostatic stress level for bulk cavitation is about three times of that for necking at the same strain level. The short specimen was also used to quantify the level of hydrostatic stress required for the initiation of bulk cavitation. As a result, the new specimen design has bulk cavitation replace necking as the dominant deformation mechanism in HDPE.

The thesis work also dealt with the micro-mechanical deformation mechanism, i.e., effect of the gauge section geometry on the nucleation of cavity in HDPE under uniaxial tension. In this study three different designs of specimen gauge section geometry have been used to demonstrate explicitly a transition in failure

behavior from necking (shear yielding) to cavitation. A combined experimental and numerical study has been presented to establish the transition from necking to cavitation without the presence of any sharp notch. The study captured the macroscopic stress-field at the onset of cavity nucleation and identified that negative pressure (hydrostatic tensile stress, $\sigma_H \geq 24$ MPa) is most favourably responsible for the generation of cavity. Transition from necking (shear yielding) to cavitation-induced rupture was also found to be influenced by another factor: ratio of tangent modulus to axial stress at the onset of the damage generation. Value of this ratio for bulk cavitation is almost double of that for neck initiation. Condition for the cavity initiation has been explained in terms of the tie molecules and entanglement of free molecules that carry the load during the uniaxial extension. Dependence of parameters in the constitutive model on the evolved hydrostatic stress has been presented to demonstrate how specimen geometry affects the deformation behavior during the large deformation.

Overall the thesis has dealt with various subject matters that have not been explored in the past. It is my belief that the results of this study would be recognized as a milestone in the relevant research field.

7.2 Recommendations

Chapter 5 presents a new type of cylindrical specimens that can suppress neck formation in HDPE, and raise hydrostatic stress level to induce bulk cavitation. Standard specimen used to produce brittle fracture contains sharp notches, thus involving crack growth during the cavitation. Since deformation in the new specimen does not involve crack growth, the results can be used to quantify the loading condition for the cavitation. Chapter 6 explores the effect of hydrostatic stress level on the mechanism that dominates the deformation process. Hydrostatic stress level generated at the peak load in the short specimen is nearly 3 times of that in the long specimen, suggesting that the high hydrostatic stress level facilitates the transition from necking to bulk cavitation. The short specimen was also found to generate the stress triaxiality of around 1 at the peak load, which quantifies the level of hydrostatic stress required for the initiation of bulk cavitation. Thus, if somehow the hydrostatic stress level in the new specimen can be decreased, cavitation can be suppressed to have a transition from brittle to ductile. Using the constitutive model described in Chapters 3 and 4, the

simulation results indicate that with the decrease of the cross-head speed the hydrostatic stress evolved at the onset neck propagation decreases. Thus decreasing the loading rate or increasing the temperature of the test environment encourages the transition from brittle to ductile. I also believe that with further decrease of the loading rate or increase of temperature, another transition from ductile to brittle can be found. It has been reported in the literature that polyethylene exhibit brittle fracture when subjected to a low stress level over a long period of time. This failure mechanism has been a big problem for pipeline industries for decades. This failure behaviour is also known as Slow Crack Growth (SCG) in the pipe industry. Capturing this material behavior takes a tremendously long period of time (more than a year) per ASTM D 1598 (Standard test method for time-to-failure of plastic pipe under constant internal pressure). It is my belief that using the approach described in current thesis mechanical properties of SCG can be obtained in a much shorter duration. However, further study is needed to develop the details of the test methodology.

References

ABAQUS Analysis User's Manual. "Rate-dependent plasticity: creep and swelling", Section 18.2.4, ABAQUS manual version 6.7 (2007) ABAQUS, Inc.

Adianto R., Jar P.-Y. B. (2010). Determination of plane-strain fracture toughness of polyethylene copolymer based on the concept of essential work of fracture, Polymer Engineering & Science, 50, 3, 530.

Argon A. S., Cohen R. E. (2003). Toughenability of polymers, Polymer, 44, 6013.

Armstrong R. W., Walley S. M. (2008). High strain rate properties of metals and alloys, Int. Mater. Rev., 53, 3, 105.

ASTM F1473-07, *American Society for Testing and Materials* (2007).

Automotive Engineering International. April 2007, SAE International, p. 108.

Bao, S. P., Tjong, S. C. (2008). Mechanical behaviors of polypropylene/carbon nanotube nanocomposites: The effects of loading rate and temperature, Mater. Sci. Eng. A, 485, 508.

Bardenhagen S. G., Stout M. G., Gray G. T. (1997). Three-dimensional, finite deformation, viscoplastic constitutive models for polymeric materials, Mech. Mater, 25, 4, 235.

Bianchi G., Sorrentino R. (2007). Electronic filter simulation and design. McGraw-Hill Companies, New York.

Boyce M. C., Arruda E. M. (1990). An experimental and analytical investigation of the large strain compressive and tensile response of glassy polymers, Polym. Eng. Sci., 30, 1288.

Boyce M. C., Parks D. M., Argon A. S. (1988). Large inelastic deformation of polymers, Part I: Rate dependent constitutive model, Mech. Mater., 7, 1, 15.

Boyce M. C., Weber G. G., Parks D. M. (1989). On the kinematics of finite strain plasticity, J. Mech. Phys. of Solids, 37, 5, 647.

Brereton M. G., Klein P. G. (1988). Analysis of the rubber elasticity of polyethylene networks based on the slip link model of S. F. Edwards et al., Polymer, 29, 970.

Bridgman P. W. (1944). Stress distribution at neck of tension specimen, Trans. Amer. Soc. Met., 32, 553.

Brown N., Wang X. (1988). Direct measurement of the strain on the strain on the boundary of crazes in polyethylene, Polymer, 29, 3, 463.

Buckley C, Costas M. (2004). Neck propagation in polyethylene, J. Polym. Sci. Part B: Polym. Phys., 42, 2081.

Butterworth S. (1930). On the theory of filter amplifiers, Experimental wireless and the wireless engineer, 7, 536.

Castagnet S., Deburck Y. (2007). Relative influence of microstructure and macroscopic triaxiality on cavitation damage in a semi-crystalline polymer, Materials Science and Engineering A, 448, 2, 56.

Castagnet S., Girault S., Gacougnolle J. L., Dang P. (2000). Cavitation in strained polyvinylidene fluoride: Mechanical and X-ray experimental studies, Polymer, 41, 7523.

Cessna L. C. (1974). Dilatometric studies of polymers undergoing high and low rate tensile deformation, Polymer Engeering & Science, 14, 696.

Coleman B. D. (1983). Necking and drawing in polymeric fibers under tension, Arch. Rat. Mech. Analy., 83, 2, 115.

Cristiano A., Marcellan A., Long R., Hui C.-Y., Stolk J., Creton C. (2010). An experimental investigation of fracture by cavitation of model elastomeric networks, Journal of Polymer Science, Part B: Polymer Physics, 48, 1409.

Dettenmaier M., Kausch H. H. (1980). Some observations by scanning electron microscopy on a new craze phenomenon in bisphenol-A polycarbonate, Polymer Bulletin, 3, 571.

Dettenmaier M., Kausch H. H. (1981). Studies on a new craze phenomenon in bisphenol-A polycarbonate: Craze initiation by stress-activated molecular disentanglement, Colloid and Polymer Science, 259, 937.

Drozdov A. D., Christiansen J. (2003). Nonlinear time-dependent response of isotactic polypropylene, J. Rheol., 47, 3, 595.

Duan Y., Saigal A., Greif R., Zimmerman N. A. (2001). A uniform phenomenological constitutive model for glassy and semicrystalline polymers, Polym. Eng. Sci., 41, 8, 1322.

Edwards S. F., Vilgis Th. (1986). The effect of entanglements in rubber elasticity, Polymer, 27, 4, 483.

Fager L. O., Bassani J. L. (1986). Plane strain neck propagation, Int. J. Solids Structures, 22, 1243.

Fang Q. Z., Wang T. J., Beom H. G., Zhao H. P. (2009). Rate-independent large deformation behavior of PC/ABS, Polymer, 50, 296.

Friedrich K. (1983). Crazes and shear bands in semi-crystalline thermoplastics, Advances in polymers science, 52/53, 225.

Galeski A. (2003). Strength and toughness of crystalline polymer systems, Prog. Polym. Sci., 28, 12, 1643.

Dean G. D., McCartney L. N., Mera R., Urquhart J. M. (2011). Modeling nonlinear viscoelasticity in polymers for design using finite element analysis, Polym. Eng. Sci., 51, 2210.

Gent A. N., Lindley P. B. (1959). Internal rupture of bonded rubber cylinders in tension, Proceedings of the Royal Society of London, Series A, Mathematical and Physical Sciences, 249, 195.

G'Sell C., Aly-Helal N. A., Jonas J. J. (1983). Effect of stress triaxiality on neck propagation during the tensile stretching of solid polymers, J. Mater. Sci., 18, 1731.

G'Sell C., Hiver J. M., Dahoun A. (2002). Experimental characterization of deformation damage in solid polymers under tension, and its interrelation with necking, Inter. J. Solids and Structures, 39, 3857.

G'Sell C., Jonas J. J. (1979). Determination of the plastic behavior of solid polymers at constant true strain rate, J. Mater. Sci., 14, 583.

Hadriche I., Ghorbel E., Masmoudi N., Halouani F. E. (2010). Influence of strain rate on the yielding behavior and on the self heating of thermoplastic polymers loaded under tension, Key Eng. Mater., 446, 63.

Higgs P. G., Gaylord R. J. (1990). Slip-links, hoops and tubes: tests of entanglement models of rubber elasticity, Polymer, 31, 70.

Hill R. (1952). On discontinuous plastic states, with special reference to localized necking in thin sheets, J. Mech. Phys. Solids, 1, 19.

Hiss R., Hobeika S., Lynn C., Strobl G. (1999). Network stretching, slip processes, and fragmentation of crystallites during uniaxial drawing of polyethylene and related copolymers. A comparative study, Macromolecules, 32, 13, 4390.

Hoge K. G., Mukherjee A. K. (1977). The temperature and strain rate dependence of the flow stress of tantalum, J. Mater. Sci., 12, 1666.

Hollomon J. H. (1945). Tensile deformation, Trans. Metall. Soc. American Institute of Mining and Metallurgical Engineers, 162, 268.

Hutchinson J. W., Neale K. W. (1983). Neck propagation, J. Mech. Phys. Solids, 31, 405.

Jang B. Z., Uhlmann D. R., Vander Sande J. B. (1984). Ductile-brittle transition in polymer, Journal of Applied Polymer Science, 29, 3409.

Jar P. -Y. B., Muhammad S. (2012). Cavitation-induced rupture in high-density polyethylene copolymers, Polymer Engineering and Science, 52, 1005.

Khan F., Yeakle C. (2011). Experimental investigation and modeling of non-monotonic creep behavior in polymers, Int. J. Plasticity, 27, 512.

Klepaczko J. (1975). Thermally activated flow and strain rate history effects for some polycrystalline FCC metals, Mater. Sci. Eng., 18, 121.

Klingbeil W. W., Shield R. T. (1966). Large-deformation analysis of bonded elastic mounts, Z.A.M.P. (J. Appl. Math. Phys.), 17, 20, 281.

Kwon H. J., Jar P. –Y. B. (2007a). The application of essential work of fracture concept to toughness characterization of high-density polyethylene, Polym. Eng. Sci., 47, 1327.

Kwon H. J., Jar P. –Y. B. (2008). On the application of FEM to deformation of high-density polyethylene, Int. J. Solids Structures, 45, 3521.

Li H. X., Buckley C. P. (2008). Evolution of strain localization in glassy polymers: A numerical study, Int. J. Solids Structures, 46, 1607.

Li H. X., Buckley C. P. (2010). Necking in glassy polymers: Effects of intrinsic anisotropy and structural evolution kinetics in their viscoplastic flow, Int. J. Plasticity, 26, 1726.

Lim S. H., Yu Z. Z., Mai Y. W. (2010). Effects of loading rate and temperature on tensile yielding and deformation mechanisms of nylon 6-based nanocomposites, Composites Sci. Tech., 70, 1994.

Liu L. -Z., Hxiao B. S., Fu B. X., Ran S., Toki S., Chu B., Tsou A. H., Agarwal P. K. (2003). Structure changes during uniaxial deformation of ethylene-based semicrystalline ethylene-propylene copolymer. 1. SAXS study, Macromolecules, 36, 6, 1920.

Liu Y., Truss R. W. (1994). A study of tensile yielding of isotactic polypropylene, J. Polym. Sci. Part B: Polym. Phys., 32, 12, 2037.

Lu X., Brown N. (1990). Transition from ductile to slow crack growth failure in a copolymer of polyethylene, Journal of materials science, 25, 411.

Masud A. (2005). A 3-D model of cold drawing in engineering thermoplastics, Mech. Adv. Mater. Structures, 12, 457.

Muhammad S., Jar P. -Y. B. (2010). Effect of aspect ratio on large deformation and necking of polyethylene, J. Mater. Sci., 46, 1110.

Muhammad S., Jar P. -Y. B. (2013). Determining stress-strain relationship for necking in polymers based on macro deformation behavior, Finite Elements in Analysis and Design, 70-71, 36.

Muliana A., Rajagopal K. R. (2012). Modeling the response of nonlinear viscoelastic biodegradable polymeric stents, Int. J. Solids and Structures, 49, 989.

Neale K. W., Tugcu P. (1985). Analysis of necking and neck propagation in polymeric materials, J. Mech. Phys. Solids, 33, 323.

Neale K. W., Tugcu P. (1988). Approximate methods for analyzing the cold drawing of polymeric fibres and films, Int. J. Numer. Methods Eng., 25, 99.

O'Connell P. A., Duckett R. A., Ward I. M. (2002). Brittle-ductile transitions in polyethylene, Polymer Engineering and Science, 42, 7, 1493.

Ogden R. W. (1972). Large deformation isotropic elasticity: on the correlation of theory and experimental for compressible rubberlike solids, Proceedings of the Royal Society of London, Series A (Mathematical and Physical Sciences), 328, 567.

Osman M. A., Rupp J. E. P., Suter U. W. (2005). Tensile properties of polyethylene-layered silicate nanocomposite, Polymer, 46, 1653.

Pae K. D., Chu H. -C., Lee J. K., Kim J. -H. (2000). Healing of Stress-Whitening in Polyethylene and Polypropylene at or Below Room Temperature, Polymer Engineering and Science, 40, 8, 1783.

Pawlak A., and Galeski A. (2005). Plastic deformation of crystalline polymers: The role of cavitation and crystal plasticity, Macromolecules, 38, 9688.

Peterlin A. (1971). Molecular model of drawing polyethylene and polypropylene, Journal of Materials Science, 6, 6, 490.

Peterlin A. (1987). Drawing and extrusion of semi-crystalline polymers, Colloid Polym. Sci., 265, 357.

Plummer C. J. G., Goldberg A., Ghanem A. (2001). Micromechanisms of slow crack growth in polyethylene under constant tensile loading, Polymer, 42, 9551.

Raghava R., Caddell R. M. (1973). The macroscopic yield behavior of polymers, J. Mater. Sci., 8, 225.

Roland C. M., Twigg J. N., Vu Y., Mott P. H. (2007). High strain rate mechanical behavior of polyurea, Polymer, 48, 574.

Serban D. A., Marsavina L., Silberschmidt V. V. (2012). Response of semi-crystalline thermoplastic polymers to dynamic loading: A finite element study, Comp. Mat. Sci., 64, 116.

Shariff M. H. B. M. (1993). A general approach to axial deformation of bonded elastic mounts of various cross-sectional shapes, Appl. Math. Modelling, 17, 8, 430.

Silano A. A., Bhateja S. K., Pae K. D. (1974). Effects of hydrostatic pressure on the mechanical behavior of polymers: polyurethane, polyoxymethylene, and branched polyethylene, Int. J. Polym. Mater., 3, 117.

Spitzig W. A., Richmond O. (1979). Effect of hydrostatic pressure on the deformation behavior of polyethylene and polycarbonate in tension and in compression, Polym. Eng. Sci., 19, 1129.

Spitzig W. A., Sober R. J., Richmond O. (1975). Pressure dependence of yielding and associated volume expansion in tempered martensite, ACTA Metallurgica, 23, 885.

Tabiei A., Yi W., Goldberg R. (2005). Non-linear strain rate dependent micro-mechanical composite material model for finite element impact and crashworthiness simulation, Int. J. Non-Linear Mech., 40, 957.

Tomita Y., Hayashi K. (1993). Thermo-elasto-viscoplastic deformation of polymeric bars under tension, Int. J. Solids Structures, 30, 225.

Tomita Y., Takahashi T., Shindo A. (1990). Neck and bulge propagation in polymeric cylinders under internal pressure, Int. J. Mech. Sci., 32, 4, 335.

Tugcu P., Neale K. W. (1987a). Analysis of plane-strain neck propagation viscoplastic polymeric films, Int. J. Mech. Sci., 29, 793.

Tugcu P., Neale K. W. (1987b). Necking and neck propagation in polymeric materials under plane-strain tension, Int. J. Solids Structures, 23, 1063.

Tugcu P., Neale K. W. (1988). Analysis of neck propagation in polymeric fibres including the effects of viscoplasticity, Trans. ASME, J. Engng. Mater. Tech., 110, 4, 395.

Van Krevelen D. W. (1997). Properties of Polymers, third ed., Elsevier, Amsterdam.

Viana J. C. (2005). Structural interpretation of the strain-rate, temperature and morphology dependence of the yield stress of injection molded semicrystalline polymers, Polymer, 46, 11773.

Vincent P. I. (1960). The necking and cold-drawing of rigid plastics, Polymer, 1, 7.

Volynskii A. L., Shmatok Ye. A., Ukolova Ye. M., Arzhakova O. V., Yarsheva L. M., Lukovkin G. M., Bakeyev N. F. (1991). Two types of crazing realized in the course of strain of polymers, Polymer science USSR, 33, 5, 917.

Ward A. L., Lu X., Huang Y., Brown N. (1991). Mechanism of slow crack growth in polyethylene by an environmental stress cracking agent, Polymer, 32, 12, 2172.

Ward I. M., Hadley D. W. (2000). Mechanical properties of solid polymers, Wiley, Chichester, UK.

Wesseloo J., Visser A. T., Rust E. (2004). A mathematical model for the strain-rate dependent stress-strain response of HDPE geomembranes, Geotextiles Geomembr., 22, 273.

Wu J. J., Buckley C. P. (2004). Plastic deformation of glassy polystyrene: A unified model of yield and the role of chain length, J. Polym. Sci.B, 42, 11, 2027.

Wu P. D., van der Giessen E. (1992). On improved 3-D non-Gaussian network models for rubber elasticity, Mech. Res. Commun., 19, 5, 427.

Wu P. D., van der Giessen E. (1993). On improved network models for rubber elasticity and their applications to orientation hardening in glassy polymers, J. Mech. Phys. Solids, 41, 3, 427.

Wu P. D., van der Giessen E. (1995). On neck propagation in amorphous glassy polymers under plane strain tension, Int. J. Plast., 11, 211.

Zaïri F., Naït-Abdelaziz M., Woznica K., Gloaguen J. –M. (2005). Constitutive equations for the viscoplastic-damage behaviour of a rubber-modified polymer, Eur. J. Mech. A/Solids, 24, 1, 169.

Zebarjad, S. M., Sajjadi, S. A. (2008). On the strain rate sensitivity of HDPE/$CaCO_3$ nanocomposites, Mater. Sci. Eng. A, 475, 365.

Zhang X. C., Butler M. F., Cameron R. E. (2000). The ductile-brittle transition of irradiated isotactic polypropylene studied using simultaneous small angle x-ray scattering and tensile deformation, Polymer, 41, 3797.